Interlayer Charge Transport in Quasi-Two-Dimensional Organic Conductors

Kaori Sugii

February 2014

Interlayer Charge Transport in Quasi-Two-Dimensional Organic Conductors

Kaori Sugii
Doctoral Program in Materials Science and Engineering

Submitted to the Graduate School of
Pure and Applied Sciences
in Partial Fulfillment of the Requirements
for the Degree of Doctor of Philosophy in
Engineering

at the
University of Tsukuba

Contents

Abstract

Organic conductors have attracted great interest because of the variety of possible electronic states, such as Mott insulating, superconducting, metallic, and charge ordering states. The electronic states in most organic conductors are highly two-dimensional (2D) because such conductors are layered structures composed of organic molecules and anions. In these layered organic conductors, spin, charge, and orbital degrees of freedom lead to intriguing physical properties at low temperatures. For such properties, strong electron correlations in these 2D electronic structures play an essential role. Hence, along with transition metal oxides and rare-earth metal complexes, organic conductors are being recognized as important targets for studying strong correlation effects in the electronic states.

In layered 2D organic conductors, the interlayer charge transport properties are well-known to show characteristic features in temperature and magnetic field dependent phenomena. Such phenomena are strongly affected by scattering caused by (1) local magnetic moments in the anion layers and (2) impurities (or defects) in the conducting layers. Despite the extensive experiments performed so far, detailed mechanisms of the characteristic phenomena in the interlayer charge transport remain unsolved problems. As high-quality single crystals can be produced, 2D organic conductors are good candidates to study the interlayer charge transport. For this thesis, two material systems with layered structures were chosen and systematic measurements of their electric and magnetic properties were obtained. We give a brief overview of the results found for these materials.

(1) Conductivity and magnetism in π-d organic conductors κ-(BDH-TTP)$_2$FeX$_4$ (X = Br, Cl)

In π-d organic conductors, the π conduction electrons within the organic molecular layers, where transport behavior is strongly affected by electron correlations, are expected to interact with the localized d electrons in the anion layers. To investigate the correlation between the conductivity and magnetism, the magnetic and magnetotransport properties of the π-d systems κ-(BDH-TTP)$_2$FeBr$_4$ (FeBr$_4$ salt) and κ-(BDH-TTP)$_2$FeCl$_4$ (FeCl$_4$ salt) have been investigated. The π electrons in the BDH-TTP sheets exhibit simple metallic behavior down to 30 mK for both salts. The magnetic susceptibility of the FeBr$_4$ salt, which is mainly associated with the Fe^{3+} d spins ($S = 5/2$), obeys the Curie-Weiss law, indicating the presence of an antiferromagnetic (AF) transition at $T_N = 3.9$ K. In the AF state, a steep S-shaped increase in the magnetization at 1.5 T (H_{SF}) in the field parallel to the a-axis is found, which is ascribed to a spin-flop transition. Additionally, the magnetization curves for fields perpendicular to the easy axis show an inflection point at $H_c = 3.1$ T, suggesting a spin canting configuration in the bc-plane. A possible AF spin structure based on the magnetization data

and molecular orbital calculations features a triangular lattice consisting of the Fe d electron spins and the donor π electron spins. A steep decrease in the magnetoresistance (MR) for the AF state is observed at $H_{\rm SF}$ for $H \parallel a$, proving that the strong π-d interaction affects the electron transport in the donor system. An anomalous broadening of the electron spin resonance (ESR) linewidth in the critical region above $T_{\rm N}$ is suggestive of a developing magnetic short-range order, for which the low-dimensionality in the spin system is responsible.

For the $FeCl_4$ salt, a rapid change in the magnetic torque at low magnetic fields is associated with a change in sign at low temperatures below 0.4 K. The systematic measurements reveal that the $3d$ spins have an AF order at about 0.4 K and that the torque sign change is caused by a metamagnetic transition. A rapid decrease in the MR at the metamagnetic transition field provides clear evidence of a finite π-d interaction. Characteristic temperature dependences of the magnetic susceptibility and the ESR g-value are found in the paramagnetic phase, which are explained in terms of a single-ion anisotropy effect. These physical properties of the $FeCl_4$ salt indicate that both the π-d and d-d interactions in this salt are much weaker than those in the $FeBr_4$ salt.

(2) Incoherent interlayer charge transport in α-(BEDT-TTF)$_2$NH$_4$Hg(SCN)$_4$

To investigate the incoherent interlayer transport in a 2D organic superconductor α-(BEDT-TTF)$_2$NH$_4$Hg(SCN)$_4$, we have performed the interlayer MR measurements for many samples with different qualities. The temperature dependence of the interlayer resistivity is found to be strongly sample-dependent. For some samples, the Shubnikov-de Hass oscillations are measured to determine the Dingle temperature ($T_{\rm D}$), characterizing the sample quality. When $T_{\rm D}$ is relatively low, the incoherent interlayer transport becomes evident only in high magnetic fields parallel to the layers. This incoherent behavior is due to the confinement effect of the electrons by the parallel field. When $T_{\rm D}$ is sufficiently high, the interlayer transport is incoherent in the whole angle and field region. From the systematic measurements, we obtained the crossover field from the coherent to incoherent interlayer transport as a function of $T_{\rm D}$. The crossover field is constant in the low $T_{\rm D}$ region below 1.2 K but decreases with $T_{\rm D}$ above it. This behavior is explained in terms of two conducting channels, the band coherent and impurity-assisted incoherent channels.

This thesis is composed of four main sections; the introduction, experimental methods, κ-(BDH-TTP)$_2$FeX$_4$ (X = Br, Cl), and α-(BEDT-TTF)$_2$NH$_4$Hg(SCN)$_4$. In the introduction, a detailed background is presented and purposes of the study are explained. Next, experimental methods are explained and followed by a discussion on the magnetotransport properties and other magnetic properties arising from the π-d interaction for the $FeBr_4$ and $FeCl_4$ salts. The incoherence in the interlayer charge transport is then discussed for α-(BEDT-TTF)$_2$NH$_4$Hg(SCN)$_4$.

Chapter 1

Introduction

1.1 Background

Because of their novel electronic and chemical properties and their application for electronic devices, organic materials have been extensively developed and studied in both industry and academia for decades. Until the 1950s, organic compounds made of non metallic atoms had been thought to be insulators because they had closed orbits. However, when an electron is removed from or added to an organic polymer, the holes or electrons can move freely, and the polymer becomes conductive. In 1954, a perylene-bromine charge complex was the first semiconducting organic material to be discovered.[1] The first metallic polymer was synthesized by A. J. Heeger, A. G. MacDiarmid, and H. Shirakawa in 1975, for which they won the 2000 Nobel Prize in Chemistry.[2] Synthetic metals are classified into two groups: organic conducting polymers and organic conductors (molecular conductors). A Polymer is a large molecule composed of many small elements connected by strong covalent bonds. A molecular conductor is composed of small molecules that interact with each other through weak inter-molecular interactions, and form a single crystal. Charges are transferred from donor molecules to acceptor molecules, and the surplus holes can become conductive. Along with the success in the development of organic conducting polymers, the organic molecular conductor, TTF-TCNQ was found in 1973 to exhibit metallic conduction.[3] Diagrams of the TTF, TCNQ molecules, and other organic molecules are shown in Fig. 1.1.[4] The conductive organic material exhibits conductance of up to $\sigma = 10^4$ Scm^{-1}.

A number of other organic conductors and organic superconductors have since been synthesized. The first organic superconductor, $(TMTSF)_2PF_6$, was discovered in 1980 and has a quasi-1-dimensional (q1D) Fermi surface.[5] This material undergoes a superconducting transition at 0.9 K under a hydrostatic pressure of 12 kbar. Following this discovery, electronic states of two-dimensional (2D) organic BEDT-TTF salts were found to be superconducting under ambient pressure.[6,7] The 2D κ and β' type salts, in which strong electron correlations are introduced, show superconducting transitions above 10 K. Moreover, three-dimensional (3D) superconductors, such as K doped C_{60}, were developed ($T_c \approx 33$ K). These studies on organic superconductors have been expanded in efforts to achieve higher T_c values.

Recently, studies pursuing novel functionality in organic conductors, such as single-component molecular crystals and molecular magnets, have also attracted attention.[8]

1.1.1 Molecular conductor

Most molecular conductors are composed of donor and acceptor molecules. For example, in a (BEDT-TTF)$_2$X salt, two BEDT-TTF molecules supply one electron to the X anion (acceptor) molecule, giving rise to one hole for every two BEDT-TTF molecules. By charge transfer between the molecules, cation and anion radicals are generated in forming the salt. For this reason, molecular conductors are also called charge transfer salts.

One important feature of organic conductors is the low dimensionality, arising from the large anisotropy of the molecular structures. Illustrations of two crystal structures are shown in Fig. 1.2. These examples show that the large p orbits from either the carbon or sulfur atoms of the donor molecules overlap, allowing the π conjugated system to form. Because of charge transfer, the anion molecules become insulating, and hence form insulating layers situated between conducting layers. The TMTTF molecules from adjacent layers stack along the direction normal to the layer, thus, enabling electron conduction to become 1D. In contrast, the BEDT-TTF molecules stack two dimensionally within the donor layer as shown in Fig. 1.2. In the interlayer direction, the donor molecules are separated from each other by the insulating anion layers. This particular stacking of the BEDT-TTF salts enables 2D conduction within the layer, which means that the transfer integral is smaller for the interlayer direction than that for the in-plane direction.

Many different molecular configurations have been found in the donors of the 2D systems as shown in Fig. 1.3(a). In the β' and κ type salts, the facing pair of donor molecules has a strong interaction and can be dimerized. The electron correlation between each dimer plays an essential role in these salts. One of the features of organic conductors is the simple Fermi surfaces in spite of their complicated molecular arrangements. The band structures and the Fermi surfaces of some organic conductors are shown in Figs. 1.3(b)-(d). Most salts have a 2D or 1D Fermi surface.

The band calculations for these salts are usually done by the tight-binding extended Hückel method, which is a semiempirical approach. This method provides useful qualitative information of the Fermi surfaces of organic conductors. However, there are some serious problems with parameters such as the bandwidths and effective band masses. In recent years, the band calculations by the first-principles method have been performed to investigate the detailed electronic structures for some molecular metals. Figure 1.4(a) shows the band structure and the Fermi surface of α-(BEDT-TTF)$_2$KHg(SCN)$_4$ calculated using the extended Hückel method.[14] The general structure of the energy band and the shape of the Fermi surface agree very well with that found in the first-principles study shown in Fig. 1.4(b).[15] The absolute value of the band width, however, is larger for the extended Hückel method than that for the first-principles study, in this case.

We can control the molecular arrangement by changing either the species of anions or the crystallization process. As a result, a variety of physical and electronic properties such as superconducting transitions, density waves, charge order, and Mott insulating phases have been observed. Because of this variety, organic conductors have attracted much attention in the fields of chemistry, and physics,

both experimentally and theoretically.

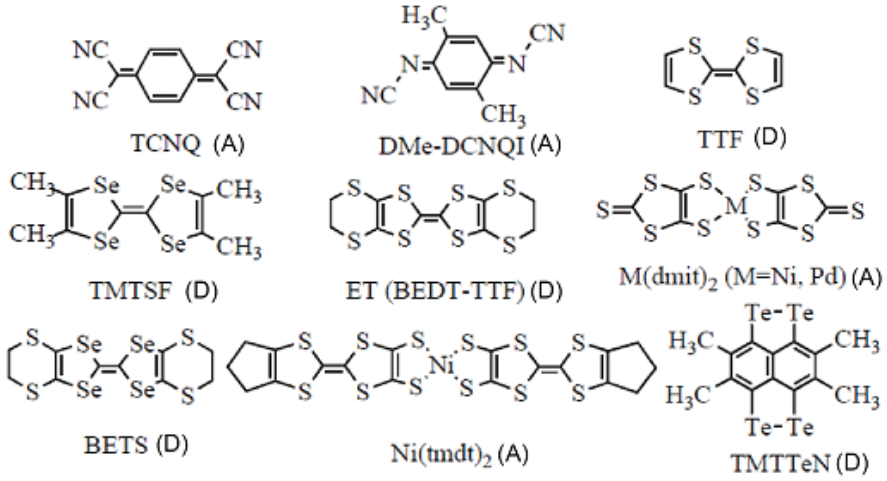

Figure 1.1: Examples of organic molecules. (D) and (A) denote the donor and accepter molecules, respectively.[4]

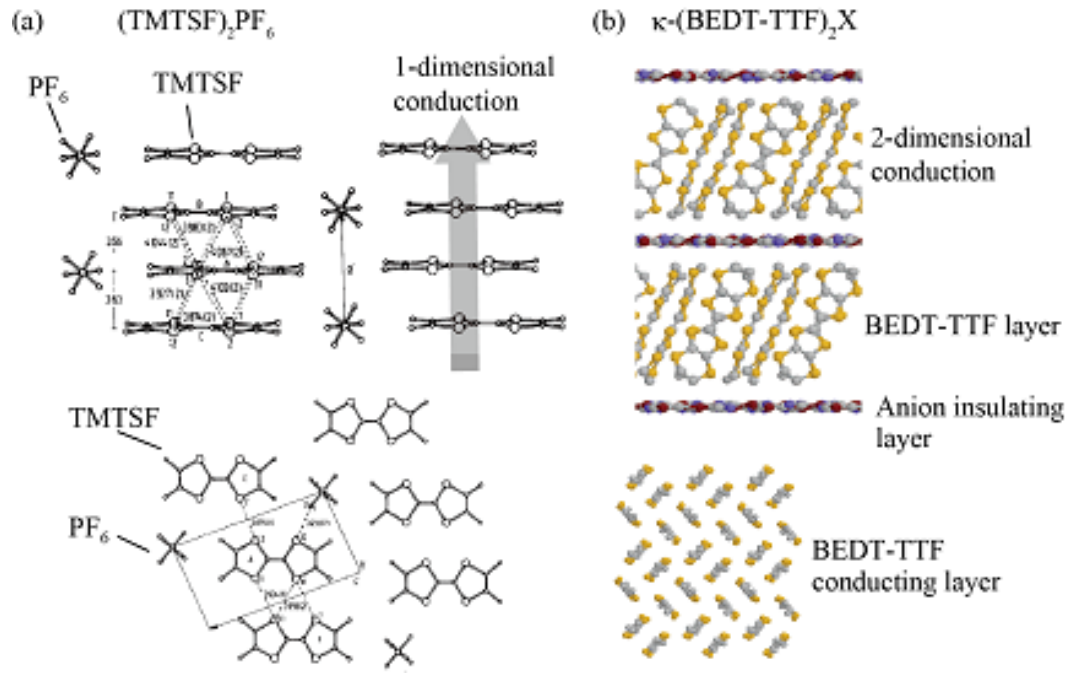

Figure 1.2: (a) Crystal structure and conducting direction of 1D material. (b) Crystal structures of 2D systems. The 2D conducting layers are separated by the insulating anion layers.[9,10]

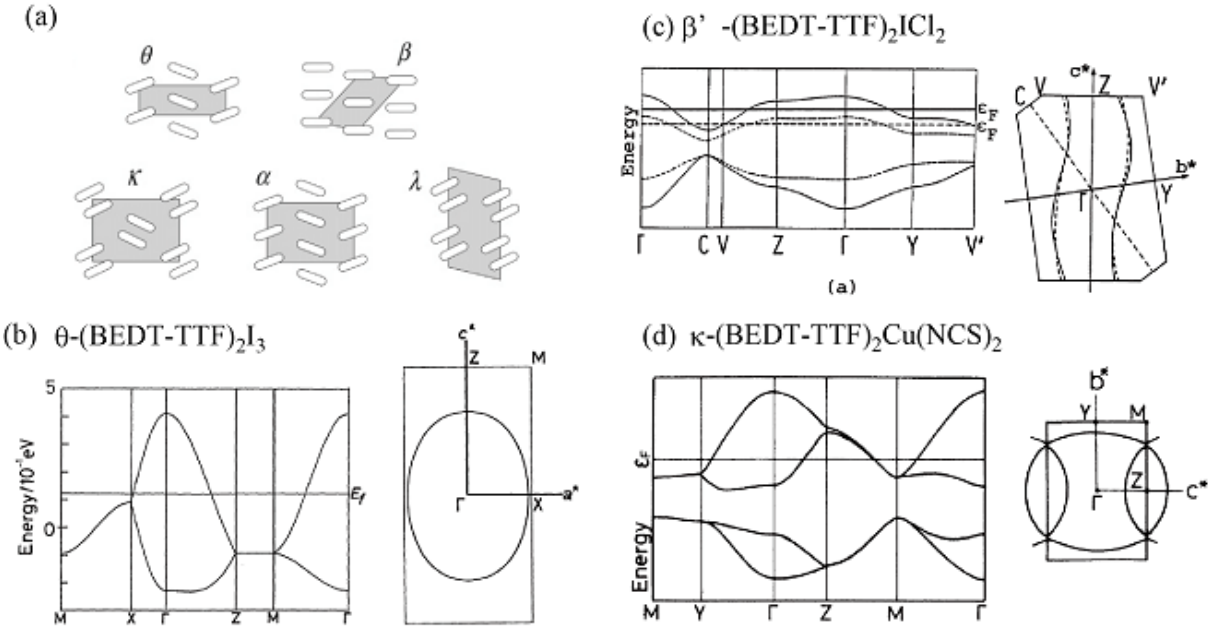

Figure 1.3: (a) Relation between the donor arrangement and the unit cell for a range of organic conductors. (b)-(d) Fermi surfaces for the donor layer for the θ, β', and κ type organic conductors.[11–13]

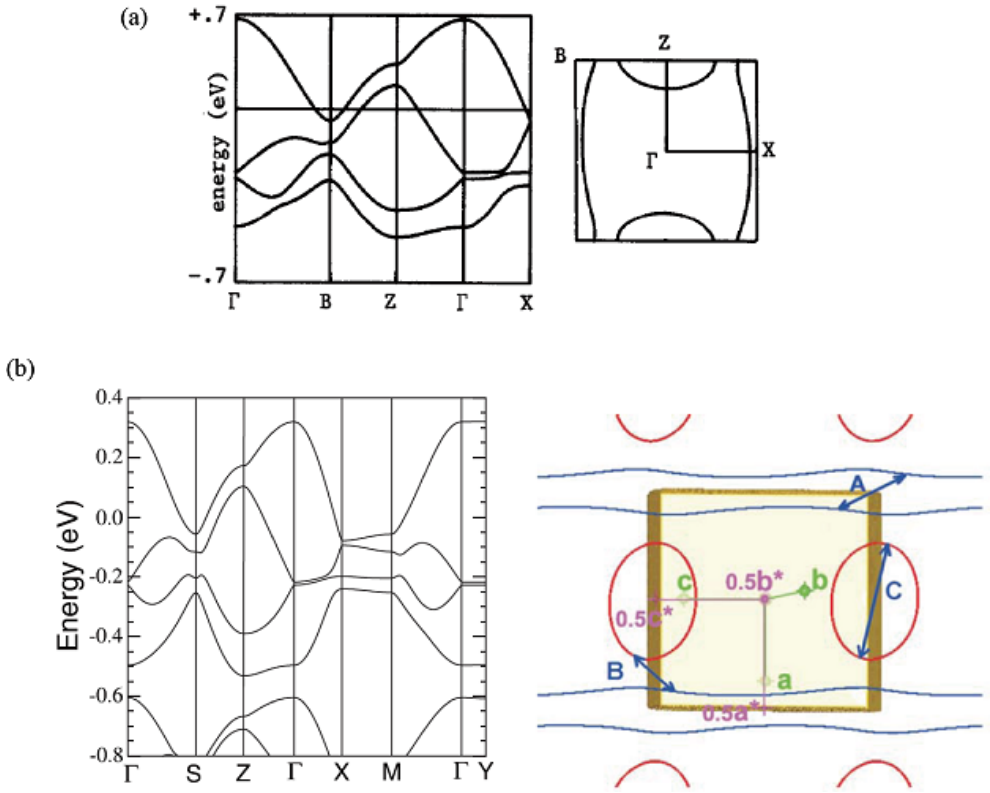

Figure 1.4: Band structure and Fermi surface of α-(BEDT-TTF)$_2$KHg(SCN)$_4$ at 104 K using (a) the extended Hückel method and (b) the first-principles density functional theory.[14,15]

1.1.2 π-d organic conductor

π and s electrons (holes) are able to move freely as conduction carriers within the salts. If dopants having d orbits, such as transition metals like Fe, are located in the sea of the conduction s electrons, the Heisenberg-type exchange interactions between the s and d spins are given by

$$-2J_{sd}\delta(r)\boldsymbol{S}\cdot\boldsymbol{s}, \tag{1.1}$$

where $\boldsymbol{S}$ and $\boldsymbol{s}$ denote the spins of the s and d electrons, and J_{sd} is exchange interaction parameter. Effective field, acting on a s electron decreases with distance from a d electron; this decay is described by the δ function for the distance. This s-d interaction causes spin polarizations of the conducting s spins near the localized d spins, enabling long-ranged exchange coupling of the d spins via the s spins. The coupling mechanism is referred to as the RKKY (Ruderman-Kittel-Kasuya-Yoshida) interaction, which is important in magnetic diluted alloys.

In the 1990s, studies of organic conductors containing magnetic $3d$ spins (π-d systems) began to reveal novel magnetic and transport properties. In π-d systems, the π conduction electrons, the transport behavior of which are affected by strong electron correlations, were expected to interact with the localized d spins. Accordingly, this situation enabled magnetic conductors to be designed that exhibited phenomena, highlighting the importance of the interplay between the electron transport and magnetism, which cannot be observed in traditional magnetic conductors.[16–21] In π-d systems such as λ-$(BETS)_2FeCl_4$ and $TTP[Fe(Pc)(CN)_2]_2$ (Pc: Phthalocyanine), interesting phenomena have been observed, where the cooperation between the strong π-d interaction (exchange interaction between the conducting π spins and localized $3d$ spins) and strong electron correlations among the π electrons play an essential role.[22,23] The structures of these π-d systems are shown in Figs. 1.5 and 1.6. The anion layers containing Fe(III) ions with large $3d$ moments and the donor layers are arranged alternately in λ-$(BETS)_2FeCl_4$. For this sandwiched structure, the magnitude of the π-d interaction depends on the distance between the anion and donor molecules. In contrast, the $Fe(Pc)(CN)_2$ molecule contains both π conduction electrons on the Pc ligand and a $3d$ moment on the Fe^{3+} ion. Thus, the π-d interaction in $TPP[Fe(Pc)(CN)_2]_2$ is larger than that in the salts with the sandwiched structure. λ-$(BETS)_2FeCl_4$ undergoes a magnetic-field-induced superconducting phase, whereas the normal superconducting phase is easily destroyed by the magnetic field. The anomalous temperature dependence of the specific heat in this salt is also regarded as a result of the π-d interaction.[25] $TTP[Fe(Pc)(CN)_2]_2$ exhibits a large negative magnetoresistance (MR) as seen in Fig. 1.6(b). Recently, an organic ion-radical salts without metal ions have also been found in which conductivity and magnetism coexist.[26]

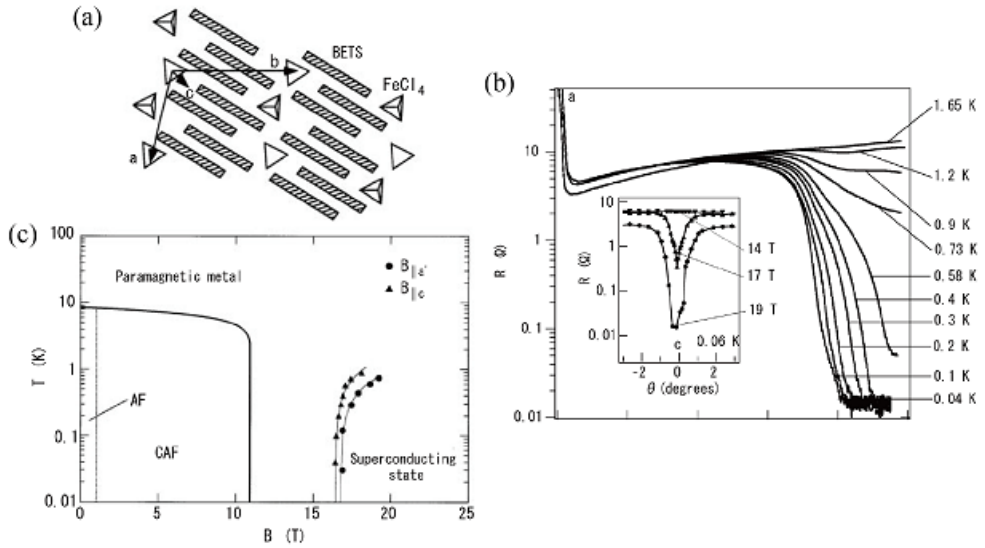

Figure 1.5: (a) Schematic of the crystal structure of λ-$(BETS)_2FeCl_4$. (b) Interlayer resistance when the field is exactly parallel to the conduction plane. (c) Temperature vs. magnetic field diagram.[22]

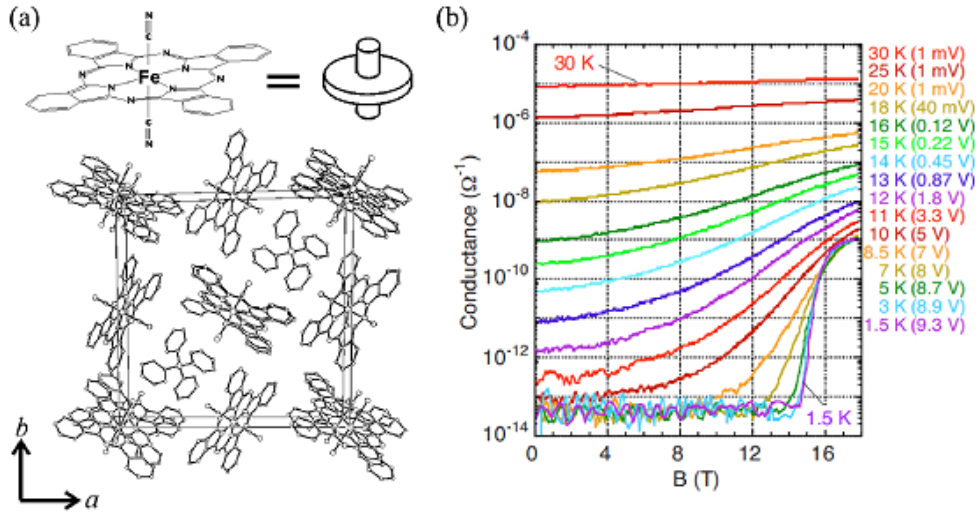

Figure 1.6: (a) Structure of $TTP[Fe(Pc)(CN)_2]_2$. (b) Interlayer conductance vs. magnetic field.[23,24]

1.2 Incoherent interlayer transport

1.2.1 Incoherent interlayer transport in q1D systems

The incoherent behavior of the interlayer charge transport in the highly anisotropic conductors has been one of the long-standing issues in solid state physics.[27,28]

The incoherence of the interlayer charge transport was first discussed in a q1D organic conductor $(TMTSF)_2PF_6$.[29,30] $(TMTSF)_2PF_6$ has a pair of corrugated 1D Fermi surfaces [see Fig. 1.7(a)], which are perpendicular to the a-axis (the most conducting direction). When a high magnetic field is applied along the second conducting direction (b-axis), the electrons are driven in the k_c direction on the Fermi surface by the Lorentz force. In real space, the electrons run at constant velocity in the a-axis but move sinusoidally in the least conducting direction (c-axis). The width of the electron motion in real space is given by

$$\Delta z = \frac{4t_z}{ev_F H_b}, \tag{1.2}$$

where t_z is the transfer integral along the c-axis, v_F is the Fermi velocity, and H_b is the magnetic field component along the b-axis. As the field increases, the amplitude of the sinusoidal motion Δz diminishes and becomes smaller than the distance between layers. The electrons are then confined in each layer; the electronic states are decoupled between adjacent layers. Hence, the interlayer transport is prohibited without scattering and thus becomes incoherent in high magnetic fields.[31] In this situation, the angular dependence of the MR cannot be explained by the Boltzmann transport theory. The interlayer MR for $(TMTSF)_2PF_6$ is shown in Fig. 1.8(a).[29] Apart for the dips caused by the Lebed resonance, the MR background shape changes above 1 T. The interlayer MR has a maximum (minimum) in a field perpendicular (parallel) to the layer, whereas the Boltzmann transport theory predicts the opposite behavior. This unconventional MR behavior, the reversal of the angular dependence in the MR, is considered as indicating *incoherent* interlayer transport, and has been extensively studied both theoretically and experimentally.[29,31–33]

1.2.2 Incoherent interlayer transport in 2D systems

In recent decades, another criterion for incoherent transport has been discussed for 2D systems.[27,28,34]

In metallic materials, the electron conduction is ascribed to the coherent motion of electrons in the band states. A model commonly used for 2D materials consists in the free motion of electrons within the 2D planes and nearest-neighbor hopping between the planes. The energy is given by

$$\epsilon_k = \frac{\hbar \boldsymbol{k}_{\parallel}^2}{2m_c} - 2t_z \cos(k_z c), \tag{1.3}$$

where $\boldsymbol{k}_{\parallel}$ and k_z are the in-plane and z-axis components of the momentum, respectively. m_c is the in-plane effective mass and c is the length between the adjacent layers. Because t_z is finite, the cylindrical Fermi surface is corrugated as shown in Fig. 1.9. For typical 2D organic conductors, a

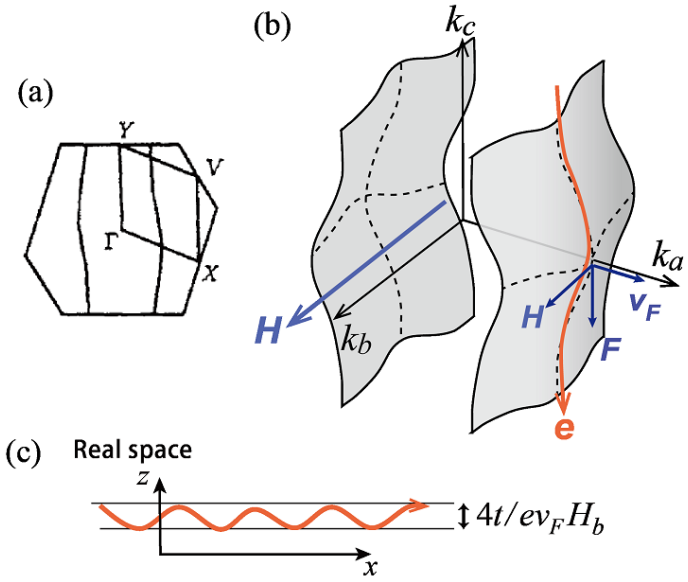

Figure 1.7: (a) Fermi surface of $(TMTSF)_2PF_6$.[10] (b) Schematic diagrams of the q1D Fermi surface and the electron motion with a magnetic field applied along the second conducting direction ($\| k_b$). (c) Confinement of the electron motion in real space.

highly 2D electronic state is formed at t_z of approximately 1 K, and a Fermi energy of order 1000 K. With this model, the electron motion can be well described by the Boltzmann transport theory.

The coherence of the interlayer charge transport can be determined by the relation between two factors; the interlayer transfer integral t_z and the scattering time τ. For $t_z \gg \hbar/\tau$, a cylindrical 2D Fermi surface with corrugation given by t_z is well defined. The electrons can easily move in the interlayer direction without scattering, the interlayer transport is then being *coherent*. The angular dependence of the MR is well described by the Boltzmann transport theory. The evidence for the coherent transport is the observation of a narrow peak, called the *coherence peak*, in the MR under high fields parallel to the layers. This peak arises from small cyclotron orbits [shown in Fig. 1.10(b)] on the side of the corrugated cylindrical 2D Fermi surface.[35] Additionally, the MR has characteristic oscillatory behavior dependent on the field angle, which is called angular-dependent magnetoresistance oscillation (AMRO). The AMRO arises from the periodic cyclotron motion across the corrugated Fermi surface. The interlayer conductivity for a corrugated 2D Fermi surface with axial symmetry is given by

$$\begin{aligned} \sigma_{zz}(H) &= \sigma_{zz}^0 \Big\{ J_0^2(ck_F \tan\theta) + \sum_{\nu=1}^{\infty} \frac{2J_\nu^2(ck_F \tan\theta)}{1+(\nu\omega_c\tau\cos\theta)^2} \Big\}. \\ \sigma_{zz}^0 &= \frac{2e^2 m_c t_z^2 c\tau}{\pi\hbar^4} = \left(\frac{\tilde{v}_z}{v_F}\right)^2 \frac{Ne^2\tau}{m_c}. \end{aligned} \tag{1.4}$$

Here c is the interlayer spacing, k_F is the Fermi wave number, e is the elementary charge, $\tilde{v}_z = 2t_z c/\hbar$, and N is the density of electrons.[36,37] The nth Bessel function J_n has zeros, giving resistance peaks when the field angle satisfies the relation

$$ck_F \tan\theta = \pi\,(n - 1/4) \quad (n = 1, 2, 3\cdots). \tag{1.5}$$

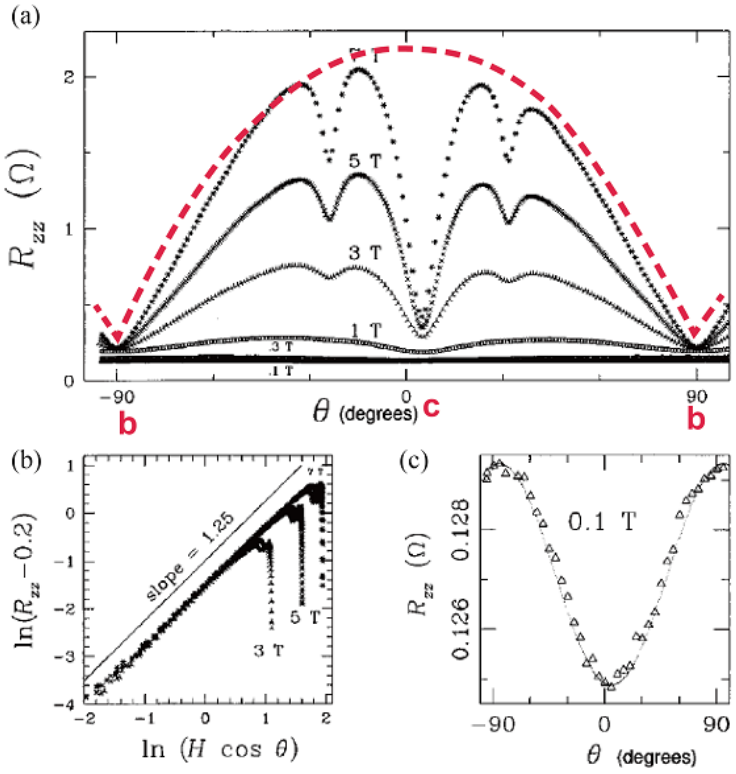

Figure 1.8: (a) MR perpendicular to the *ab*-plane for $(TMTSF)_2PF_6$. The field angle θ is rotated from the *c*- to the *b*-axis. The red curve is added to guide the eyes. (b) Data for magnetic fields of 3, 5, and 7 T, plotted as the natural logarithm of the deviation from a reference value versus the natural logarithm of the magnetic field strength, perpendicular to the *ab* plane. (c) MR at 0.1 T for the *cb*-rotation.[29]

In the opposite limit ($t_z \ll \hbar/\tau$), electrons cannot tunnel between the layers without scattering. The interlayer transport then becomes *incoherent*; the in-plane momentum and energy of the electrons are no longer conserved. A reversal of the angular dependence of the MR, similar to the 1D case, is also observed. In this limit, a corrugated 2D Fermi surface is not defined and it might be a good picture that each layer has an independent 2D Fermi surface.[28,34]

In the intermediate condition, $t_z \approx \hbar/\tau$, the interlayer transport is rather complicated. The interlayer transport between the adjacent layers is dominated by a quantum tunneling (not by a diffusive process). However, successive tunneling rarely occurs because the scattering probability is relatively large. For this case, the angular dependent MR was first calculated by McKenzie and Moses and it is clarified that the MR formula is also given by Eq. (1.4).[27] However, the absence of successive interlayer tunneling means there is no coherence peak in parallel fields. This transport process was originally called *weakly incoherent*. However, in this thesis, we refer to it as *weakly coherent* because the transport between adjacent layers is dominated by the tunneling (a coherent process).

In this condition, the crossover from the coherent to incoherent transport regimes takes place as the magnitude of τ or t_z decreases. The t_z value was tuned for the first time in an artificial GaAs/AlGaAs superlattice by changing the AlGaAs barrier thickness between the GaAs 2D electronic

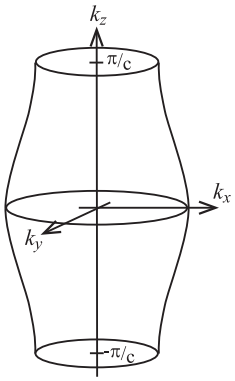

Figure 1.9: Corrugated 2D Fermi surface.

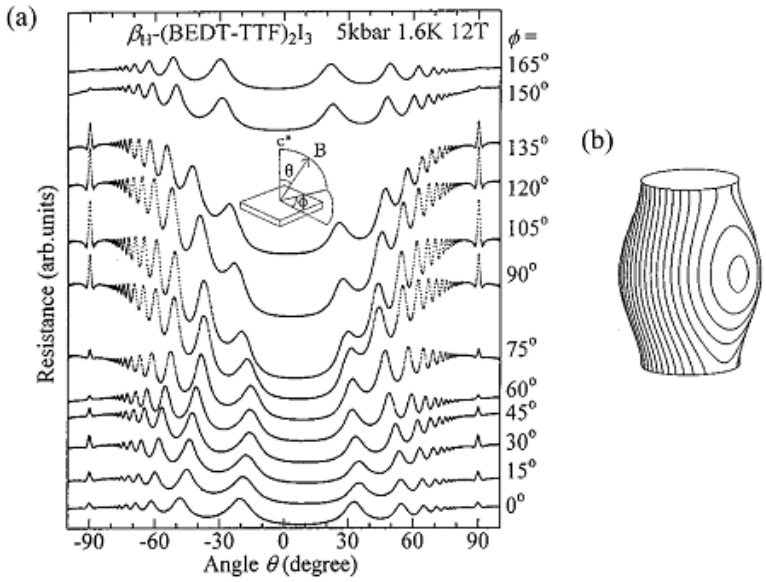

Figure 1.10: (a) Angular dependence of the MR for β_H-(BEDT-TTF)$_2$I$_3$. In addition to the AMRO peaks, a sharp peak structure in the MR appears for magnetic fields nearly parallel to the conduction layer ($\theta = \pm 90°$).[35] (b) An example of the electron orbits on the q2D Fermi surface under a magnetic field parallel to the layer.[35]

states by Kuraguchi *et al.*[38] For the superlattice with large (small) t_z, the conventional (reversal) angular dependence in the MR is observed as seen in Fig. 1.11. For both samples, the AMROs are superimposed on the MR. In some highly 2D organic conductors, the criteria for the coherent transport have been investigated.[28,34,39,40]

The sample quality (τ) dependence of the interlayer transport was first investigated in a 2D system, α-(BEDT-TTF)$_2$KHg(SCN)$_4$ by Kartsovnik *et al.*[41] They found that the angular dependence of the MR behavior was different between two samples with different qualities. (Fig. 1.12). The reversal of the MR background, scaled by the field component perpendicular to the layer, was observed for a dirty sample, whereas a clean sample shows the normal MR background with a coherence peak in fields parallel to the layer. This study shows that the interlayer MR in the incoherent regime is very similar to the decoupled case of the 1D systems by the confinement effect: both the scattering and the confinement effect by the parallel field play crucial roles in the incoherent behavior of the interlayer

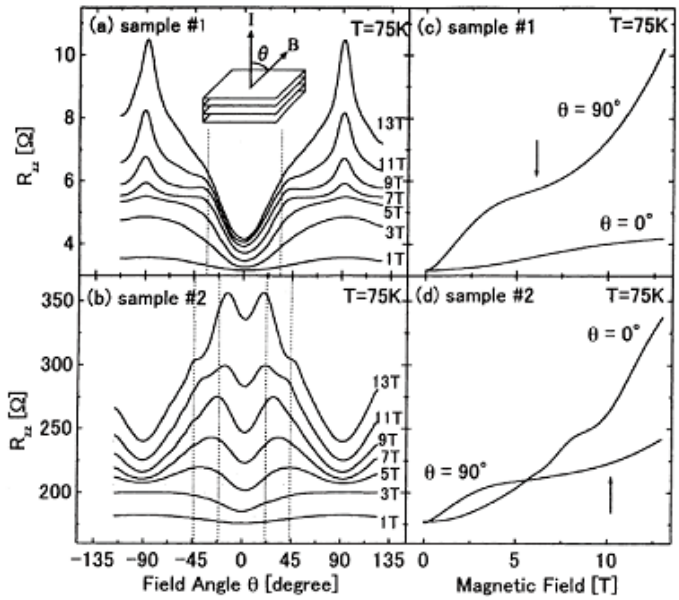

Figure 1.11: Angular dependence of the interlayer MR for (a) sample ♯1 ($\hbar/\tau = 0.98$ meV) and (b) sample ♯2 ($\hbar/\tau = 1.03$ meV) of the GaAs/AlGaAs superlattices. The field dependence for (c) sample ♯1 and (d) sample ♯2. Sample ♯1 exhibits a coherence peak near 90°.[38]

transport in 2D systems.

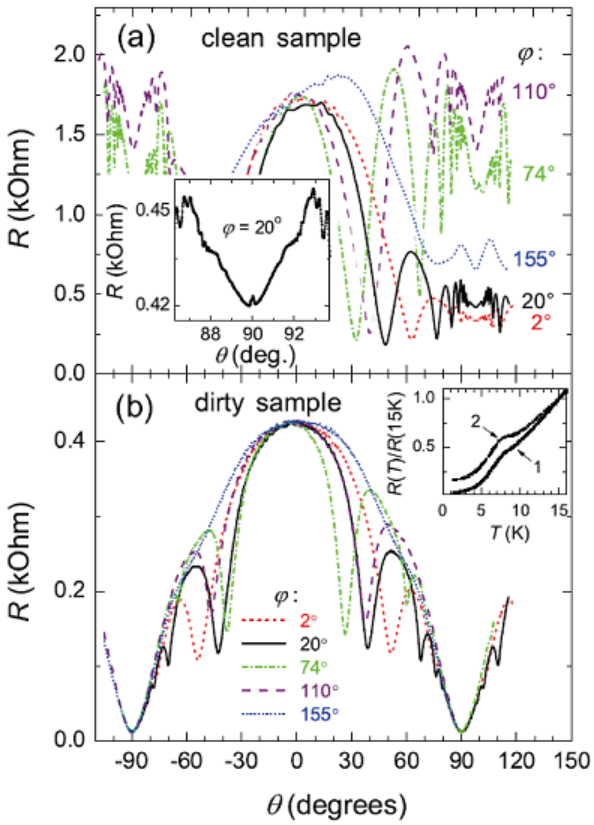

Figure 1.12: Interlayer resistance of two α-(BEDT-TTF)$_2$KHg(SCN)$_4$ salts as a function of the polar angle θ recorded at different azimuthal angles ϕ, $P = 0$ kbar, H= 10 T.[41] A coherence peak is evident for the clean sample (see inset in the upper panel).

1.2.3 Confinement effect in 2D systems

The confinement scenario with the large parallel field in the 1D systems was applied to an anisotropic 2D system,[40] whose cylindrical Fermi surface has an elliptic cross-section.

Over most parts of the orbit, the electrons have an in-plane velocity component $v_\perp$ perpendicular to the magnetic field. On the anisotropic Fermi surface (see Fig. 1.14), when the field is applied parallel to the $\overrightarrow{OP_1}$ (along the shortest Fermi wave vector), electrons close to P_1 experience a very weak Lorentz force because they have small $v_\perp$. The transport of these electrons remains coherent at high fields. In contrast, electrons close to P_2 experience a strong Lorentz force, and are likely to be incoherent. When the field is nearly parallel to $\overrightarrow{OP_2}$, the electrons over most parts of the Fermi surface have large $v_\perp$. Hence, the interlayer transport is likely to be incoherent, and the layers are decoupled. However, when the magnetic field is applied nearly parallel to $\overrightarrow{OP_1}$, a small portion of the electrons on the Fermi surface has a large $v_\perp$. Hence, the electrons remain coherent and a coherence peak can be observed.

The Fermi surface of (BEDT-TTF)$_2$Br(DIA), obtained by AMRO measurements, is presented in Fig. 1.13(b).[40] Actually, a dip in the MR (corresponding to a MR reversal) is enhanced in high field along the long axis but a coherence peak is found in high field along the short axis as shown in Fig. 1.13(c). The results also show that a crossover from the coherent to incoherent behavior takes place as the parallel field along the long axis increases.

The behavior of the interlayer MR in the coherent and incoherent limits is summarized in Fig. 1.15(c). For the coherent interlayer transport, the AMRO peaks and the normal MR background are observed. In the limit of the incoherence, a reversed shape is seen in the MR, which is scaled by the field component perpendicular to the layer, even at low magnetic fields. The studies mentioned above show that the incoherent interlayer transport is strongly affected by the relation between t_z and τ, as well as by the confinement effect caused by the parallel field. However, no systematic investigations have been performed, and it remains unclear how the crossover from the coherent to incoherent transport is induced (see Fig. 1.15). Thus, it was necessary to investigate the MR when only the t_z or τ is modulated and to clarify the effect of the parallel field on the incoherent transport. In this study, we chose to vary the quality (τ) of samples of an organic superconductor α-(BEDT-TTF)$_2$NH$_4$Hg(SCN)$_4$, which was expected to have small t_z becaused of the large anion molecules. The quality of each sample is quantitatively checked by the quantum oscillation measurements. The angular dependence of the MR and the temperature dependence of the resistance for various single crystals can provide much information on the coherence of the interlayer charge transport.

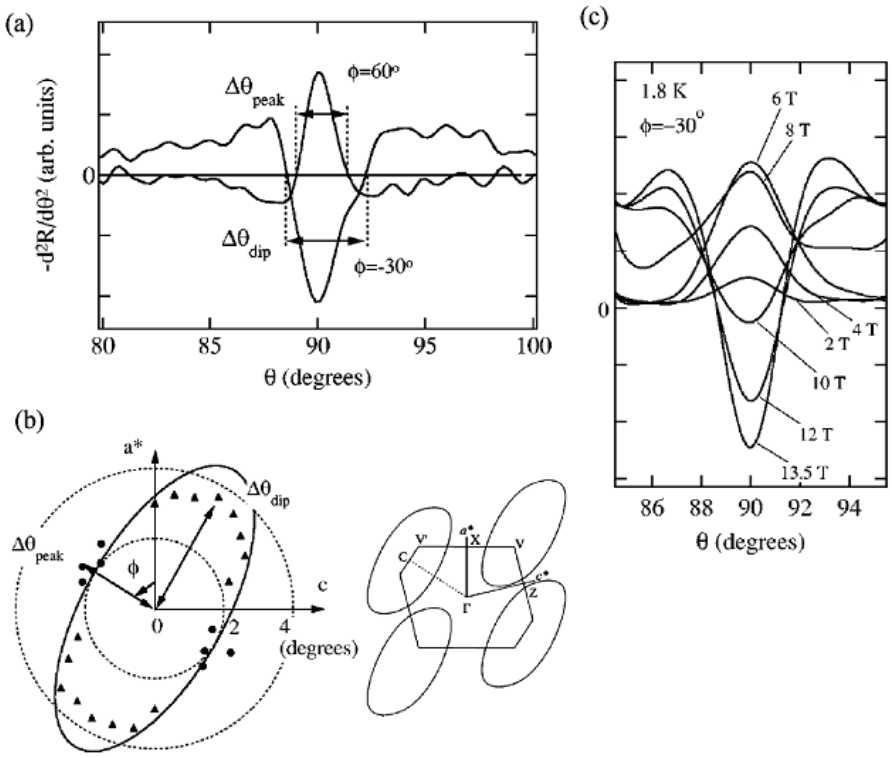

Figure 1.13: (a) Second derivative curves of the resistance for $(BEDT\text{-}TTF)_2Br(DIA)$ at 13.8 T. Peak and dip structures are seen in the angular dependences of the resistance. (b) Fermi surface in the a^*c-plane and a polar-plot of the widths of the peak ($\Delta\theta_{\rm peak}$) and dip $\Delta\theta_{\rm dip}$. (c) Second derivative curve of the resistance at azimuthal angle of $\phi = -30°$. The dip at $\theta = 90°$ appears at high fields and the peak appears at low fields.[40]

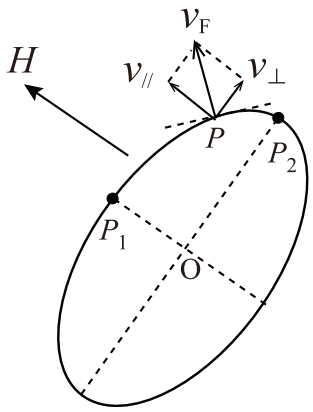

Figure 1.14: (a) A 2D Fermi surface. The Fermi velocity v_F at an arbitrary point P, which is perpendicular to the tangential line.

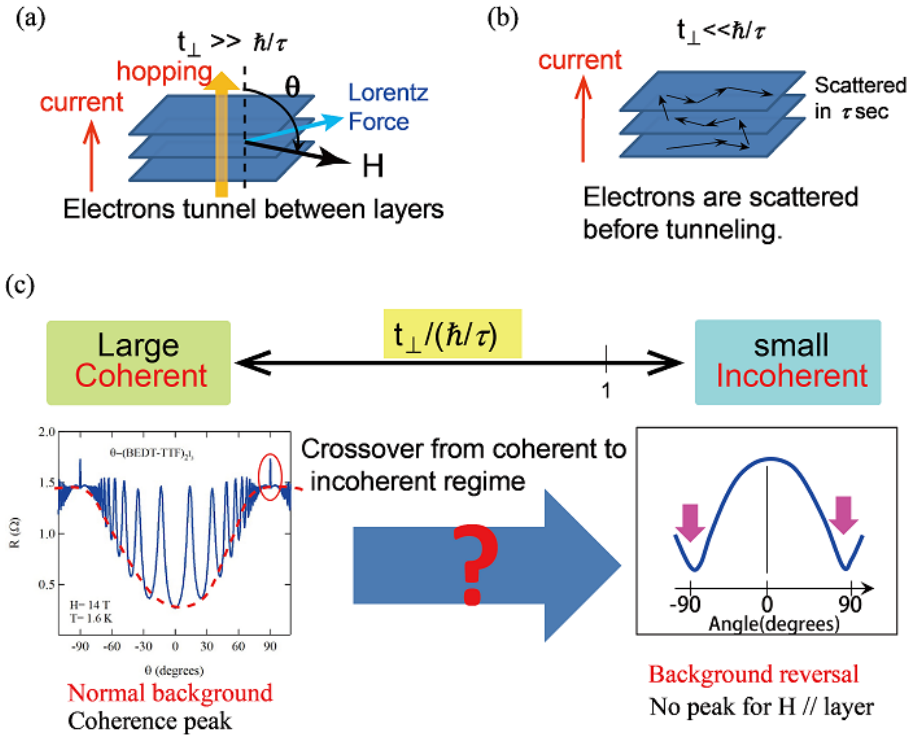

Figure 1.15: Schematics of (a) coherent and (b) incoherent interlayer transport. (c) MR behavior in the incoherent and coherent interlayer regimes.

1.3 Materials investigated

1.3.1 π-d organic conductors κ-(BDH-TTP)$_2$FeX$_4$ (X = Br, Cl)

π-d systems

To date, many π-d systems, following novel designs, have been investigated, although most of them are insulators or semiconductors at low temperatures because of electronic instability. The exceptions are κ-(BETS)$_2$FeBr$_4$ (X = Br, Cl),[42,43] λ-(BETS)$_2$Fe$_x$Ga$_{1-x}$Cl$_4$,[44] (EDO-TTFVO)$_2$FeCl$_4$,[45] (EDO-TTFVODS)$_2$FeBr$_4$,[46] (EDT-DSDTFVSDS)$_2$FeBr$_4$,[47] (EDT-DSDTFVO)$_2$FeX$_4$ (X = Br , Cl),[48] and β''-(EDO-TTFVODS)$_2$FeBr$_4$(SCE)$_{0.15}$,[49] which exhibit metallic or superconducting behavior at low temperatures. Another important feature of these salts is the low dimensionality of the electronic states. Because of this feature, peculiar behavior has been observed in superconducting,[22,50] and magnetic properties in these salts.[25] These aspects require a special effort to find typical examples of metallic π-d systems, because the insulating or semiconducting states sweep away the intriguing phenomena that arise from the interplay between the electron transport and magnetism.

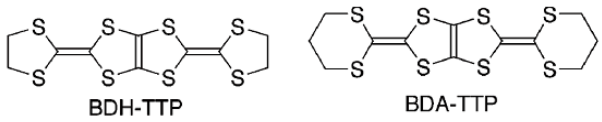

Figure 1.16: BDH-TTP and BDA-TTP

Over the last decade, the structurally similar BDA-TTP and BDH-TTP based π-d systems with tetrachloroferrates Fe(III)Cl$_4$ have been synthesized. The donors of 2,5-bis(1,3-dithian-2-ylidene)-1,3,4,6-tetrathiapentalene (BDA-TTP) and 2,5-bis(1,3-dithiolan-2-ylidene)-1,3,4,6-tetrathiapentalene (BDH-TTP) contain no TTF unit (Fig. 1.16).[51] The structures of β-(BDA-TTP)$_2$FeCl$_4$ and κ-(BDH-TTP)$_2$FeCl$_4$ are shown in Fig. 1.17(a) and 1.18(a), respectively. β-(BDA-TTP)$_2$FeCl$_4$ exhibits an metal-insulator (MI) transition at a high temperature (113 K) and has an AF order at $T_{\rm N} = 8.5$ K. The MI transition is suppressed with increasing pressure with superconductivity appearing above 4.5 kbar [Fig 1.17(b)].[52] In contrast, κ-(BDH-TTP)$_2$FeCl$_4$ (FeCl$_4$ salt) is metallic down to 1.5 K undergoing no magnetic transition as shown in Fig. 1.18(b).[53] In these salts, the $FeCl_4^-$ anions (Fe^{3+} ions) retain their large local magnetic moments, $S = 5/2$. Taking into account the structural similarity, the simple metallic behavior observed in the FeCl$_4$ salt indicates that the ratio of the transfer integral (bandwidth) to the electron correlation energy is larger than that in β-(BDA-TTP)$_2$FeCl$_4$. It is well known that intriguing phenomena arising from the enhanced interplay between the electron transport and magnetism can emerge when energy scales of both are comparable.[54] Therefore, reducing the bandwidth of the FeCl$_4$ salt would be of interest.

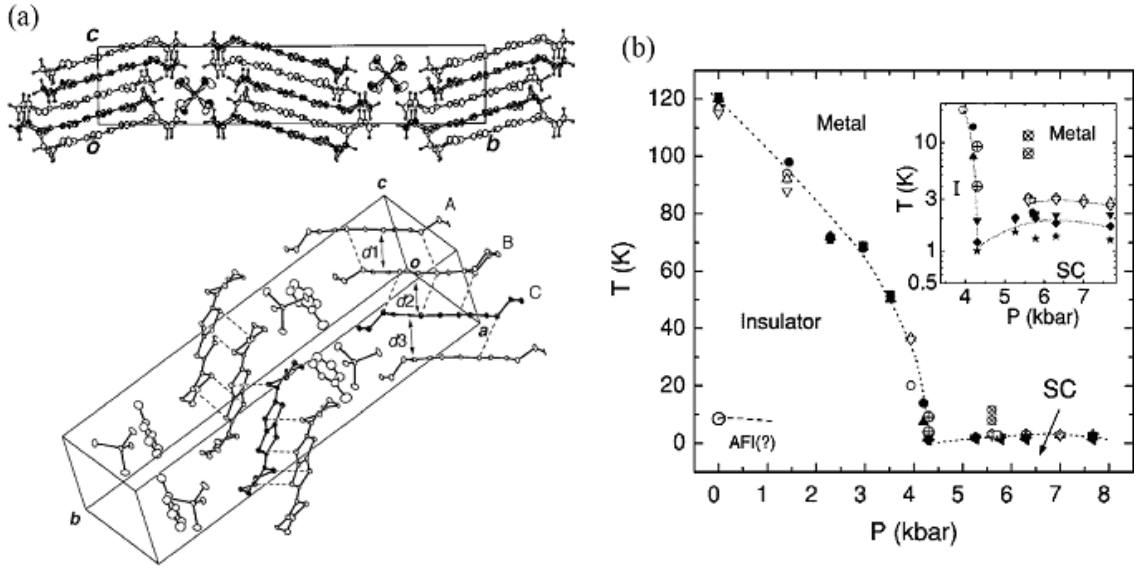

Figure 1.17: (a) Crystal structure of β-(BDA-TTP)$_2$FeCl$_4$. (b) Temperature-pressure phase diagram of β-(BDA-TTP)$_2$MCl$_4$ (M = Fe, Ga). The solid (open) symbols correspond to data for M = Fe (Ga).[52]

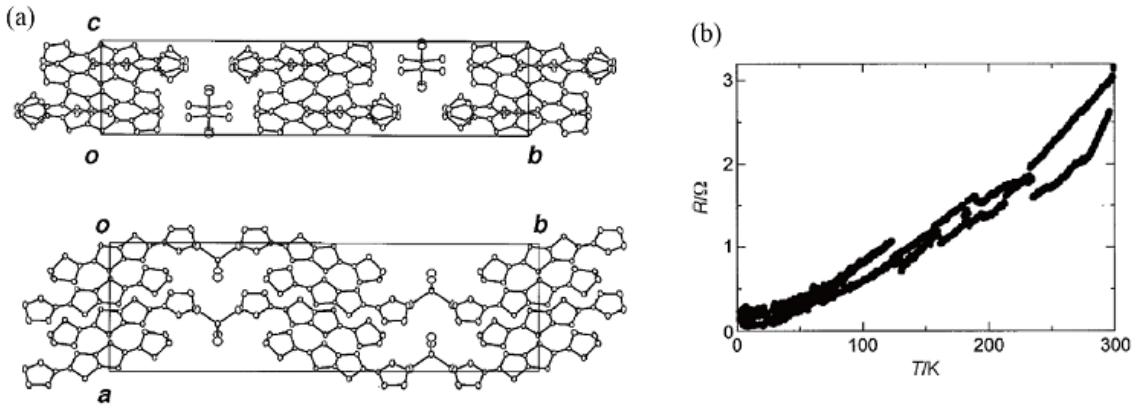

Figure 1.18: (a) Crystal structure of κ-(BDH-TTP)$_2$FeCl$_4$ viewed from the a-axis (upper) and the c-axis (lower). (b) Temperature dependence of the resistance for κ-(BDH-TTP)$_2$FeCl$_4$.[53]

BDH-TTP salts

Figure 1.19(a) shows the donor arrangement in the ac-plane for κ-(BDH-TTP)$_2$FeBr$_4$ (FeBr$_4$ salt). The donors form a dimerized structure, where the electronic interaction represented by the intradimer overlap integral $c1$ is responsible. The calculated overlap integrals are $c1$ = 19.0, $c2$ = 15.6, p = 6.31, and q = -6.64 $\times 10^{-3}$. These values are slightly smaller than those for the FeCl$_4$ salt, 19.3, 15.7, 6.36, and -6.79 $\times 10^{-3}$, respectively, showing the smaller bandwidth for the FeBr$_4$ salt. The intradimer overlap integral $c1$ is not much larger than the intermolecular integrals $c2$, p, and q; the BDH-TTP molecules are weekly dimerized compared with other κ-type salts.[43,55] The calculated band structure and Fermi surface of the FeBr$_4$ salt are shown in Figs. 1.19(c) and (d), respectively.[53] Because of the layered structure, the Fermi surface is highly 2D; a cylindrical Fermi surface that extends over

the Brillouin zone is formed, similar to those of the other κ phases, κ-$(BETS)_2FeCl_4$ and κ-$(BEDT\text{-}TTF)_2Cu(CN)_3$.[43,55] The isostructural $FeCl_4$ salt has a similar calculated band structure and Fermi surface. The values of the lattice parameters and the unit cell volume in the $FeBr_4$ salt are slightly larger (a: 0.8 %, b: 3.0 %, c: 0.1 %, and V: 4.0 %) than those in the $FeCl_4$ salt (a = 11.039, b = 37.471, c = 8.169 Å, and V = 3379 Å^3). The crystallographic data for both salts, obtained using the X-ray diffraction, are summarized in Table 1.1.

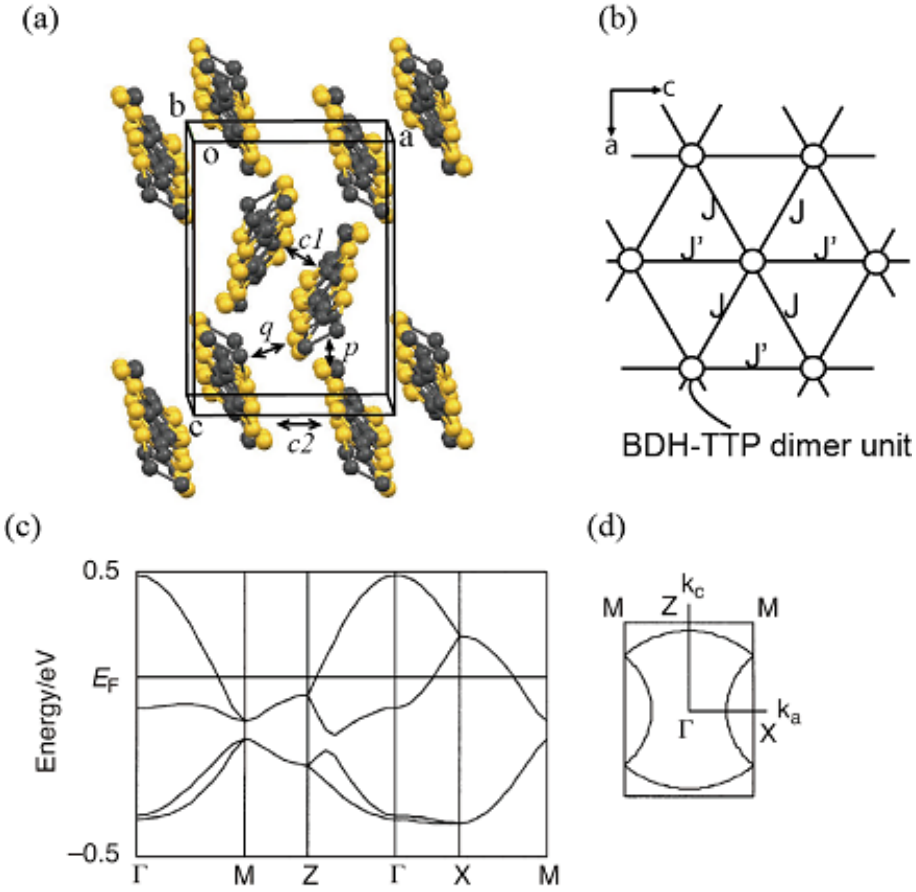

Figure 1.19: (a) BDH-TTP molecular arrangement. The overlap integrals for the $FeBr_4$ salt ($FeCl_4$ salt), $c1$, $c2$, p, and q are 19.0 (19.3), 15.6 (15.7), 6.31 (6.36), and −6.64 (−6.79) $\times 10^{-3}$, respectively. (b) Anisotropic triangular lattice of the BDH-TTP dimmers. (c) Energy bands and (d) Fermi surface calculated with the tight-binding approximation using the extended Hückel Hamiltonian.[53]

Table 1.1: Crystallographic data for κ-(BDH-TTP)$_2$FeBr$_4$ and κ-(BDH-TTP)$_2$FeCl$_4$.[53]

	κ-(BDH-TTP)$_2$FeBr$_4$ [a]	κ-(BDH-TTP)$_2$FeCl$_4$[53]
Formula	$C_{20}H_{16}S_{16}FeBr_4$	$C_{20}H_{16}S_{16}FeCl_4$
Formula weight	1144.77	966.94
Temperature (K)	298.2	295.2
Wave length (Å)	0.7107 (Mo Kα)	0.7107 (Mo Kα)
Crystal system	Orthorhombic	Orthorhombic
Space group	*Pnma*	*Pnma*
a (Å)	11.130(4)	11.0388(15)
b (Å)	38.598(3)	37.471(5)
c (Å)	8.177(4)	8.1693(10)
V	3513(2)	3379.1(8)
Z	4	4
D_{calc} (Mgm^{-3})	2.164	1.901
Total no. of reflections	4608	2490
No. of reflections observed ($I > 2\sigma(I)$)	2007	2094
No. of parameters	198	190
R_1, $_wR_2$	0.0424, 0.0400	0.0387, 0.0754
GOF	1.671	1.035

[a]Crystallographic data for both salts were obtained from the X-ray diffraction measurements performed by Assoc. Prof. J. Yamada and Dr. H. Akutsu at the University of Hyogo.

Calculation of the π-d interactions in the BDH-TTP salts

AF ordered structures and T_N in various π-d systems have been successfully explained in terms of the cooperation between the π-d and d-d exchange interactions, which are calculated from the overlap integrals.[56,57] The same procedure is followed in analyzing the spin structure of the present π-d system. The strengths of the calculated exchange interactions and T_N are summarized in Tables 1.2 and 1.3. The exchange interaction paths are indicated in Fig. 1.20(a). The strengths of all exchange interactions for the $FeBr_4$ salt are larger than those for the $FeCl_4$ salt. The calculated T_N are 4.00 K for the $FeBr_4$ salt and 1.33 K for the $FeCl_4$ salt (Table 1.3).

In the $FeBr_4$ salt, the direct d-d interaction (J_I/k_B) is estimated to be 0.31 K, along the a-axis [Fig. 1.20(a)]. This gives the exchange energy $E_J = 2J_I zS(S+1)/3k_B = 3.62$ K with $z = 2$ (the number of the nearest neighbor sites) and $S = 5/2$. This direct interaction predominantly leads to an antiparallel spin arrangement along the a-axis. In contrast, there are six π-d interactions (J_1 - J_6), the largest one of which, J_4 (J_4/k_B= 3.93 K) governs the dominant AF interaction between the Fe $3d$ and π spins (Table 1.2). The largest overlap integral $c2$ determines the AF coupling between the π dimer sites along the c-axis. Therefore, the possible spin alignment along the c-axis is AF, given by the $3d$ - J_4 - π dimer - $c2$ - π dimer -J_4 - $3d$ path, as shown in Fig. 1.20(a). Along the interlayer direction (b-axis), the strongest interaction between the $3d$ spins in the same unit cell is given by the $3d$ - J_4- π dimer - J_4 - $3d$ path, establishing the ferromagnetic (F) coupling. Consequently, the $3d$ spin configuration are proposed, as depicted in Figs. 1.20(a) and (b).

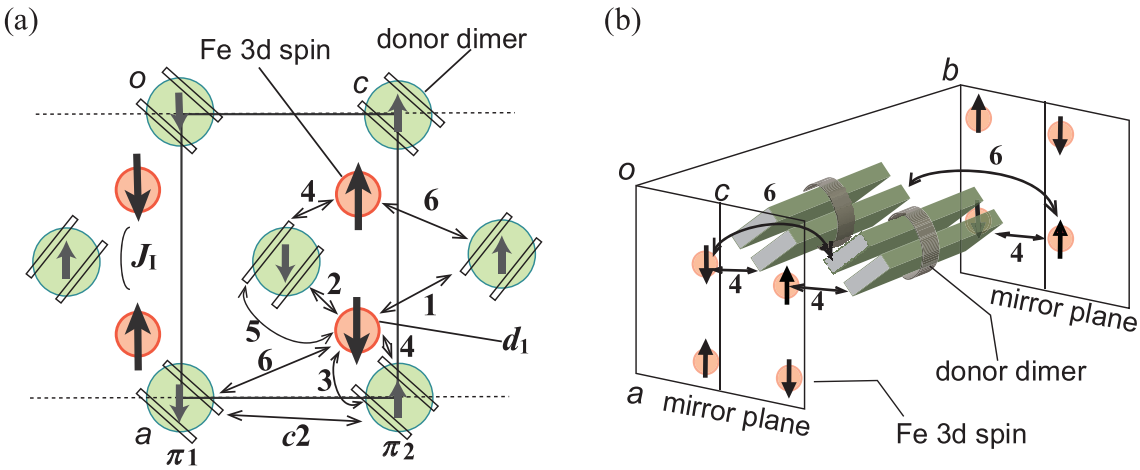

Figure 1.20: (a) Possible spin structures and definitions of the six π-d interactions (J_1 - J_6). (b) Dominant interaction paths along the b-axis.

Table 1.2: Calculated π-d and d-d interactions for κ-(BDH-TTP)$_2$FeBr$_4$ and κ-(BDH-TTP)$_2$FeCl$_4$. The interaction paths are indicated in Fig. 1.20(a).

		κ-(BDH-TTP)$_2$FeBr$_4$	κ-(BDH-TTP)$_2$FeCl$_4$
		$J/k_{\rm B}$ (K)	$J/k_{\rm B}$ (K)
π-d [b]	1	0.03	0.01
	2	0.07	0.05
	3	0.20	0.17
	4	3.93	1.76
	5	0.14	0.07
	6	1.10	0.78
d-d [b]	I	0.31	0.11

Table 1.3: Total π-d interactions and Néel temperatures calculated from the individual interactions for κ-(BDH-TTP)$_2$FeBr$_4$ and κ-(BDH-TTP)$_2$FeCl$_4$.

	κ-(BDH-TTP)$_2$FeBr$_4$	κ-(BDH-TTP)$_2$FeCl$_4$
$J_{\pi-d}$ [c]	8.32 K	3.88 K
$J'_{\pi-d}$ [c]	2.62 K	1.80 K
J_d [d]	0.62 K	0.22 K
x [e]	0.057	0.021
J (direct) [f]	3.62 K	1.28 K
J (indirect) [f]	0.38 K	0.050 K
$T_{\rm N}$ [f]	4.00 K	1.34 K

[b] Calculated by Assoc. Prof. T. Mori at the Tokyo Institute of Technology.[56,57]

[c] $J_{\pi-d} = 2J_1 + 2J_3 + 2J_4$ and $J'_{\pi-d} = 2J_2 + 2J_5 + 2J_6$ are the cooperative and frustrating π-d interactions, respectively.

[d] Total d-d interaction is given by $J_d = 2J_{\rm I}$.

[e] x is the π spin polarization factor given by $x = 5M_\pi/M_d = (5\chi_q/2k_{\rm B}C_\pi)|J'_{\pi-d} - J_{\pi-d}|$ where χ_q and C_π are the staggered susceptibility and the Curie constant for the π electrons. $x = 1$ for the case of the entirely localized spins. Here, $C_\pi/\chi_q = 500$ K is assumed, which is obtained for λ-(BETS)$_2$FeCl$_4$.

[f] From the mean-field theory for $S = 5/2$, $T_{\rm N}$ is given by $k_{\rm B}T_{\rm N} = (35/6)|J'_d - J_d| + (35/6)\cdot(\chi_q/2k_{\rm B}C_\pi)\,(J'_{\pi-d} - J_{\pi-d})^2$. The first term is the contribution of the direct d-d interaction and second term is the indirect π-d interaction. $J_{\pi-d}$ and $J'_{\pi-d}$ are the cooperative and frustrating π-d interactions. For these salts, $J'_d = 0$.

1.3.2 α-(BEDT-TTF)$_2$NH$_4$Hg(SCN)$_4$

Isostructural α-(BEDT-TTF)$_2$MHg(SCN)$_4$ (M = K, Tl, Rb, and NH$_4$) salts have attracted interest because of their low-temperature properties. α-(BEDT-TTF)$_2$NH$_4$Hg(SCN)$_4$ (NH$_4$ salt) produces a superconducting transition at ∼1 K. However, the other salts are metallic down to low temperatures with a magnetic transition at approximately 10 K. Some experimental studies have suggested that the ground states of the K, Tl, and Rb salts are density-wave states.

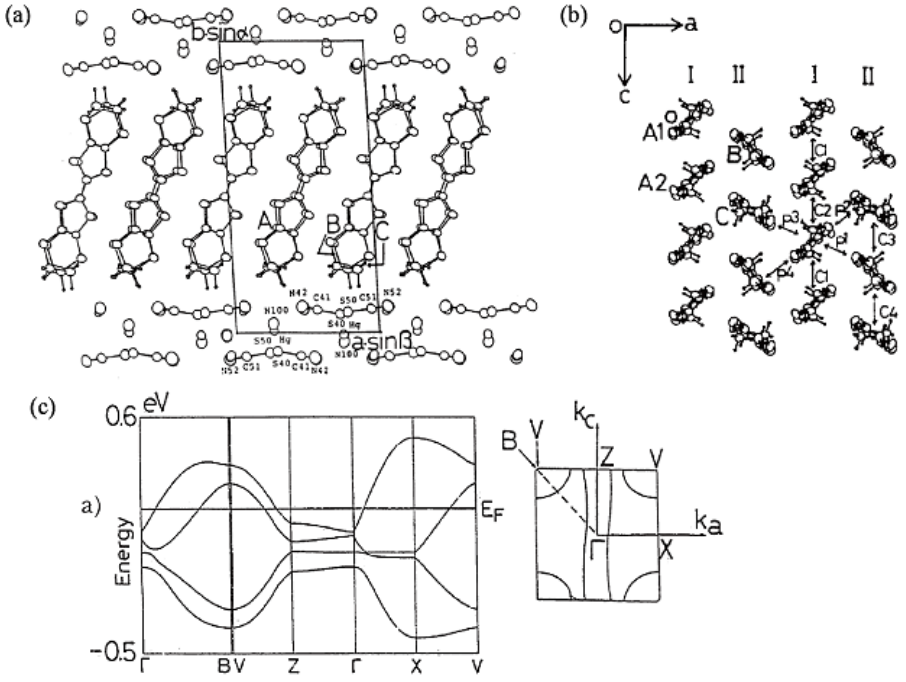

Figure 1.21: (a) Crystal structure, (b) donor arrangement, (c) calculated band structure, and Fermi surface for α-(BEDT-TTF)$_2$NH$_4$Hg(SCN)$_4$.[58] The overlap integrals are $c1 = -2.4$, $c2 = 5.9$, $c3 = -0.5$, $c4 = -0.1$, $p1 = -8.8$, $p2 = -9.5$, $p3 = 13.7$, and $p4 = 13.5$ ($\times 10^{-3}$).

The crystal structure for the NH$_4$ salt is shown in Fig. 1.21(a) and (b).[58] This salt has a layered structure, where the donor layers and anion layers are alternately stacked along the b-axis. The structure is triclinic and the unit cell angles are $\alpha = 103.65°$, $\beta = 90.53°$, and $\gamma = 93.30°$. The side-by-side S—S contacts of the donor molecules form a 2D network in the ac-plane [Fig. 1.21(b)]. The transverse overlap integrals $p1$-$p4$ are larger than those along the stacking direction ($c1$-$c4$), corresponding to the q1D structure. In consequence of the anisotropic structure, the NH$_4$ salt has anisotropic Fermi surfaces, one of which is a pair of 1D Fermi surfaces along the k_c direction and the other is a 2D cylindrical Fermi surface as shown in Fig. 1.21(c).

The Shubnikov-de Haas (SdH) oscillations for the NH$_4$ salt, shown in Fig. 1.22(a), have an oscillation frequency corresponding to the 2D α orbit.[59] The oscillation amplitude is reduced by increasing temperature, which gives the effective mass of the electron. The mass plot in Fig. 1.22(b) reveals an effective mass ratio for the NH$_4$ salt of 2.5, which is larger than those of the other isostructural salts (∼1.5).[59] Thus, the electron correlation in the NH$_4$ salt is larger than the other salts.

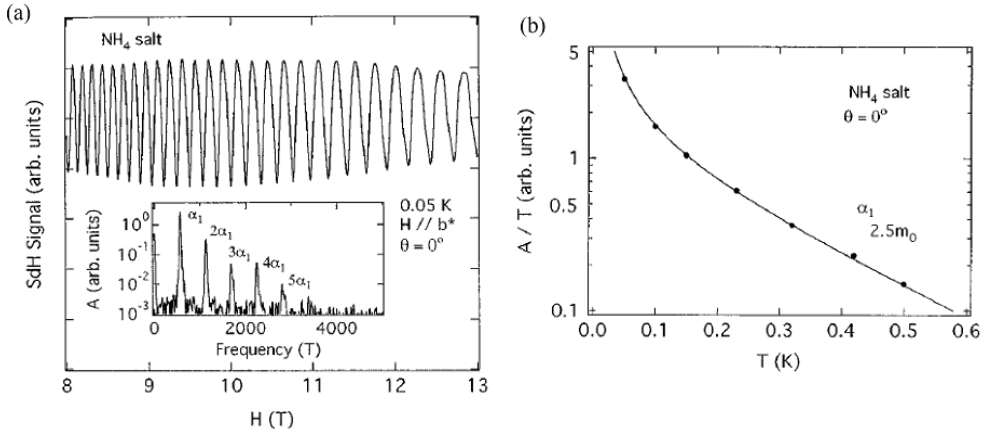

Figure 1.22: (a) SdH signal at 0.05 K and high fields for α-(BEDT-TTF)$_2$NH$_4$Hg(SCN)$_4$. The inset shows the FT spectrum of the signal. (b) Oscillation amplitude divided by temperature vs. temperature. The solid line is the fitted result using the LK formula.[59]

Figure 1.23(a) shows the angular dependences of the MR at various azimuthal angles.[60] The AMRO peaks are clearly observed. The 2D cylindrical Fermi surface, seen in Fig. 1.21(c), was experimentally confirmed from the polar plots of the peak positions.[60]

The interlayer transfer integral of the isostructural K salt is $t_z \approx 0.03$ meV, which is small for organic conductors.[41] The result indicates that the electronic state of the K salt is highly 2D. The NH_4 salt is also expected to have a small t_z, because of the structural similarity. Hence, the crossover from the incoherent to coherent interlayer transport can be observed for these systems when τ is changed. Furthermore, only the NH_4 salt is superconducting; the other salts form density-wave states at low temperatures. None of the magnetic transitions in the NH_4 salt are suitable for observing the interlayer transport crossover.

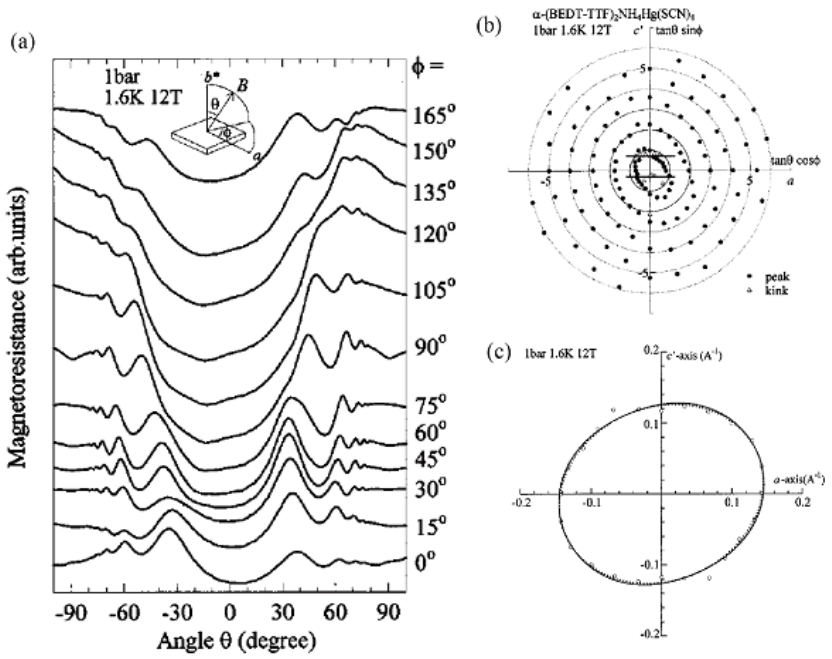

Figure 1.23: (a) Angular dependence of MR for α-(BEDT-TTF)$_2$NH$_4$Hg(SCN)$_4$. AMRO peaks clearly observed. (b) Polar plots of the AMRO peaks. (c) Cylindrical Fermi surface obtained from AMRO data.[60]

1.4 Purpose

In layered 2D organic conductors, the interlayer charge transport properties are well-known to show characteristic features in temperature and magnetic field dependent phenomena. Such phenomena are strongly affected by scattering caused by (1) local magnetic moments in the anion layers and (2) impurities (or defects) in the conducting layers. Despite the extensive experiments performed so far, detailed mechanisms of the characteristic phenomena in the interlayer charge transport remain unsolved problems. As high-quality single crystals can be produced, 2D organic conductors are good candidates to study the interlayer charge transport. For this thesis, two material systems with layered structures were chosen and systematic measurements of their electric and magnetic properties were obtained.

(1) Conductivity and magnetism in π-d organic conductors κ-(BDH-TTP)$_2$FeX$_4$ (X = Br, Cl)

In π-d systems, some interasting phenomena have been found, although most of them are insulators or semiconductors at low temperatures. κ-(BDH-TTP)$_2$FeX$_4$ (X = Br, Cl) are the candidates for metallic π-d systems. To clarify the effect of the large $3d$ magnetic moment on the metallic interlayer transport of the π spins, the magnetic susceptibility, X-band ESR, magnetic torque, and MR of both salts were investigated. The $FeBr_4$ salt appears to have the larger π-d and d-d interactions than the $FeCl_4$ salt. A comparison of the two salts will be made, and the physical properties caused by the π-d interaction elucidated.

(2) Incoherent interlayer charge transport in α-(BEDT-TTF)$_2$NH$_4$Hg(SCN)$_4$

The crossover from the incoherent to coherent behavior in the interlayer transport of 2D systems is known to take place when the interlayer transfer or scattering time is changed. However, no systematic investigations have been performed and how the crossover is induced remains unclear. α-(BEDT-TTF)$_2$NH$_4$Hg(SCN)$_4$ is a highly 2D organic superconductor, which has both 1D and 2D Fermi surfaces. To investigate the crossover from incoherent to weakly coherent interlayer transport in this system, the interlayer MR measurements were performed for many crystals with different quality. The angular dependences of the MR are expected to show large dependences on sample quality arising from the crossover phenomenon. The quality of each sample was quantitatively checked by the quantum oscillation measurements. The angular dependence of the MR and the temperature dependence of the resistance for various single crystals can provide much information on the coherence of the interlayer charge transport.

Chapter 2

Experimental Techniques and Measurements

2.1 Band-structure-measuring techniques

2.1.1 Landau quantization

The motion of the electrons in a magnetic field $\boldsymbol{H}$ depends on the Lorentz force acting on them,

$$\hbar\frac{d\boldsymbol{k}}{dt} = -e\boldsymbol{v} \times \boldsymbol{H}, \tag{2.1}$$

where $\boldsymbol{k}(t)$ is the electron wave vector. The velocity $\boldsymbol{v}$ is related to the electron energy ε by

$$\boldsymbol{v} = \frac{1}{\hbar}\frac{\partial\varepsilon(\boldsymbol{k})}{\partial\boldsymbol{k}}. \tag{2.2}$$

Equation (2.1) implies that the component of the electron wave vector parallel to $\boldsymbol{H}$ is a constant as $d\boldsymbol{k}/dt$ is perpendicular to $\boldsymbol{v}$. Hence $d\mathbf{k}/dt$ is perpendicular to $\partial\varepsilon(\boldsymbol{k})/\partial\boldsymbol{k}$,which means the energy associated with the electron orbit is constant. Therefore, the path of the electron orbit in k-space is defined by the intersections of surfaces of constant energy with planes perpendicular to $\boldsymbol{v}$. If the electron orbits are closed, the motion of the electron can be described using the cyclotron frequency ω_c,

$$\omega_c = \frac{eH}{m_c}, \tag{2.3}$$

where m_c is the cyclotron mass defined as

$$m_c = \frac{\hbar^2}{2\pi}\frac{\partial S_k}{\partial\varepsilon}, \tag{2.4}$$

with S_k being the k-space cross-sectional area of the closed orbit. The relationship between the area of the orbit in real space and k-space is

$$S_r = \left(\frac{\hbar}{eH}\right)^2 S_k. \tag{2.5}$$

The momentum of an electron under magnetic field is

$$\boldsymbol{p} = \hbar\boldsymbol{k} - e\boldsymbol{A}, \boldsymbol{H} = \nabla \times \boldsymbol{A}, \tag{2.6}$$

where $\boldsymbol{A}$ is the magnetic vector potential. From the Bohr quantization condition, the orbits for a electron subjected to an applied magnetic field are quantized as

$$\oint \boldsymbol{p} \cdot d\boldsymbol{r} = (n+\gamma)h = 2\pi(n+\gamma)\hbar, \tag{2.7}$$

where n is an integer and γ is a phase factor (γ is 1/2 for a free electron). Using eq. (2.6), a time-integrated version of Eq. (2.1), the Kelvin-Stokes theorem, and various vector identities, the left hand side of Eq. (2.7) becomes

$$\oint \boldsymbol{p} \cdot d\boldsymbol{r} = \oint \hbar \boldsymbol{k} \cdot d\boldsymbol{r} - \oint e\boldsymbol{A} \cdot d\boldsymbol{r} = -e \oint (\boldsymbol{r} \times \boldsymbol{H}) \cdot d\boldsymbol{r} - e \int (\nabla \times \boldsymbol{A}) \cdot d\boldsymbol{\sigma}$$
$$= e \oint \boldsymbol{H} \cdot (\boldsymbol{r} \times d\boldsymbol{r}) - e \int \boldsymbol{H} \cdot d\boldsymbol{\sigma} = 2e\Phi - e\Phi = e\Phi, \tag{2.8}$$

where Φ denotes the magnetic flux. As a result, from Eqs. (2.7) and (2.8), the flux is quantized,

$$\Phi = \frac{2\pi\hbar}{e}\left(n + \frac{1}{2}\right). \tag{2.9}$$

Here, from Eq.(2.5), the flux is expressed in k-space as

$$\Phi = HS_r = H\left(\frac{\hbar}{eH}\right)^2 S_k = \left(\frac{\hbar}{e}\right)^2 \frac{S_k}{H}. \tag{2.10}$$

Therefore, the relation between the orbital area in k-space and the magnetic field is given by

$$S_k = \left(n + \frac{1}{2}\right)\frac{2\pi e}{\hbar}H. \tag{2.11}$$

Separating k parallel and perpendicular components with respect to $\boldsymbol{H}$, the energy of a free electron is written as

$$\varepsilon = \frac{\hbar^2}{2m_e}(k_\parallel^2 + k_\perp^2) = \frac{\hbar^2}{2m_e}\left(\frac{S_k}{\pi} + k_\perp^2\right). \tag{2.12}$$

From Eqs. (2.12) and (2.11),

$$\varepsilon = \frac{\hbar eH}{m_e}\left(n + \frac{1}{2}\right) + \frac{\hbar^2}{2m_e}k_\perp^2. \tag{2.13}$$

In a 2D system, the second term in Eq. (2.13) is zero. Hence, we obtain

$$\varepsilon = \hbar\omega_c\left(n + \frac{1}{2}\right), \quad (n = 0, 1, 2, \cdots) \tag{2.14}$$

from which, we find that the electron energy is quantized in the magnetic field. The energy levels are called “ Landau levels ”.

2.1.2 Quantum oscillation in q2D conductors

In 3D systems (including the q2D case), the energy spectrum in the plane perpendicular to the field is degenerate. In k-space, the only permitted states for the electrons lie on so called “ Landau tubes ”. Each Landau tube crosses the Fermi level at different points.

In a magnetic field, the energy difference between adjacent Landau levels is obtained from Eq. (2.14) as

$$\Delta\varepsilon = \frac{\hbar eH}{m_e} = \hbar\omega_c. \tag{2.15}$$

Clearly, the energy difference between Landau levels is larger at higher fields than at lower fields. Hence, as the field increases, the gap between Landau levels widens. Next, we consider the density

of states (DOS) near the Fermi level. Electrons occupy the Landau levels up to the Fermi level. In forming the ground state, electrons occupy the states of the lowest Landau levels; the highest occupied level determines the Fermi level and in turn the energy of the Fermi level determines the Fermi surface. With increasing magnetic field, the number of occupied states in the highest Landau level (n), which lies inside the Fermi surface, decreases and vanishes rapidly when the Landau level touches the Fermi level. The electrons in the Landau level n fall to the lower $n-1$ level, and the total free energy decreases. As the field increases further, the free energy once again increases. This leads to a periodic variation in the free energy and the DOS. Consequently, oscillations occur in the physical properties such as magnetization, resistance, and heat capacity.

From Eq. (2.11), the number of Landau levels below the Fermi energy E_F is given by

$$n = \frac{E_F}{\hbar\omega_c} = \frac{\hbar}{2\pi e} S_F \frac{1}{H}. \tag{2.16}$$

Therefore, the oscillation frequency is given as

$$F = \frac{\Delta n}{\Delta(1/H)} = \frac{\hbar}{2\pi e} S_F. \tag{2.17}$$

The oscillation frequency is proportional to the cross-sectional area of the Fermi surface. Equation (2.17) also indicates that the interval of the oscillations is inversely proportional to the intensity of field.

These quantum oscillations are observed under extreme conditions such as low temperature and high field. At a finite temperature, the electrons are thermally excited, and the oscillation amplitude diminishes. Hence, to observe these oscillations, the thermal energy should be smaller than the period of the Landau levels,

$$kT \ll \hbar\omega_c. \tag{2.18}$$

Landau quantization requires the electron trajectories are closed orbits. However, if the electrons are scattered by impurities, phonons or other electrons, Landau quantization does not occur and no quantum oscillation appears. Thus, the scattering time of the electrons should be sufficiently longer than the cyclotron period, given by condition

$$\tau \gg 1/\omega_c, \tag{2.19}$$

or

$$\hbar/\tau \ll \hbar\omega_c. \tag{2.20}$$

Equation (2.20) requires the energy width of Landau levels from thermal broadening ($\hbar/\tau$) to be smaller than the energy gap between successive Landau levels.

2.1.3 Lifshitz-Kosevich formula

The general treatment of quantum oscillations in 3D metals was derived by Lifshitz and Kosevich.[61] Consider the Fermi surface as containing one extremal cross section perpendicular to the field. If the

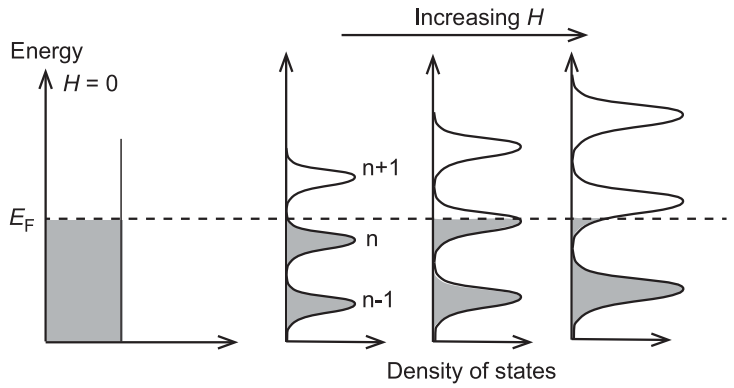

Figure 2.1: Schematic of Landau levels when magnetic field increases.

energy dispersion surface is assumed parabolic, the oscillatory part of the Gibbs potential, $\tilde{\Omega}$, can then be written as a sum of harmonics, which is periodic with scale $1/H$,

$$\tilde{\Omega} = (eH)^{5/2} \frac{V}{4\pi^4 m_c \hbar^{1/2}} \sum_{p=0}^{\infty} \frac{R_{\rm T} R_{\rm D} R_{\rm S}}{p^{5/2}} \cos\left[2\pi p\left(\frac{F}{H} - \frac{1}{2}\right) - \frac{\pi}{4}\right], \tag{2.21}$$

where V is the total volume of the sample, p denotes the pth harmonic for the fundamental frequency, and $R_{\rm T}$, $R_{\rm D}$, $R_{\rm S}$ are the damping factors that are associated with temperature, scattering, and spin, respectively.

The oscillatory part of the magnetization $\tilde{M}$ is obtained by field differentiation of $\tilde{\Omega}$ for constant chemical potential ξ. The longitudinal and transverse components of $\tilde{M}$ are given by

$$\tilde{M}_{\parallel} = -\left(\frac{\partial\tilde{\Omega}}{\partial H}\right)_{\xi}, \tag{2.22}$$

$$\tilde{M}_{\perp} = -\frac{1}{H}\left(\frac{\partial\tilde{\Omega}}{\partial\theta}\right)_{\xi,H} = -\frac{1}{F}\frac{\partial F}{\partial\theta}\tilde{M}_{\parallel}. \tag{2.23}$$

$$\tilde{M}_{\parallel} = -\frac{3}{2^{5/2}\pi} N_0 \beta_0 \left(\frac{H}{F}\right)^{1/2} \left[\sum_{p=0}^{\infty} \frac{R_{\rm T} R_{\rm D} R_{\rm S}}{p^{3/2}} \sin\left[2\pi p\left(\frac{F}{H} - \frac{1}{2}\right) - \frac{\pi}{4}\right]\right], \tag{2.24}$$

where $\beta_0 = e\hbar/m_c$, $N_0 = (V/3\pi^2)(2m_c\xi/\hbar^2)^{3/2}$.

The damping factors are written as

$$R_{\rm T} = \frac{Kp\mu T/H}{\sinh(Kp\mu T/H)}, \tag{2.25}$$

$$R_{\rm D} = \exp\left(-2\pi^2 p k_{\rm B} T_{\rm D}/\beta_0 H\right) = \exp\left(-Kp\mu T_{\rm D}/H\right), \tag{2.26}$$

$$R_{\rm S} = \cos\left(\frac{1}{2}p\pi g\mu\right), \tag{2.27}$$

where $T_{\rm D}$ is the Dingle temperature, which gives a measure of sample quality, g the spin-splitting factor, μ the effective mass ratio $\mu = m_c/m_e$, and $K = 2\pi^2 k_{\rm B} m_e/e\hbar \approx 14.7$. The Dingle temperature

is given by

$$T_{\rm D} = \frac{\hbar}{2\pi k_{\rm B}\tau}, \tag{2.28}$$

where τ is the scattering time averaged over the cyclotron orbit. Hence, a higher-quality sample has a longer τ, which infers a smaller $T_{\rm D}$.

As seen in the above, the amplitude of the oscillations is reduced by the damping factors. From the temperature dependence of the oscillation amplitude A, the $\ln(A/T)$ vs. T plot gives the effective mass ratio. The large scattering rate (large $T_{\rm D}$) also reduces the oscillation amplitude. $T_{\rm D}$ is obtained by measuring the field dependence of the oscillation amplitude, which for typical clean organic conductors is $\sim$1 K ($\sim$ 1 ps).

2.1.4 Angular-dependent magnetoresistance oscillation

When a magnetic field is applied to a 2D conductor, the angular dependence of the interlayer resistance exhibits an oscillation as shown in Fig. 2.2(a). The oscillation is called the angular-dependent magnetoresistance oscillation (AMRO or ADMRO); it does not depend on the strength of the field. but depends on its orientation. The AMRO was observed for the first time by Kajita *et al.* in the MR of an organic conductor θ-(BEDT-TTF)$_2$I$_3$.[62] The following theoretical explanation was given by Yamaji.[36] Consider a simple q2D band structure,

$$E(k) = \frac{\hbar^2}{2m_c}\left(k_x^2 + k_y^2\right) - 2t_z\cos\left(ck_z\right), \tag{2.29}$$

where k_x and k_y are the in-plane components of the wave vector k, and k_z is the perpendicular component of k, c is the length between the adjacent layers. In the magnetic field, the electrons are subjected to the Lorentz force, Eqs. (2.1) and (2.2). The intersection of the Fermi surface with the k_xk_z-plane is illustrated in Fig. 2.2(b). When the magnetic field H is inclined at an angle θ from the k_z-direction towards the k_x-direction, the trajectory of the semiclassical closed orbit is given by the intersection of the Fermi surface and the plane perpendicular to the field. That is,

$$k_x\sin\theta + k_z\cos\theta = p = k_z^{(0)}\cos\theta, \tag{2.30}$$

where $k_z^{(0)}$ is the point where the k_z-axis intersects the orbital plane. The area of the orbital plane S_k in k-space is calculated assuming that $t_z/E_F \ll 1$,

$$\begin{aligned} S_k\cos\theta &= \int_0^{\pi} d\phi\left\{k_F^2 + 4mt_z\cos\left[c\left(k_z^{(0)} - k_F\tan\theta\cos\phi\right)\right]\right\}, &(2.31)\\ &= S_F + 4\pi m_c t_z\cos(ck_z^{(0)})\cdot J_0\left(ck_F\tan\theta\right), &(2.32)\end{aligned}$$

where $S_F = \pi k_F^2$, and J_0 is the Bessel function $J_0(z) = (1/2\pi)\int_0^{2\pi}\cos(z\sin\theta)d\theta$. When $z \geq 1$, $J_0(z)$ is approximately $J_0(z) \approx (2/\pi z)^{1/2}\cos(z - \pi/4)$. Thus, when the condition

$$ck_F\tan\theta = \pi\left(n - 1/4\right) \quad (n = 1, 2, 3\cdots) \tag{2.33}$$

holds, S_k does not depend on $k_z^{(0)}$ because $S_k \cos\theta = \pi k_F^2$. Hence, the system can be regarded as being completely 2D at these θ values, and consequently, the resistance has a local maximum at these angles. This oscillation is called AMRO (sometimes also referred to as Yamaji oscillation or ADMRO) and the associated angle is called the Yamaji angle.

The velocity of the electrons along the z-axis is given by

$$v_z = \frac{\partial E}{\hbar \partial k_z} = \frac{2t_z c}{\hbar} \sin(k_z c). \tag{2.34}$$

The average of v_z over a cyclotron orbit is calculated as

$$\langle v_z \rangle = \oint v_z d\phi = \frac{2t_z c}{\hbar} J_0(ck_F \tan\theta) \sin(ck_z^{(0)}). \tag{2.35}$$

As factors $J_0(ck_F \tan\theta)$ and $\langle v_z \rangle$ are zeros at the Yamaji angle, the electrons are unable to move in the direction parallel to the z-axis. Hence the conductivity is zero (equivalently, the resistance show peaks) at the Yamaji angles.

From the periodicity of the AMRO peaks, as given by Eq. (2.33), we can extract k_F along the field direction. Thus, the in-plane Fermi surface can be obtained by the AMRO measurement.

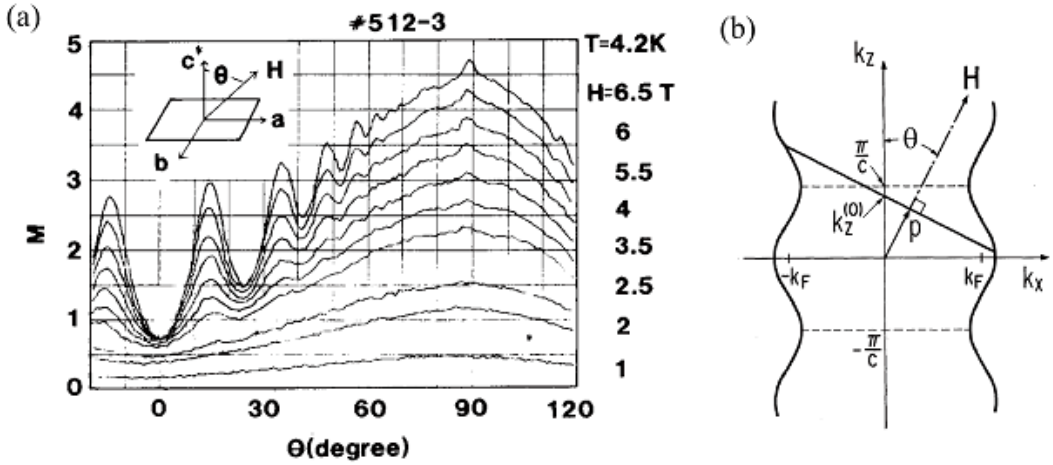

Figure 2.2: (a) MR of θ-(BEDT-TTF)$_2$I$_3$ against the magnetic field direction.[62] (b) Intersection of the Fermi surface with the $k_x k_z$-plane.[36]

2.1.5 Magnetoresistance in q2D conductors

Next, the MR behavior in q2D systems will be quantitatively explained using the Boltzmann transport theory. The energy dispersion in Eq. (2.29) gives the velocity components,

$$v_x = \frac{\hbar k_x}{m_c}, \quad v_y = \frac{\hbar k_y}{m_c}, \quad v_z = \frac{2t_z c}{\hbar} \sin k_z c. \tag{2.36}$$

The conductivity tensor for a charge particle in a magnetic field is given by

$$\sigma_{ij} = \frac{e^2}{4\pi^3} \oint \frac{dS}{\hbar |\boldsymbol{v}|} \int_0^\infty v_i(0) v_j(t) e^{-t/\tau} dt. \quad (i, j = x, y, z). \tag{2.37}$$

The velocity $\boldsymbol{v}$ along the orbit is integrated for each area element of the Fermi surface dS. These orbits are determined from the Lorentz equation, Eq. (2.1). When the field is inclined at an angle θ to the interlayer direction, we have

$$\hbar \frac{dk_z}{dt} = -ev_0 H \sin\theta, \tag{2.38}$$

where v_0 is the in-plane Fermi velocity ($v_0 = v_x = v_y$), which is assumed to be constant. For this case, k_y ($k_x = k_y$) is a constant. By integrating Eq. (2.38),

$$ck_z(t) = ck_z(0) + \Omega_c t \sin\theta, \tag{2.39}$$

where the frequency Ω_c is given by $\Omega_c = ev_0 cH/\hbar$, at which the fastest quasiparticles traverse the Brillouin zone. Ω_c can also be ascribed using the cyclotron frequency $\omega_c = eH/m_c$ [Eq. (2.3)] as $\Omega_c = k_y c\omega_c$. Equations (2.36) and (2.39) give the velocity in the c direction,

$$v_c(t) = \frac{2t_z c}{\hbar} \sin\left[ck_z(0) + \Omega_c t \sin\theta\right]. \tag{2.40}$$

By integrating Eq. (2.37), the conductivity can be obtained:

$$\begin{aligned} \sigma_{zz}(H) &= \sigma_{zz}^0 \Big\{ J_0^2(ck_F \tan\theta) + \sum_{\nu=1}^{\infty} \frac{2J_\nu^2(ck_F \tan\theta)}{1 + (\nu\omega_c\tau\cos\theta)^2} \Big\}. \\ \sigma_{zz}^0 &= \frac{2e^2 m_c t_z^2 c\tau}{\pi\hbar^4} = \left(\frac{\tilde{v}_z}{v_F}\right)^2 \frac{Ne^2\tau}{m_c}, \end{aligned} \tag{2.41}$$

where J_ν is the νth order Bessel function (shown in the previous subsection), N is the density of electrons, and $\tilde{v}_z = 2t_z c/\hbar$. The summation term diminishes with increasing $\omega_c\tau$ (increasing field), hence the conductivity at high fields is governed by the first term. The conductivity shows a minimum at the Yamaji angles because of the $J_0^2(ck_F \tan\theta)$ term. The angular and magnetic field dependence of the resistivity $\rho_{zz}(H) = 1/\sigma_{zz}(H)$ are shown in Fig. 2.3. As $\omega_c\tau$ decreases (H or τ decreases), the AMRO peaks diminish [Fig. 2.3(a)].

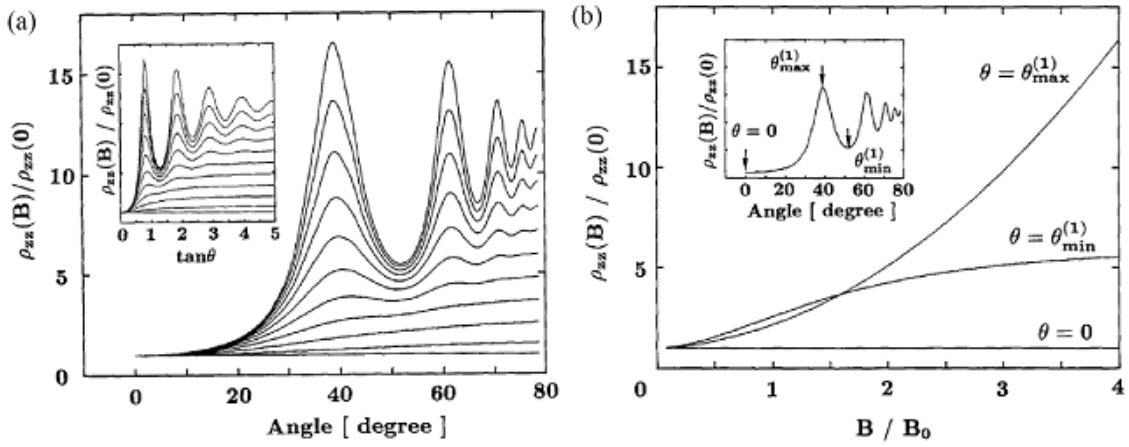

Figure 2.3: (a) Interlayer MR for different magnetic fields. From top to bottom, the value of $\omega_0\tau$ varies from 4 to 0 with step interval of 0.4. The parameter settings are $E_F/t_z = 100$ and $m_c t_z c^2/\hbar^2 = 0.045$. (b) Magnetic field dependence of the interlayer MR at fixed angles. $B/B_0 = \omega_c\tau$. The positions of $\theta^{(1)}_{min}$ and $\theta^{(1)}_{max}$ are indicated in the inset.[37]

2.2 Experimental and analysis techniques

2.2.1 Helium refrigerator

For this study, two Oxford 20T superconducting magnets and a 17T superconducting magnet were used. The 17T superconducting magnet system combined with a ^{4}He cryostat can cool the sample space down to 1.6 K.

^{3}He cryostat

The 20T superconducting magnet system is combined with a ^{3}He cryostat, in which samples are cooled down to 0.3 K. Figure 2.4 shows the operating principle of the ^{3}He cryostat. In the condenser (or " 1 K pot "), the ^{4}He gas is pumped and cooled down to around 1 K.

The ^{3}He gas is absorbed by cooling the sorption pump, and the gas can be emitted by heating the pump. Most of the ^{3}He gas can be cooled and condensed near the condenser. The sorption pump is then cooled, reducing the vapor pressure above the liquid ^{3}He. The sample space can then be cooled to around 0.3 K.

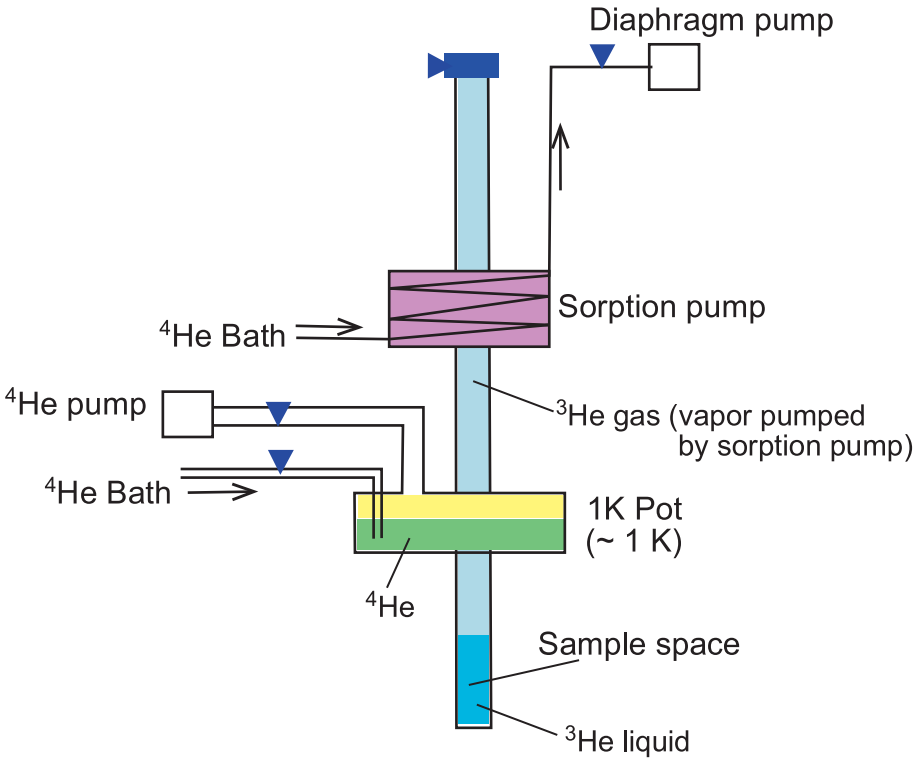

Figure 2.4: Schematic diagram of the ^{3}He cryostat.

Dilution refrigerator

The second 20T superconducting magnet system is combined with a ^{3}He dilution refrigerator, which can continuously cool samples down to ∼30 mK.

Figure 2.5 shows a schematic diagram of the refrigerator. In the condenser, the ^{4}He gas is pumped and cooled to ∼1 K. The heat exchangers allow the heat to pass from the mixture to the condenser, effectively cooling the mixture. The ^{4}He gas passes continuously through the bath via a needle valve (impedance) and into the condenser. The mixture flows through the “Still”, which is maintained at ∼0.6 K. Through the heat exchanger, the mixture transfers its heat to the Still and is cooled. Next, the mixture flows past the “Cold Plate”, where more heat is transferred from the mixture, until the mixture ends up in the “Mixing Chamber”.

In the Mixing Chamber, the ^{3}He - ^{4}He mixture separates into two phases, the ^{3}He-rich phase (^{3}He concentrated, the upper phase, comprising almost 100 % ^{3}He) and the ^{4}He-rich phase (^{3}He dilute, the lower phase, which has 6.6 % ^{3}He). The ^{3}He dilute phase is pumped into the Still and the ^{3}He liquid in the concentrated phase is transferred into the dilute phase. The system then gains entropy and is cooled to 20-30 mK.

In the Still, only ^{3}He is distilled from the mixture and pumped out of the Still as gas. The ^{3}He gas is then pumped back to the beginning of the system, where it is mixed with the incoming ^{3}He and ^{4}He gases. Eventually, the ^{3}He sources are closed off and essentially only ^{3}He is circulating through the main part of the cryostat.

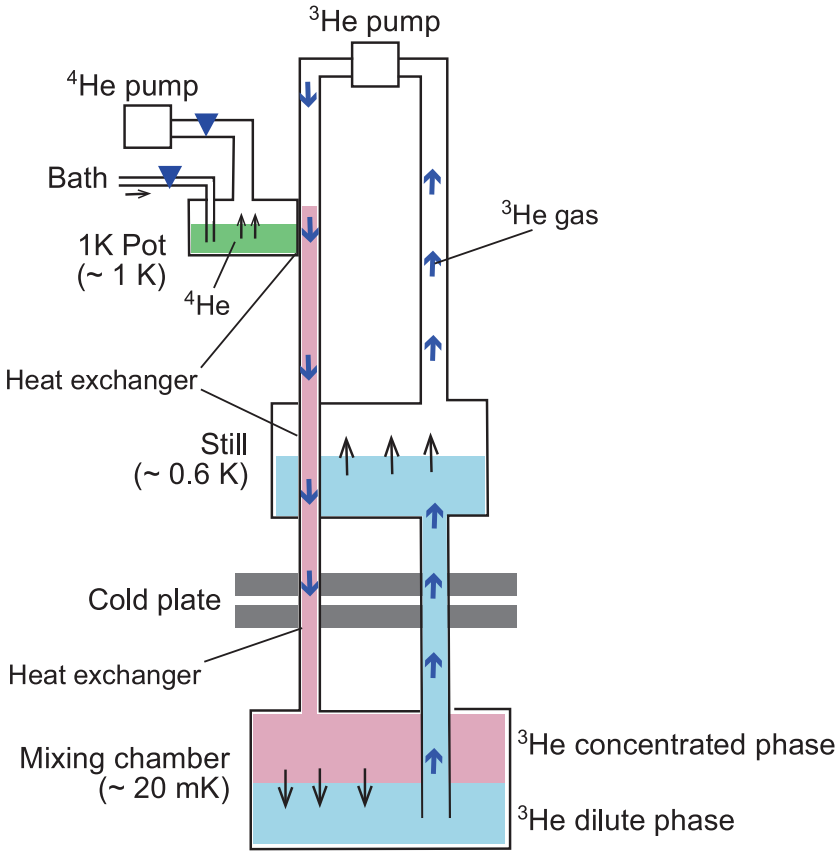

Figure 2.5: Schematic diagram of the ^{3}He dilution refrigerator.

2.2.2 Electron spin resonance measurements

Principle

The magnetic moment of a single free electron is described by $\mu_s = -g\mu_{\rm B}S$. In a magnetic field H, the energy difference ΔU between the two spin states, corresponding to the magnetic spin component $m_s = \frac{1}{2}, -\frac{1}{2}$, called as Zeeman energy, is given by

$$\Delta U = g\mu_{\rm B}H\left(\frac{1}{2}\right) - g\mu_{\rm B}H\left(-\frac{1}{2}\right) = g\mu_B H. \tag{2.42}$$

Consider microwave radiation of frequency ν interacting with an electron. If the energy of the microwave equals the Zeeman energy, an electron in the $m_s = -\frac{1}{2}$ state absorbs the microwave energy, and is excited into the $m_s = \frac{1}{2}$ state. This phenomenon is called electron spin resonance (ESR) or electron paramagnetic resonance (EPR). The condition for resonance is

$$h\nu = g\mu_{\rm B}H. \tag{2.43}$$

We shall investigate the resonance as a function of the frequency ω for constant magnetic fields H_0. The absorption spectrum is obtained by taking the Fourier transformation of the spin correlation function. We assume that the resonance frequency $\omega(t, r)$ fluctuates about an average value. The spin correlation function for ω is given by

$$\Psi(\tau) = \frac{\langle\omega(\tau)\omega(0)\rangle}{\langle\omega(0)^2\rangle}, \tag{2.44}$$

where $\langle\omega(0)^2\rangle$ is the second moment of the absorption spectrum, and is expressed as $\omega_d = \sqrt{\langle\omega(0)^2\rangle}$.

According to the Kubo-Tomita theory,[63] the Fourier transformation (ϕ) of the absorption spectrum is

$$\phi(t) = \exp\left(-\omega_d^2\int_0^t (t-\tau)\Psi(\tau)d\tau\right). \tag{2.45}$$

When only the dipole-dipole interaction is considered between spins, we can take $\Psi(\tau) = 1$ because ω does not depend on time; $\omega(t) = \omega(0)$. Thus,

$$\phi(t) = \exp\left(-\frac{\omega_d^2 t^2}{2}\right) \tag{2.46}$$

is obtained. The Fourier transformation for $\phi(t)$ gives the resonance absorption spectrum I(ω),

$$\mathrm{I}(\omega) = \frac{1}{\sqrt{2\pi}\omega_d}\exp\left(-\frac{(\omega-\omega_0)^2}{2\omega_d^2}\right). \tag{2.47}$$

This function is a Gaussian.

Next, we consider the strong exchange interaction effects on the spins. On time scales of $J/\hbar(=\omega_e)$, the spin information is lost because of the exchange interaction J. Hence, the spin correlation function is, for example, given by

$$\Psi(\tau) = \exp\bigl(-\omega_e^2\tau^2\bigr), \tag{2.48}$$

which rapidly decreases at $\tau \sim 1/\omega_e$. For simplicity, the spin correlation function is assumed to have form

$$\Psi(\tau) = \begin{cases} 1 & (0 < \tau < 1/\omega_e), \\ 0 & (\tau > 1/\omega_e), \end{cases} \tag{2.49}$$

for which Eq. (2.45) becomes

$$\phi(\tau) = \exp\left(-\frac{\omega_d^2|t|}{\omega_e}\right). \tag{2.50}$$

If we assume $\omega_e \gg \omega_d$, from the Fourier transform of Eq. (2.50), the absorption spectrum is obtained as

$$\mathrm{I}(\omega) = \frac{\omega_d^2/\omega_e}{\pi}\left\{\frac{1}{(\omega-\omega_0)^2 + (\omega_d^2/\omega_e)^2}\right\}. \tag{2.51}$$

This spectrum has Lorentzian form. The type of function thus depends on the properties of $\Psi(\tau)$. When $\omega_e \neq 0$, the linewidth ω_d becomes narrower (ω_d^2/ω_e) because of the motion of the electron. This is called motional narrowing (exchange narrowing).

The phase difference between spins becomes entirely random on time scales greater than some T_2, called the spin-spin relaxation time. The spin system relaxes its energy obtained from the microwave radiation via thermal equilibrium with the lattice system. The time scale for this relaxation defines the spin-lattice relaxation time (T_1). The total relaxation time is given by

$$\frac{1}{T} = \frac{1}{T_2} + \frac{1}{2T_1}. \tag{2.52}$$

Parameters obtained from ESR

The ESR signal is obtained from the differential of the absorption.

***g* -value**

The g-value is obtained experimentally from the resonance field using Eq. (2.43). For a free electrons, $g = 2$. If strong spin-orbit coupling exists, the g-value differs from $g = 2$. In particular, the rare-earth metals exhibit g-values different largely from 2 owing to the orbital motion. If an atomic system has an unpaired spin in a p, d, or f orbit, the distribution of the electron is anisotropic, and resonance fields in each field direction are different from each other. Hence the g-values are anisotropic.

Linewidth

An electron is affected, not only by the external field, but also by local magnetic fields H_{loc} arising from the dipole-dipole interaction with other electrons. This H_{loc} can be a source of the linewidth, which is time-modulated. The second moment is given by

$$\langle \Delta H^2 \rangle = (3/4)\mu^2 \Sigma_{j,k} \frac{(3\cos^2\theta_{j,k} - 1)}{r_{j,k}^6}, \tag{2.53}$$

where j and k index the electrons, $r_{j,k}$ is the distance between the spins, and $\theta_{j,k}$ is the angle between the vector $r_{j,k}$ and the field. The absorption reduces to Gaussian when only the dipole-dipole

interactions are taken into account. The relation between the second moment and the peak-to-peak linewidth is then given by

$$\Delta H_{\rm pp} = 2\sqrt{\langle \Delta H^2 \rangle}. \tag{2.54}$$

If two or more paramagnetic different ions exist, two absorption spectra are expected because of the different g-values of the ions. However, if the exchange interaction is also taken into account, only one absorption line can be observed because of the exchange narrowing. The absorption line is near the average of the resonance fields for two ions.

Integrated amplitude

The amplitude of the absorption I is proportional to the imaginary part of the susceptibility χ''. The amplitude $S_{\rm I}$ of the absorption spectrum $I(\nu)$ can be defined as the area of the absorption spectrum,

$$S_{\rm I} = \int I(\nu) d\nu \approx \nu_0 C \int \frac{\chi''(\nu)}{\nu} d\nu. \tag{2.55}$$

From the Kramers-Kronig relation, we can obtain

$$(2/\pi) \int \frac{\chi''}{\nu} d\nu = \chi_0, \tag{2.56}$$

where χ_0 is the static susceptibility of the sample. Thus, we obtain the relation

$$S_{\rm I} = \frac{\pi \nu_0}{2} C \chi_0, \tag{2.57}$$

which implies that the absorption line and the integrated amplitude are proportional to the static susceptibility.

2.2.3 Magnetic torque measurements

Principle

When the magnetization is parallel to the easy-axis, the electron energy is lower than when the magnetization is parallel to the hard-axis. This difference between the electron energies is defined as the magnetic anisotropy. A magnetic torque is induced on the sample when the magnetic field is not exactly parallel to the magnetic moment of the sample. In other words, the magnetic anisotropy induces a force that changes the direction of the magnetic field.

For the paramagnetic phase, the magnetization $\boldsymbol{M}$ induced by a field $\boldsymbol{H}$ is given by $\boldsymbol{M} = \chi \boldsymbol{H}$, where χ is the 3×3 magnetic susceptibility tensor. As the magnetic susceptibility for a paramagnet is independent of the magnetic field, the magnetic anisotropy energy is expressible as

$$E_a = \int_0^M HM = \frac{1}{2} H \chi H = \frac{1}{2} MH. \tag{2.58}$$

When the field $\boldsymbol{H}$ is rotated in the xy-plane, $\boldsymbol{H}$ can be written using the field angle θ, $\boldsymbol{H} = (H\cos\theta, H\sin\theta, 0)$. The magnetic susceptibility has diagonal form, and the magnetization vector

can be written as

$$\boldsymbol{M} = \begin{pmatrix} M_x \\ M_y \\ M_z \end{pmatrix} = \begin{pmatrix} \chi_x & 0 & 0 \\ 0 & \chi_y & 0 \\ 0 & 0 & \chi_z \end{pmatrix} \begin{pmatrix} H_x \\ H_y \\ H_z \end{pmatrix}. \tag{2.59}$$

Hence, the magnetic anisotropy energy is

$$E_a = \frac{1}{2}\left(\chi_x \cos^2\theta + \chi_y \sin^2\theta\right) H^2. \tag{2.60}$$

The magnetic torque is given by the differential of the free energy in the field angle,

$$\tau = -\frac{\partial E}{\partial \theta} = \int \frac{\partial M}{\partial \theta} dH = \frac{1}{2}(\chi_x - \chi_y) H^2 \sin 2\theta. \tag{2.61}$$

That is, the magnetic torque exhibits a periodicity of 180°, and is proportional to the square of the field. From the magnetic torque, we obtain the anisotropy of the susceptibility, $\chi_x - \chi_y$.

Figure 2.7 shows the angular dependence of the magnetic torque for α-(BEDT-TTF)$_2$KHg(SeCN)$_4$.[65] The torque curves show a $\sin 2\theta$ dependence in accordance with Eq. (2.61).

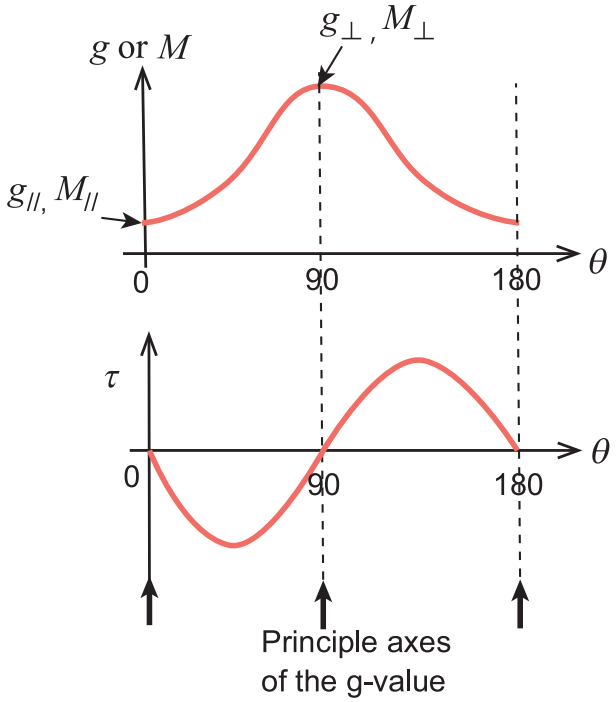

Figure 2.6: Angular dependences of the g-value (or magnetization) and the magnetic torque for a paramagnetic phase. τ is zero at the maximum and minimum of the g-value.

For an antiferromagnetic phase, the total magnetization is the sum of the magnetizations for the two spin sublattices. The magnetic anisotropy energy is given by $\frac{1}{2}(\chi_\perp - \chi_\parallel)$, where $\chi_\perp$ and $\chi_\parallel$ are the respective magnetic susceptibilities when the field is perpendicular and parallel to the easy-axis. With increasing field parallel to the easy-axis, the magnetization exhibits a jump because of the anisotropy in magnetic energy. An example of a plot between the magnetization (M) and H is shown in Fig.

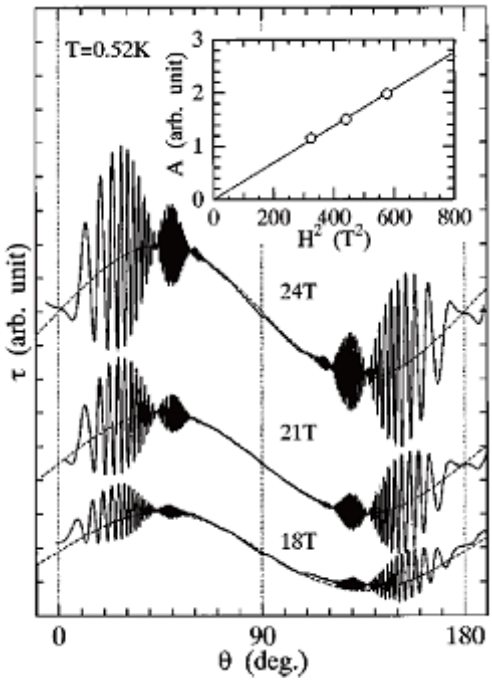

Figure 2.7: Angular dependence of the magnetic torque for α-(BEDT-TTF)$_2$KHg(SeCN)$_4$. The broken curves show the $\sin 2\theta$ dependence. The inset presents the H^2 dependence of the torque amplitude.[65]

2.8 (a). At the zero field, the spins are ordered antiferromagnetically. At the spin-flop transition field $H_{\rm SF}$, the spins rapidly change direction, corresponding to the jump in magnetization, as illustrated in Fig. 2.8 (c). At high fields, the spins are aligned parallel to the field, and the magnetization becomes saturated.

In contrast, with increasing field perpendicular to the easy-axis, the spins gradually change direction, and are aligned with the field direction at high fields [Fig. 2.8 (b)]. Thus, the M-H curve shows a monotonic increase up to the saturation field.

Figure 2.9 shows the field dependences of the magnetic torque for λ-(BETS)$_2$FeCl$_4$, which has an AF phase at low temperatures.[64] A rapid change of τ is observed at $H_{\rm SF}$ for the field nearly parallel to the easy axis. The slope of the τ-H curves become constant above 10 T, corresponding to $H_{\rm sat}$.

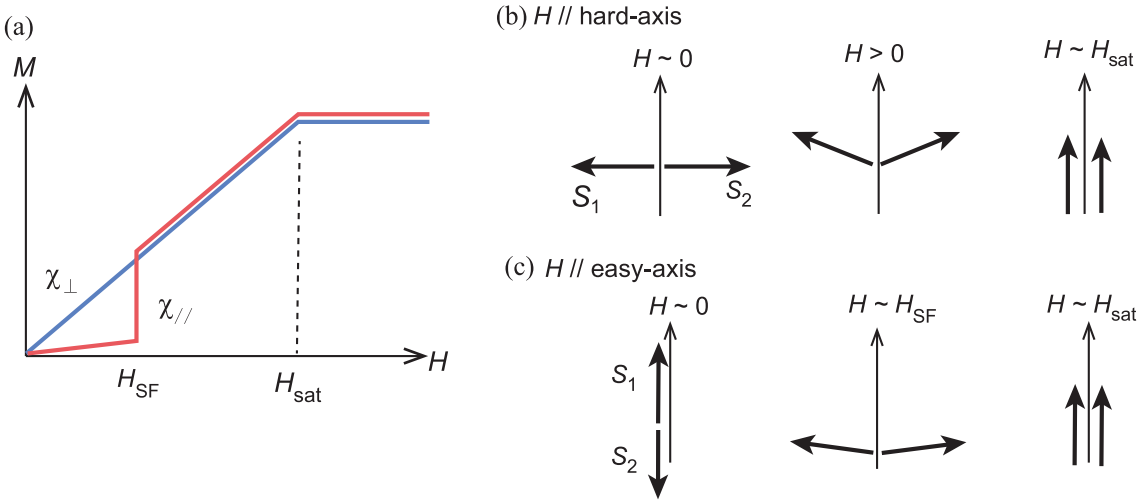

Figure 2.8: (a) Magnetization curves of an antiferromagnetic system. H_{SF} and H_{sat} are the spin-flop field and saturation field, respectively. (b) Schematics of the spins when the field is parallel to the magnetic hard-axis and (c) the easy-axis.

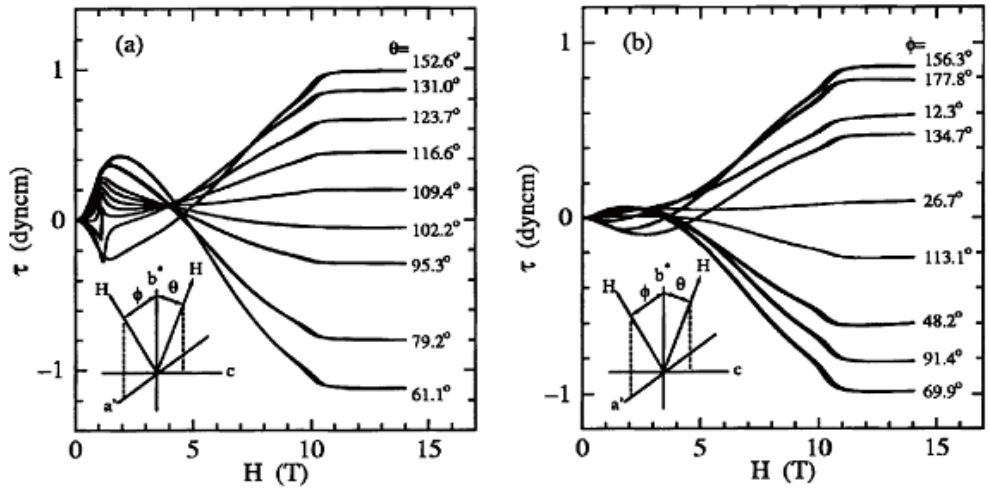

Figure 2.9: Field dependence of the magnetic torque for λ-$(\mathrm{BETS})_2\mathrm{FeCl}_4$ at 0.45 K. θ and ϕ are the field angles tilted from the b^*-axis to the c- and a'-axes, respectively.[64]

Measurements

In this study, the magnetic torque was measured using an AFM micro-cantilever (SII-SS-ML-PRC400, Seiko Instruments, Japan).[65] A small amount of silicon grease was used to attach single crystal samples to the cantilever as seen in Fig. 2.10 (a). Figure 2.10 (b) shows the resistance bridge circuit for the torque measurement. Under an applied magnetic field, the resistance changes as the cantilever bends from both the magnetic torque of the sample and gravity. The relative change in the resistance $R_{\mathrm{sample}}/(R_{\mathrm{reference}} + R_{\mathrm{sample}})$ is proportional to the magnetic torque. Hence, the change in the voltage ratio V_{AB}/V_{CD} yields the change in the magnetic torque.

In general, the magnetic susceptibility measurements provide important microscopic information on the magnetic properties in the 3d spin state. A SQUID magnetometer, for instance, is known as a quite sensitive tool to probe the magnetic properties, but it can be carried out in limited temperature and field regions. In addition, a microcantilever enables us to precisely measure the magnetic torque even for a tiny single crystal, and serves as a convenient and powerful tool to elucidate the magnetic properties at very low temperatures and high magnetic fields.[66–73]

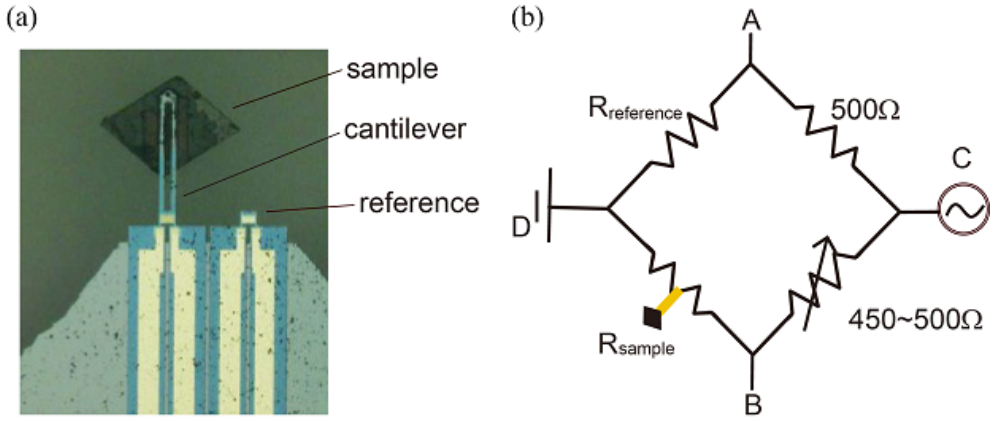

Figure 2.10: (a) Setting of the sample for magnetic torque measurements. (b) The resistance bridge circuit. C represents the ac current and D is the ground. The voltage difference between A and B was measured.

2.3 Experimental details

2.3.1 π-d organic conductors κ-(BDH-TTP)$_2$FeX$_4$ (X = Br, Cl)

The BDH-TTP donor was synthesized following an established procedure.[74] Single crystals of κ-(BDH-TTP)$_2$FeX$_4$ (X = Br, Cl) were grown by electrocrystallization of BDH-TTP (0.0125 mol) with either Et_4NFeBr_4 or Et_4NFeCl_4 (0.05 mmol) in a solvent of 10% acetone/chlorobenzene (17 mL) under an argon atmosphere. The application of a constant current of 0.15 μA for 20-30 days produced thin black plate-like crystals. The BDH-TTP and single crystals were synthesized with the Yamada group at the University of Hyogo and the Enoki group at the Tokyo Institute of Technology.

The magnetic susceptibility was measured using a SQUID magnetometer (MPMS-7, Quantum Design) up to 7 T in the temperature range of 2-300 K. Several single crystals were aligned along the crystal axes for the measurements. The core diamagnetism was subtracted from the raw data.

X-band ESR spectra were measured in the range of 3.5-300 K with a microwave power of 0.6 mW using a X-band EPR spectrometer (TE-200, JEOL) equipped with an helium continuous-flow cryostat (ESR910, Oxford Instruments). The single crystals were aligned on a silicon rod with a small amount of Apiezon N grease and sealed in a quartz tube under a $\sim$50 mbar helium atmosphere (exchange gas) for the low-temperature measurements.

The resistance and the MR were measured using the conventional four-probe ac technique down to 30 mK. Current was applied along the inter-plane direction (b-axis). The electrical contacts were made with carbon paste and thin gold wires (ϕ = 10 μm). The samples were covered with Apiezon N grease to avoid micro cracks forming during the cooling process. The magnetic field was applied using a 20T superconducting magnet.

The magnetic torque τ was measured using microcantilevers.[65] The measurements were carried out in a superconducting magnet and at low temperatures generated by either a dilution refrigerator or a ^{3}He cryostat. The magnetic field was rotated in the ab- and cb-planes of the crystals.

The de Haas-van Alphen (dHvA) effect of the magnetic torque for the $FeCl_4$ salt was measured using microcantilevers in fields up to 35 T and temperatures down to 0.5 K. The magnetic field was applied using a solenoid magnet equipped with a ^{3}He cryostat at the National High Magnetic Field Laboratory (NHMFL) in Tallahassee, USA. The dHvA measurements were performed with the cooperation of Prof. J. S. Brooks and Dr. D. Graf at the NHMFL.

2.3.2 α-(BEDT-TTF)$_2$NH$_4$Hg(SCN)$_4$

The single crystals of α-(BEDT-TTF)$_2$NH$_4$Hg(SCN)$_4$ were synthesized by Kanoda Laboratory at The University of Tokyo.

The interlayer resistivity was measured using the conventional four-terminal method and the applied ac current was 1$\sim$10 μA. For all nine crystals, the AMROs were measured by the two-axis-rotator in magnetic fields at 1.6 K. The applied magnetic fields of up to 15 T were generated using the 17T

superconducting magnet.

For the same crystals, the measurements of the Shubnikov-de Haas (SdH) oscillations were conducted at temperatures down to 0.3 K. Fields of up to 17.5 T were applied using the 20T superconducting magnet equipped with the ^{3}He cryostat. Current was applied along the interplane direction (b-axis). The electrical contacts were made with carbon paste and thin gold wires.

Chapter 3

Results and Discussion for κ-(BDH-TTP)$_2$FeX$_4$ (X =Br, Cl)

3.1 Results for κ-(BDH-TTP)$_2$FeBr$_4$

3.1.1 Magnetic properties

The temperature dependences of the magnetic susceptibility χ and χT at 0.5 T along all crystallographic axes are shown in Figs. 3.1(a) and (b), respectively. As the temperature decreases, the susceptibilities monotonically increase and then show peaks at 3.9 K. Above 20 K, the susceptibilities can be well fitted by the Curie-Weiss law $\chi = C/(T - \Theta)$. The best-fit parameters, used in producing the three curves, are presented in Fig. 3.2, and are $C_a = 4.53$, $C_b = 4.55$, $C_c = 4.65$ emu·K·mol^{-1}, $\Theta_a = -1.1$ K, $\Theta_b = -3.3$ K, and $\Theta_c = -3.4$ K, where the subscripts indicate the field direction. The deviation from the Curie-Weiss law is evident below 20 K. The Curie constant of $\sim$4.6 emu·K·mol^{-1} shows that the susceptibility is dominated by the localized Fe 3d spins of $S = 5/2$ as the Pauli paramagnetic susceptibility arising from the conduction π electrons is negligible ($\sim 10^{-4}$ emu·mol^{-1}). Therefore, the sharp peaks of the magnetic susceptibilities are ascribed to an AF transition of the 3d spins ($T_N = 3.9$ K), taking into account the negative Weiss temperature of -1.1 - -3.4 K. Note that, with the anisotropy axis along the a-axis, the uniaxial anisotropy along the a-axis appears even well above T_N. Specifically, the susceptibility for $H \parallel a$ is largest above T_N and then shows a steepest decrease below T_N. In contrast, the susceptibilities for $H \parallel b$ and $H \parallel c$ behave almost the same. The behavior of the susceptibility near the AF transition cannot be explained in terms of a simple collinear AF structure in the ordered state, but it suggests a canted-spin structure.[75,76]

The magnetization (M) vs. H plots at 2 K and 5 K are presented in Figs. 3.3(a) and (b), respectively. For $H \parallel a$, a steep increase at 1.5 T is evident, which can be ascribed to a spin-flop transition of the Fe 3d spins ($H_{SF} = 1.5$ T) with the magnetic easy axis along the a-axis. For $H \parallel b$ and $H \parallel c$, the magnetization curves increase more gradually with H, but the curvatures change slightly (inflection points) at 3.1 T (H_c). These changes are more evident in the differential curves (dM/dH), and are likely caused by weak ferromagnetic (WF) transitions (spin canting) along these axes. Using linear fits to the M-H curves below and above H_c, it is estimated that the WF moment induced at the transition is about 0.35 μ_B per a 3d spin for both $H \parallel b$ and $H \parallel c$. Above T_N, the M-H curves become smooth with no indication of any field-induced transition, as seen for the curve at 5 K [Fig. 3.3(b)].

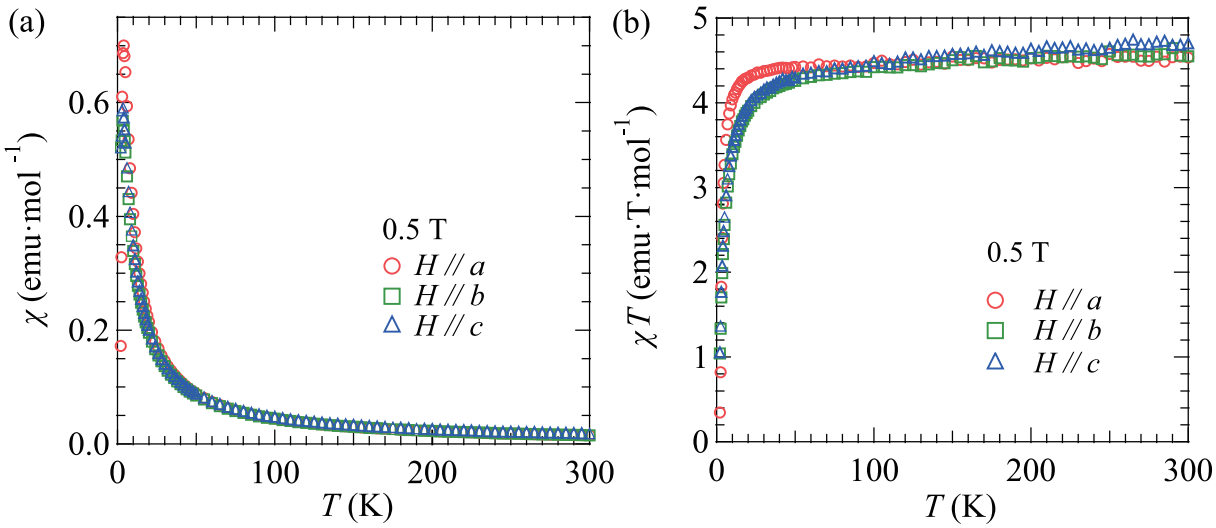

Figure 3.1: Temperature dependences of the magnetic susceptibilities χ for κ-(BDH-TTP)$_2$FeBr$_4$ for $H = 0.5$ T along all crystal axes. (b) χT vs. T plot.

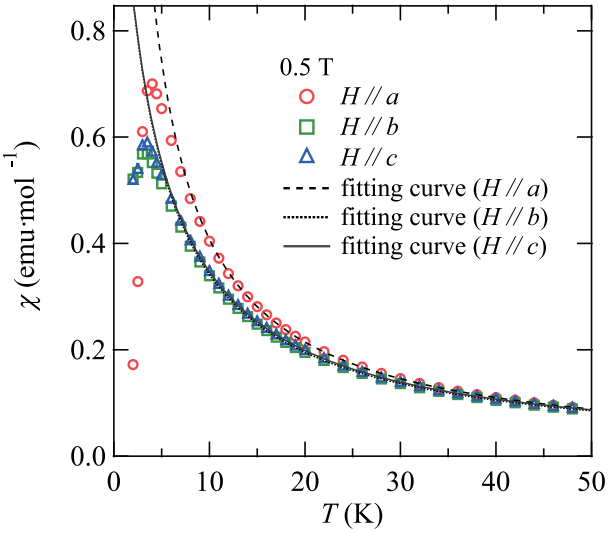

Figure 3.2: Low-temperature data (below 50 K) of the magnetic susceptibilities for κ-(BDH-TTP)$_2$FeBr$_4$ at $H = 0.5$ T. The dashed, dotted, and solid lines show the Curie-Weiss law $\chi_i = C_i/(T - \Theta_i)$, where $i = (a, b, c)$.

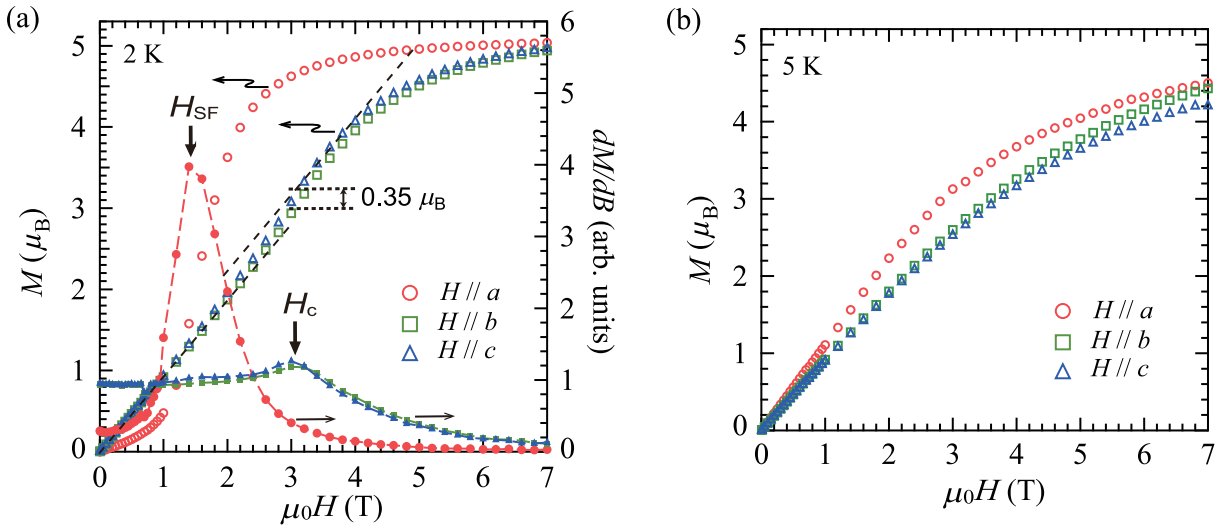

Figure 3.3: Magnetization vs. field plot for κ-(BDH-TTP)$_2$FeBr$_4$ measured at (a) 2 K and (b) 5 K along the three crystallographic directions. The differential curves, dM/dH are also shown in (a).

An ESR signal with a single Lorentzian lineshape is observed down to about 20 K. At temperatures below 20 K, an additional small sharp signal appears on the high field side ($g \approx 2.002$) of the main broad signal [see inset in Fig. 3.4(a)]. The sharp signal is ascribed to impurities because of its very small intensity (only about 0.01 percent of the main signal intensity at 31 K). The observed Lorentzian-shaped single ESR signal proves that the exchange narrowing occurs, and the d electron spins are coupled via the exchange interaction.

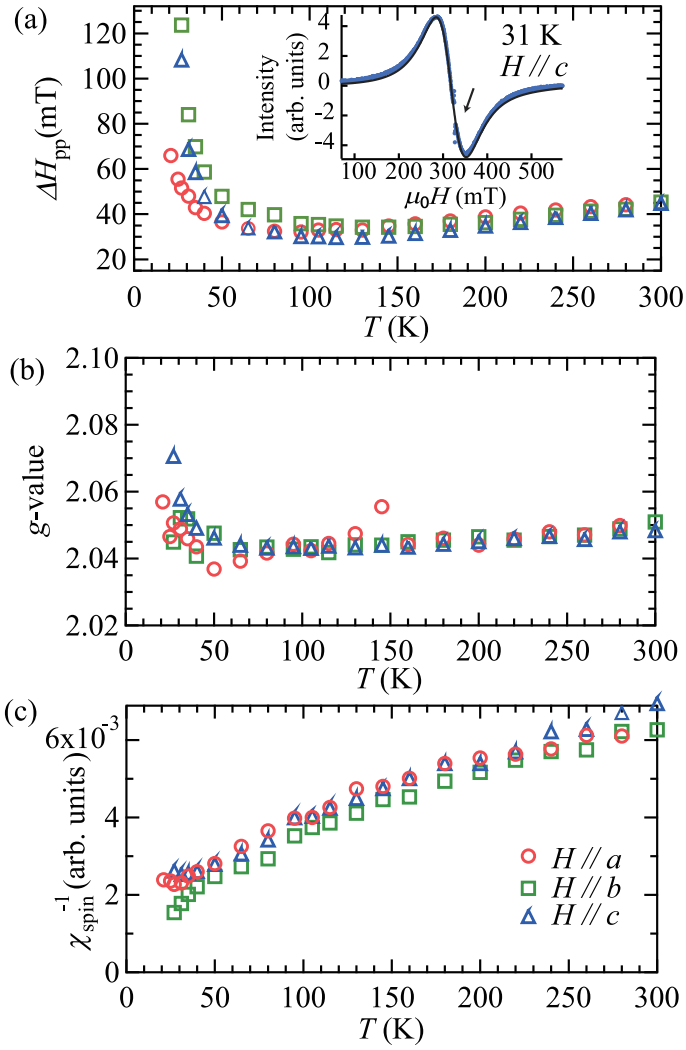

Figure 3.4: Temperature dependences of (a) the ESR linewidth ΔH_{pp}, (b) the g-value, and (c) the inverse spin susceptibility χ_{spin}^{-1} of κ-(BDH-TTP)$_2$FeBr$_4$ for the three crystallographic directions. Inset: ESR signal at 31 K. The solid curve represents the fitted Lorentzian curve. An arrow indicates the small signal arising from impurities.

The temperature dependence of the ESR linewidth (ΔH_{pp}), the g-value, and the inverse of the ESR intensity corresponding to the spin susceptibility (χ_{spin}^{-1}) are shown in Figs. 3.4(a), (b), and (c), respectively, with the field aligned along the three crystallographic axes. For all field directions, the linewidth gradually decreases with decreasing temperature, and then diverges as temperatures fall below 100 K. The linewidth becomes too wide to observe below 25 K. The divergent behavior is

more pronounced for $H \parallel b$ and $H \parallel c$. The g-values, while almost temperature independent above 50 K, slightly increase below 50 K. The divergent behavior of the linewidth at low temperatures is likely because of critical phenomena associated with the AF transition at 3.9 K. The inverse spin susceptibility $\chi_{\rm spin}^{-1}$ roughly shows a T-linear behavior, consistent with the static susceptibility [Fig. 3.1(a)].

The angular dependences of the linewidth at 110 K and 30 K are shown in Figs. 3.5(a) and (b), respectively. At 110 K, the angular dependences can be expressed in the functional form $A + B\cos^2\theta$ with maxima obtained for $H \parallel b$ as shown by solid and dashed curves, for H in the bc- and ba-planes, respectively. At 30 K, the critical phenomena governs the spin system, and the angular dependence deviates from the conventional sinusoidal form, particularly in the behavior for $H \parallel a$, for which the linewidth drops sharply.

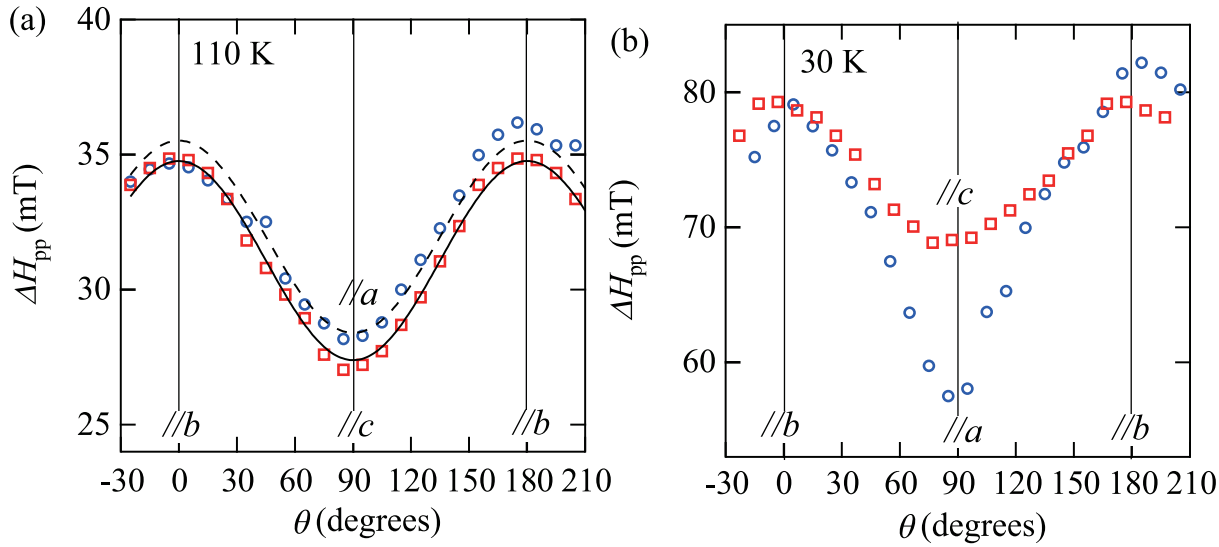

Figure 3.5: Angular dependences of the linewidth $\Delta H_{\rm pp}$ for κ-(BDH-TTP)$_2$FeBr$_4$ at (a) 110 K, and (b) 30 K. The magnetic fields are rotated in either the bc-plane (circles) or the ba- plane (squares). Dashed and solid lines are the fitting curves for the ba- and bc- planes, respectively, using $\Delta H_{\rm pp} = A + B\cos^2\theta$.

3.1.2 Resistance and magnetoresistance

The resistivity monotonically decreases with decreasing temperature over the entire temperature range as shown in Fig. 3.6. No sign of superconducting transition is observed down to 30 mK [inset of Fig. 3.6]. Here, data for the typical κ-phase superconductors, κ-(BEDT-TTF)$_2$Cu(NCS)$_2$ and κ-(BETS)$_2$FeBr$_4$ are instructive. They show broad resistance peaks at $\sim$100 and 60 K, respectively.[43,77] With increasing hydrostatic pressure, the two peaks are smeared out and disappear at 3 kbar and 5 kbar, respectively,[77,78] and are associated with the suppression of superconductivity. These results strongly suggest that the electron correlation effect, which is likely related to the superconducting mechanism and the broad peak, is reduced through the band broadening induced by the hydrostatic pressure. From analysis of κ-salts, we conclude that the electronic state of the $FeBr_4$ salt may be close to states in the high-pressure phases of κ-(BEDT-TTF)$_2$Cu(NCS)$_2$ and κ-(BETS)$_2$FeBr$_4$.

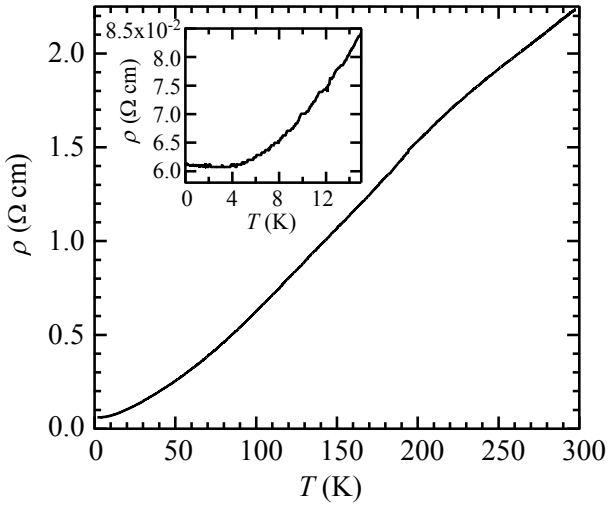

Figure 3.6: Temperature dependence of the interlayer resistivity for κ-(BDH-TTP)$_2$FeBr$_4$. Inset: Low temperature data (below 15 K).

The interlayer MR ratio at 30 mK is shown in Fig. 3.7. In Fig. 3.7(a), we note that the resistance for $H \parallel a$ ($\theta = 90°$) suddenly drops by 46 % at 2.0 T, corresponding to $H_{\rm SF}$. This steep change provides direct evidence of the strong π-d interaction. Above $H_{\rm SF}$, the resistance increases quadratically and then linearly with field, which for 2D systems is explained by the Boltzmann transport theory.[37] As the field is tilted from the a- to the b-axis, the sharp drop at $H_{\rm SF}$ is smeared out. For $H \parallel b$, the resistance gradually decreases as the field increases to 5 T. Figure 3.7(b) presents the MR for fields in the bc-plane. Below 5 T, all the curves show a gradual decrease with increasing field. This behavior corresponds to the gradual increase in the magnetization [M-H curves for $H \parallel b$ and c in Fig. 3.3(a)]. For 2D systems, the interlayer resistance is field independent in magnetic fields perpendicular to the layers.[37] This trend is present in the results for $H \parallel b$ with fields above 5 T ($\theta = 0°$).

Note also that the resistance slightly increases for $H \parallel a$ below $H_{\rm SF}$. For H aligned along the easy-axis, the AF ordered 3d spins fluctuate significantly by the increasing field. The fluctuating magnetic

potential leads to an additional scattering of π electrons as the field nears $H_{\rm SF}$. Such behavior has been observed in many dilute magnetic alloys.[79,80]

The resistances at 30 mK, 0.55 K, and 1 K for $H \parallel a$ are shown in Fig. 3.8. The resistance drop arising from the spin-flop transition at $H_{\rm SF}$ is smeared out slightly as temperature increases.

3.1.3 Magnetic torque

For measurements of the magnetic torque, the field is rotated in two rotation planes, the *ab*- and *cb*-planes. In this subsection, θ is defined as the field angle from the *a*- or *c*-axis to the *b*-axis. Note that the amplitudes of the magnetic torque curve are different between the positive and negative directions because of the structure of the cantilever.

The torque is generally given by $\tau = \mu_0(M \times H)$. For a paramagnetic state, we obtain $\tau = (1/2)(M_1 - M_2)\sin 2\theta$, where M_1 and M_2 are the magnetizations along the principal axes and θ is the field angle from the principal axis. Because paramagnetism for the π spins is negligible, the $3d$ spins are the dominant contributors to the torque.

The torque curve $\tau(H)$ at 1.2 K, shown in Fig. 3.9(c), exhibits a sharp peak at 1.7 T. The curve rapidly decreases above 1.7 T. This behavior is associated with change in sign for fields nearly parallel to the *a*-axis ($\theta \leq 30^\circ$). The peak field corresponds to the spin-flop transition field ($H_{\rm SF}$) [Fig. 3.3(a)]. As the direction of the field approaches the *b*-axis ($\theta = 80^\circ$), the peak is smeared and τ changes its sign at higher fields. All the $\tau(H)$ curves become field-independent above 6 T, indicating the saturation of M. At 4K, $\tau(H)$ changes monotonically, and no sign changes occur.

As shown in Fig. 3.9(a), the angular dependence of τ is given by a simple $\sin 2\theta$ curve below $H_{\rm SF}$, but exhibits complicated behavior above $H_{\rm SF}$. At fields above 4 T, the $\tau(H)$ curve tends to show a reversed $\sin 2\theta$ dependence.

For the *cb*-plane rotation of H, the $\tau(H)$ curves show no rapid change, but show the sign changes at 1.2 K[Fig. 3.10(c)]. At 4 K, the $\tau(H)$ and $\tau(\theta)$ curves for the *cb*-rotation are similar to those for the *ab*-rotation.

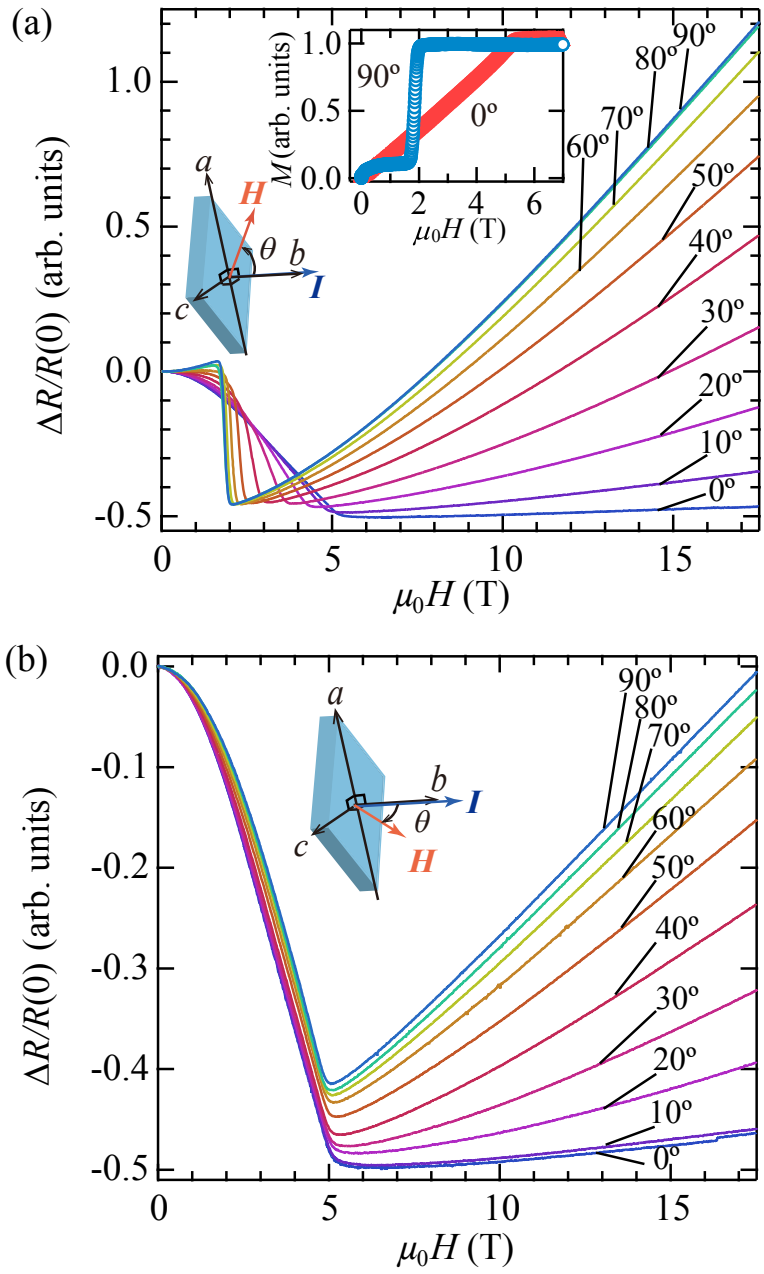

Figure 3.7: Interlayer MR ratio for κ-(BDH-TTP)$_2$FeBr$_4$ at 30 mK for fields in (a) the *ab*- and (b) *bc*-planes. Inset: Calculated M vs. H curves.

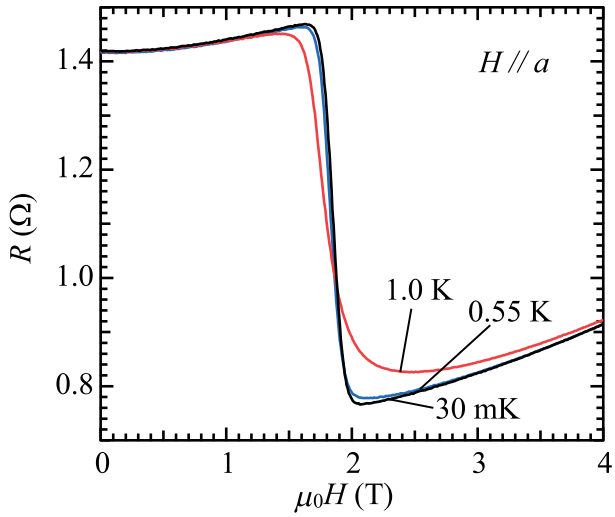

Figure 3.8: Interlayer resistance for κ-(BDH-TTP)$_2$FeBr$_4$ in the magnetic field along the a-axis at various indicated temperatures.

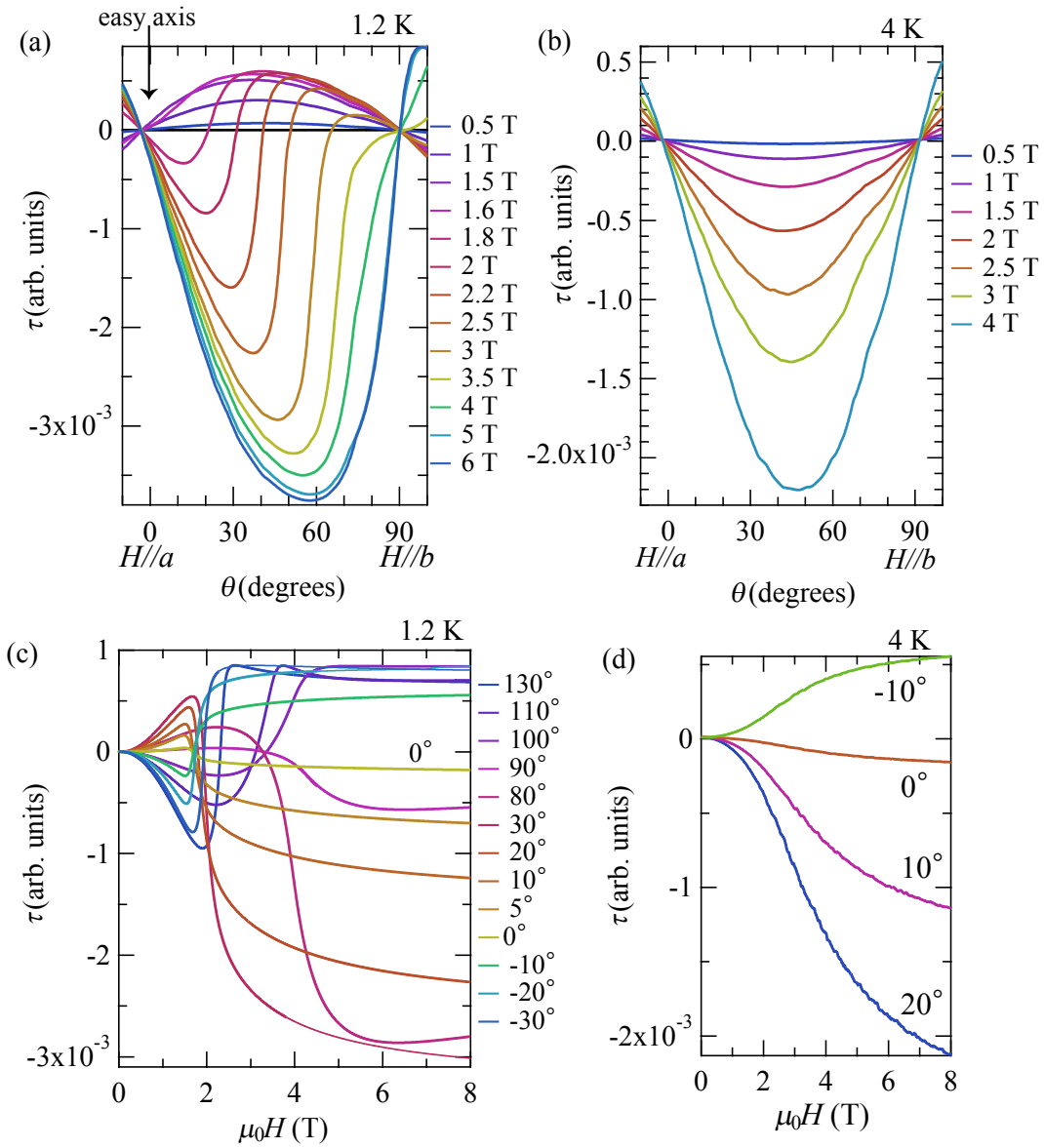

Figure 3.9: Field angle and field dependences of the magnetic torque for κ-(BDH-TTP)$_2$FeBr$_4$ at 1.2 K and 4 K. The magnetic fields are rotated in the *ab*-plane.

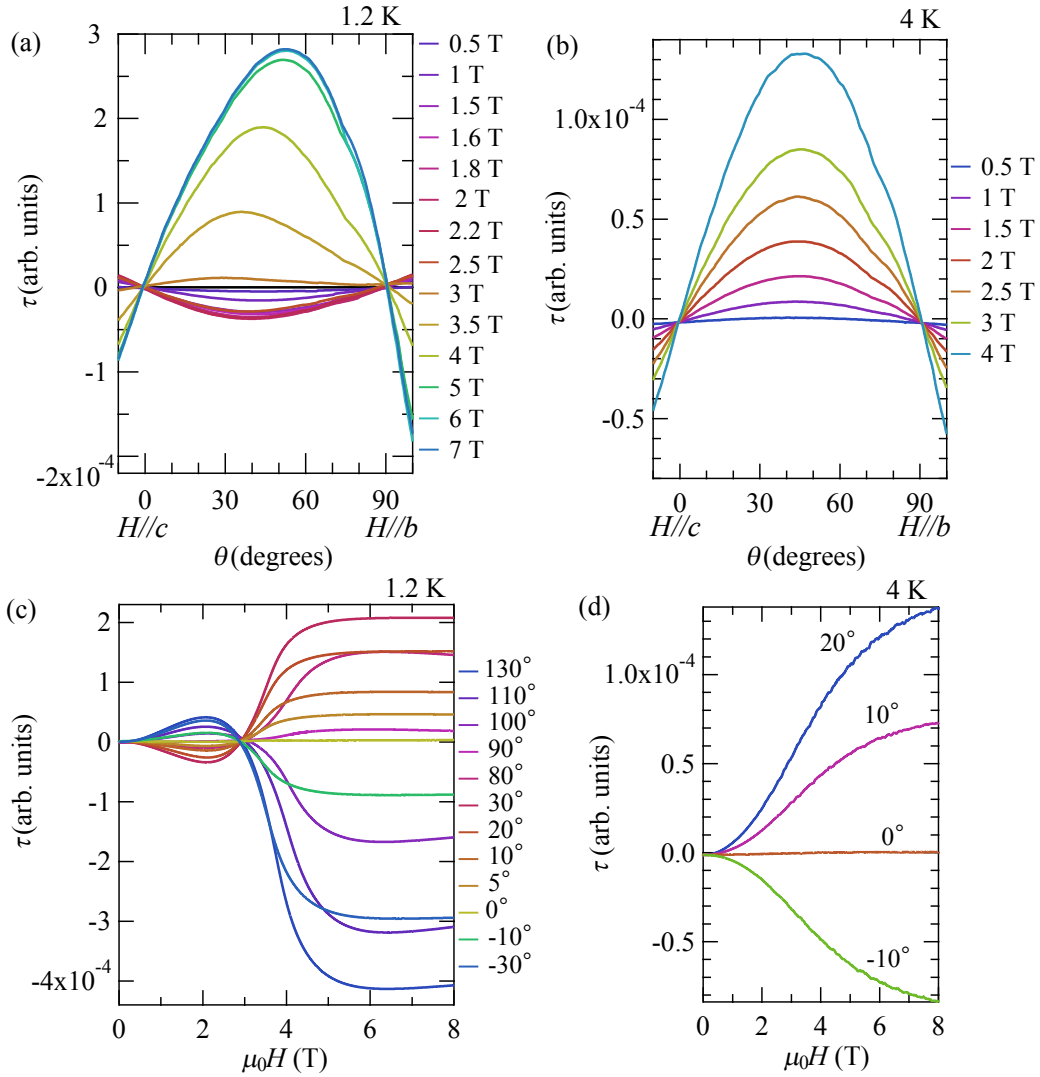

Figure 3.10: Field angle and field dependences of the magnetic torque for κ-(BDH-TTP)$_2$FeBr$_4$ at 1.2 K and 4 K. The magnetic fields are rotated in the *cb*-plane.

3.2 Discussion for κ-(BDH-TTP)$_2$FeBr$_4$

In the previous section, it was shown that the Fe 3d spin system is in the AF ordered state below 3.9 K, whereas the π electrons are in the metallic state down to 30 mK. Moreover, the Fe 3d spins exhibited characteristic magnetization curves, closely correlated with the MR behavior. Here, a few important key issues are discussed to understand these phenomena.

3.2.1 Magnetic anisotropy

In the AF state, the anisotropic magnetization is observed, which is associated with the coexistence of the spin-flop transition and spin canting. Interestingly, a large uniaxial anisotropy along the a-axis is observed in the magnetic susceptibility and also for the paramagnetic state (Fig. 3.1), where such anisotropy is in general absent. The susceptibility anisotropy is much larger than that expected from the g-values. Here we analyze the anisotropy in the paramagnetic state. The single-ion crystal field (CF) and dipole-dipole interaction is known to lead to anisotropy in the magnetic susceptibility.[81] The effects of the Dzyaloshinskii-Moriya (DM) and anisotropic exchange interactions can be excluded from the origin as these contributions are much smaller than the others, as we shall show later. The anisotropy energy of the single-ion CF effect up to the quadratic terms can be described as

$$E_{\rm anis} = DS^2 + E(S_x^2 + S_y^2). \tag{3.1}$$

This term gives anisotropic susceptibilities,

$$(\chi_\nu - \chi_\mu)_{\rm single-ion} = \frac{2Ng^2\mu_{\rm B}^2 S(S+1)(K_\nu - K_\mu)}{15(k_{\rm B}T)^2}, \tag{3.2}$$

where $K_x = -K_y = -E(2S-1)(2S+3)/4$ and $K_z = -D(2S-1)(2S+3)/4$. N denotes the number of the magnetic ions, and $(\nu, \mu) = (x, y, z)$. The z-axis is taken as the a-axis (easy axis). The effect from the dipole interaction is similarly described,

$$(\chi_\nu - \chi_\mu)_{\rm dipole} = \frac{2N\left[g^2\mu_{\rm B}^2 S(S+1)\right]^2(\psi_\nu - \psi_\mu)}{9(k_{\rm B}T)^2}, \tag{3.3}$$

where ψ_ν denotes the dipole sums $\psi_\nu = \sum_{j,\nu} r_{i,j}^{-3}\left(3x_{ij\mu}x_{ij\nu}r_{ij}^{-2} - \delta_{\mu\nu}\right)$. The sum of $(\chi_\nu - \chi_\mu)_{\rm single-ion}$ and $(\chi_\nu - \chi_\mu)_{\rm dipole}$ gives the total anisotropies of the susceptibilities $\Delta\chi_{\nu\mu} = \chi_\nu - \chi_\mu$. The curves for $\Delta\chi_{ab}$ and $\Delta\chi_{cb}$, plotted in Fig. 3.11 as a function of T^{-2}, show a linear dependence over a wide temperature range, demonstrating that the above model is appropriate. By fitting the data with this model (the solid lines in Fig. 3.11), we obtain parameters D = -0.38 K and E = 0.038 K using the calculated values for the Fe 3d spins, $\psi_a - \psi_b = 3.95 \times 10^{22}$ cm^{-3} and $\psi_c - \psi_b = 1.59 \times 10^{22}$ cm^{-3}. The negative value of D is consistent with the magnetic easy axis along the a-axis (z-axis) and the result $|D| \gg E$ shows that the CF has a nearly uniaxial symmetry.

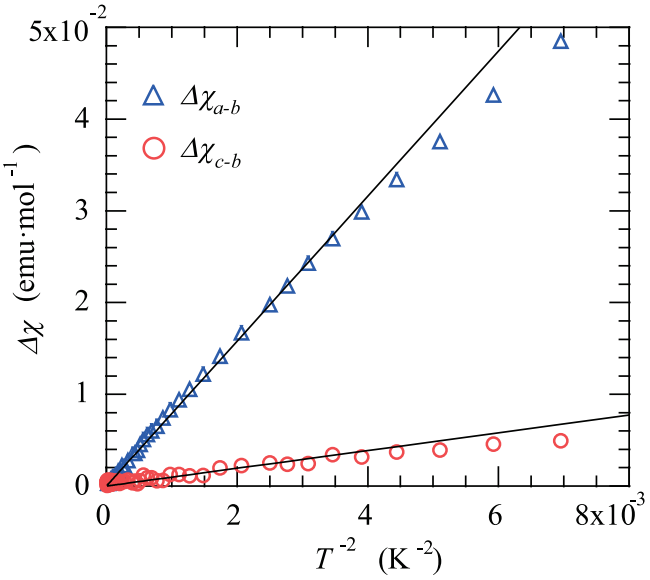

Figure 3.11: Plot of the anisotropies of the susceptibilities vs. T^{-2} in the paramagnetic region for κ-(BDH-TTP)$_2$FeBr$_4$. Solid lines are the fitted results above 18 K. See text for details.

3.2.2 Magnetic structure and spin canting in AF ordered state

The T_N values calculated using the mean field approximation are in good quantitative agreement with the experimental data, $T_N = 3.9$ K for the FeBr$_4$ salt and $T_N < 1.5$ K for the FeCl$_4$ salt. The small jumps in the magnetization for $H \parallel b$ and $H \parallel c$ seen in Fig. 3.3(a) indicate that the $3d$ spins in the AF state are canted from the easy axis (a-axis). There are three possible mechanisms for the canted configuration of the AF spin state: 1) spin frustration effect,[82] 2) ligand-field difference between the two independent FeBr$_4$ anions,[83,84] and 3) the DM interaction.[85,86] Each of the three possible mechanisms are discussed next.

1) Figure 3.12 shows a schematic of the spin structure for the FeBr$_4$ salt stemming from the coexisting Fe $3d$ and π spins. The κ-type salts to which the present FeBr$_4$ salt belongs [see Fig. 1.19(b)], are modeled as a highly frustrated triangular π spin systems with the donor dimer as the fundamental unit (π_1 and π_2) because all of the nearest neighbor exchange interactions are AF.[54,87] The exchange interactions between the dimers are given by $2t^2/U$, where t and U are the overlap integral and the on-site Coulomb interaction, respectively. In the triangular lattice of the BDH-TTP dimers [Fig. 1.19(b)], the ratio of the two exchange interactions J'/J $[= (t'/t)^2]$ is estimated from $t' = (p^2 + q^2)^{1/2}$ and $t = c2$ to be 0.22 . This J'/J ratio is not close to unity (fully frustrated case), but it causes some frustration for the AF order of the Fe $3d$ spins via $J_{\pi d}$, because the Fe d_1 spin is frustrated aided by the two major AF interactions, J_4 and J_6, with the dimer spins, π_1 and π_2, respectively [Fig. 3.12(a)]. It is difficult to estimate the effect of the π spin frustration on the $3d$ AF order, but it is a possible reason for the canted-spin structure.

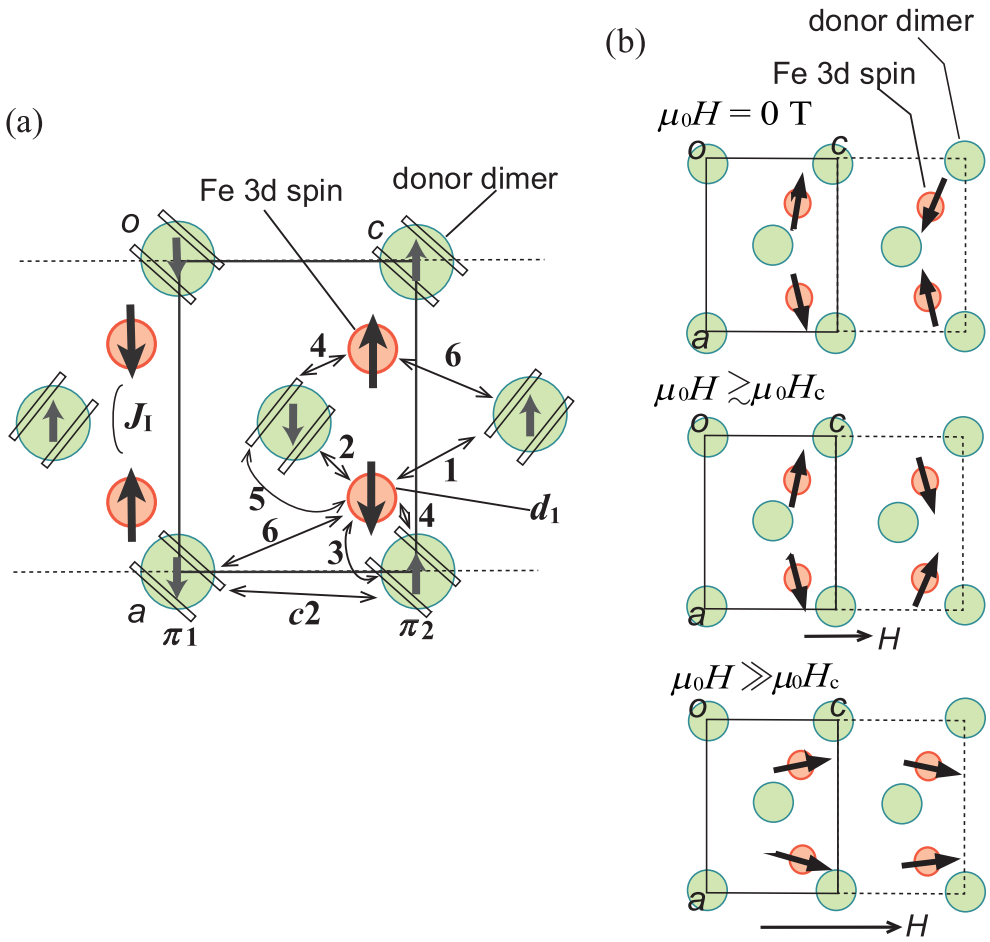

Figure 3.12: (a) Possible spin structures and definition of the six π-d interactions (J_1-J_6). (b) Possible 3d spin structures for $H \parallel c$.

2) The two independent tetrahedral $FeBr_4^-$ ions are alternately inclined from the a-axis in the ac-plane by about 11°. This alternating inclinations cause some spin canting in the ac-plane. However, this effect cannot explain the spin canting in the ab-plane (magnetization jump for $H \parallel b$) because of the mirror symmetry (parallel to the ac-plane) of the structure.

3) The DM interaction is generally written as $D_{\mathrm{DM}}(S_i \times S_j)$, which can lead to a spin-canting. The structure of the neighboring Fe ions has no inversion symmetry, giving a non-zero D_{DM} vector. The mirror symmetry parallel to the ac-plane suggests that a D_{DM} vector possibly exists along the b-axis, causing a spin canting in the ac-plane. The amplitude of the D_{DM} vector is estimated as $|D_{\mathrm{DM}}| \propto (\Delta g/g) J_{\mathrm{I}} \sim 0.046 \times 0.31 \sim 0.015$ K, where Δg is the deviation from the free electron g-value. Because the DM interaction is much smaller than J_{I} and the anisotropy parameter D, the DM interaction will not be the dominant mechanism of the spin canting.

Based on the above discussion, possible canted-spin structures are proposed in Fig. 3.12(b). At zero field, all the d spins are slightly canted from the easy axis (a-axis). Note that the total moment vanishes in this configuration. For $H \parallel c$ slightly above H_c, there is a rearrangement in the canted-spin configuration, associated with the small jumps of the magnetization. In this field range, the 3d spins

have a WF character. The average change in angle of the canted spins may be several degrees, causing a magnetization jump of about 0.35 μ_{B}. At higher fields, all the spins are almost aligned along the c-axis; the total moment is saturated. This magnetization process is consistent with the M-H curves in Fig. 3.3(a). A similar process will occur also for $H \parallel b$.

3.2.3 ESR linewidth and critical phenomena

The deviation in the susceptibility from the Curie-Weiss behavior above $T_{\rm N}$ (Fig. 3.2) is suggestive of the development of spin fluctuations originating from the low-dimensionality. The broadening of the ESR signal is also an important signature of a developing short-range order, which typically appears in low dimensional antiferromagnets.

In general, the ESR linewidth can be expressed in terms of the following function $\sum_k |F_k|^2 \langle S^z_k(\tau) S^z_{-k}(0)\rangle^2$, where the dynamic contribution $\langle S^z_k(\tau) S^z_{-k}(0)\rangle$ representing the spin fluctuations is the correlation function of S^z_k,which is governed by the isotropic exchange interaction.[88–90] The static contribution $|F_k|$ is the k-component of the Fourier transform for the second moment from all the interactions that do not conserve the total spin, such as the dipole-dipole interaction, CF effect, DM interaction, anisotropic exchange interaction, and hyperfine interaction.

In the high temperature regime above 120 K, the lineshape is Lorentzian, indicating the strong exchange narrowing. In this case, the spin correlation function has a strong exponential decay, for which the correlation time is characterized by the exchange frequency $\hbar\omega_{\rm ex} = 2z\sqrt{S(S+1)}J$. The ESR peak-to-peak linewidth $\Delta H_{\rm pp}$ is given by the second moment M_2 and exchange frequency $\omega_{\rm ex}$,

$$\Delta H_{\rm pp} = \frac{20}{3}\frac{\hbar M_2}{g\mu_{\rm B}\omega_{\rm ex}} \tag{3.4}$$

assuming a cubic symmetry, and $M_2 = \langle[\mathcal{H}_{\rm int}, S_+][\mathcal{H}_{\rm int}, S_-]\rangle / \langle[S_-, S_+]\rangle$ where $\mathcal{H}_{\rm int}$ includes all interactions contributing to the linewidth.

For the dipole-dipole interaction between the d spins, $M_2^{\rm Dipole}$ is given by

$$M_2^{\rm Dipole} = [3/(4\hbar^2)]S(S+1)g^4\mu_B^4 \sum_{ij} \left(3\cos^2\theta_{ij} - 1\right)^2 r_{ij}^{-6}, \tag{3.5}$$

where r_{ij} is the distance between the ith and jth $3d$ spins and θ_{ij} is the angle between the $\boldsymbol{r_{ij}}$ vector and the field. The maximum linewidth is estimated as $\Delta H_{\rm pp}^{\rm dipole} = 1.1$ mT for $H \parallel a$, taking $z = 2$, $g = 2$, and $J \sim J_{\pi d} = 8.32$ K (Table 1.3). The linewidth arising from the dipole interaction between the π and d spins has a smaller contribution. Accordingly, the dipole-dipole interaction cannot solely explain the linewidth in Fig. 3.5(a). The second moment arising from an axial CF effect is given by

$$M_2^{\rm CF} = (1/10)D^2(2S-1)(2S+3)(1+\cos^2\theta), \tag{3.6}$$

where θ is the angle of magnetic field from the principle axis of the CF ($\parallel a$).[91] Taking $|D| = 0.38$ K and $J \sim J_{\pi d}$, we obtain a maximum linewidth of $\Delta H_{\rm pp}^{\rm CF} = 15$ mT for $H \parallel a$. The second moment for the DM interaction is given by

$$M_2^{\rm DM} = (2/3)D_{\rm DM}^2 S(S+1)(1+\cos^2\theta), \tag{3.7}$$

where θ is the angle of magnetic field from the principle axis of the $D_{\rm DM}$ vector.[92,93] As $D_{\rm DM} \sim (\Delta g/g)J_d$, $\Delta H_{\rm pp}^{\rm DM}$ is much smaller than $\Delta H_{\rm pp}^{\rm CF}$. Similarly, the linewidths arising from the anisotropic

exchange interaction, $\sim (\Delta g/g)^2 J$, and the hyperfine interaction are also negligible. In this way, we infer that the major contribution to the linewidth is from the CF effect. The estimated values are comparable to the experimental data at high temperatures [Fig. 3.4(a)]. The estimations are also consistent with the result that the linewidth is highest for $H \parallel a$ at temperatures above 180 K [Fig. 3.4(a)].

As the temperature approaches $T_{\rm N}$, the spin fluctuations related to the q-vector defining the AF ordered state grows. This process takes place over a wide temperature range as the short-range magnetic order develops, especially for low-dimensional antiferromagnets.[88–90] In the ESR spectra, this process is observed as a successive increase in the linewidth near $T_{\rm N}$. This is what we observed in the linewidth in the critical region.

Here we note that the linewidth broadening is pronounced in the field directions parallel to the b- and c-axes [Fig. 3.4(a)], which are the direction of the spin canting. Therefore, it is concluded that the fluctuations related to the spin canting are significantly pronounced in the critical region.

Broadening occurs because the correlation function $\langle S_k^z(\tau) S_{-k}^z(0)\rangle$ does not decay fast enough to guarantee convergence of the time integral of the correlation function.[91,92] This will lead to a broader lineshape than the Lorentzian shape. At present, it is not clear whether the lineshape deviates from a Lorentzian shape at low temperatures.

3.2.4 Magnetic potential effect on the MR

In the $FeBr_4$ salt, the presence of the MR decrease below $T_{\rm N}$ (Fig. 3.7) is evidence of the interplay between the electron transport of π electron carriers and magnetism of the Fe d electron spins. Characteristic negative MRs have been reported in some π-d systems.[21,52,94,95] For example, β-(EDT-DSDTFVSDS)$_2$$FeBr_4$ exhibits semiconducting behavior below 30 K, and a negative MR is observed at low temperatures.[94] For the AF superconductor κ-(BETS)$_2$$FeBr_4$ with $T_{\rm c} = 1$ K and $T_{\rm N} = 2.5$ K, the resistance decreases with increasing field after the superconductivity and then the AF phase are broken.[95] These features have been explained in terms of the magnetic potential effects via the π-d interactions $J_{\pi-d}$.

A schematic of the magnetic potential effect on the π spin transport is presented in Fig. 3.13. In the $FeBr_4$ salt, the 3d spins have the AF order (Fig. 1.20). The π spins see the magnetic potential produced by the Fe 3d spins via the interaction $J_{\pi d} s \cdot S$. When the π spins pass through the layers in the AF state, the magnetic potential alternately changes its sign, depending on the direction of the Fe 3d spin polarization [Fig. 3.13(a)]. This effectively reduces the interlayer transfer integral; the interlayer resistance of the π spins then increases. When all the Fe 3d spins are aligned by fields, the π spins see the homogeneous magnetic potential, which then decreases the resistance [Fig. 3.13(b)].

Figure 3.14 is a schematic of the d spin alignment and the MR behavior. For $H \parallel a$ (easy axis), the 3d spins rapidly align at $H_{\rm SF}$, giving a steep decrease in resistance. For $H \parallel c$ the Fe 3d spins gradually align along the field (the magnetization smoothly increases with field), giving a moderate

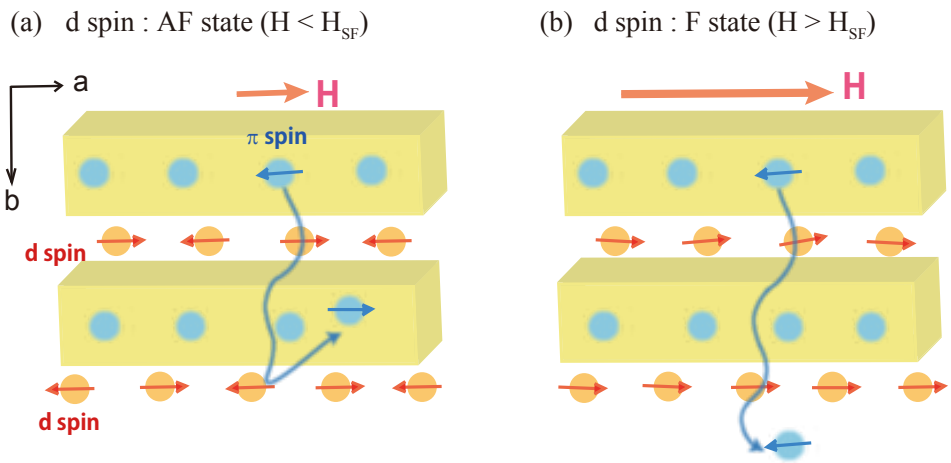

Figure 3.13: Schematic of magnetic potential effect on the π electron transport for (a) $H < H_{\mathrm{SF}}$ and (b) $H > H_{\mathrm{SF}}$ when the field is applied parallel to the a-axis (easy axis).

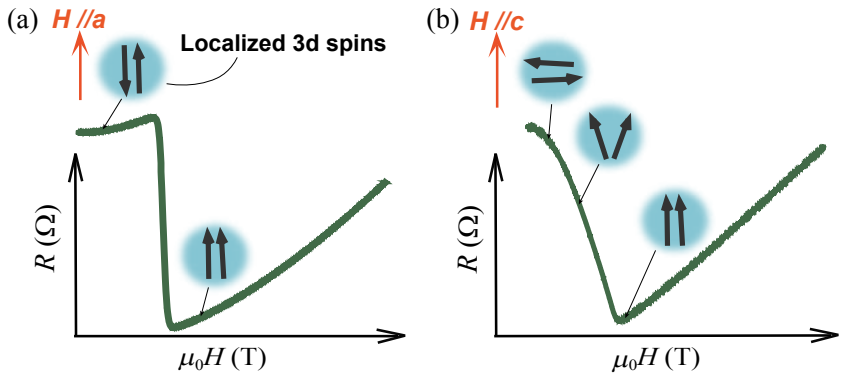

Figure 3.14: Schematic of d spins and MR behavior for (a) $H \parallel a$ and (b) $H \parallel c$. The black arrows indicate the $3d$ spins.

decrease in resistance. After the Fe $3d$ spins are aligned, the resistance is predominantly determined by the orbital effect that depends on the field direction.[37] This magnetic potential effect arises from the Zeeman effect. Therefore, the change in resistance should be independent of the field direction. As seen in Fig. 3.7, the decrease in resistance is actually almost independent of the field direction (46∼50 % for H in the ab-plane and 42∼50 % for H in the cb-plane.), which is consistent with the above picture. At T_{N} in zero magnetic field, no anomaly in the resistance is observed (Fig. 3.6) in contrast to κ-$(\mathrm{BETS})_2\mathrm{FeBr}_4$. The reason is that the $3d$ spins strongly fluctuate over a wide temperature range near T_{N} which smears out the resistance anomaly.

Next, we semiquantitatively discuss the magnetic potential effect on the field dependence of the MR in an analogy with the tunneling MR model.[96,97] The simple model proposed is that the interlayer transport is described by a quantum tunneling process. The tunnel conductance G is generally given by $G = e^2|T|^2/h$, where $|T|$ is the transmission coefficient. If we assume that a π electron with a spin only antiparallel to the $3d$ spins can tunnel through the FeBr_4 layer, the spin dependent transmission coefficient of the electron tunneling through the next FeBr_4 layer will be given by $|T| \propto \cos\delta$, where

δ is the angle between the $3d$ spins of the neighboring layers. Because the total magnetization in field is $M(H) = M_0\cos(\delta/2)$ (M_0: saturated magnetization), we obtain the spin dependent tunnel conductance $G_{\rm spin} \propto [M(H)/M_0]^2$, which gives a negative MR

$$\frac{R(H)}{R(0)} = \frac{1}{1+\alpha R(0)(M(H)/M_0)^2}, \tag{3.8}$$

where $R(0)/[1+\alpha R(0)]$ is the resistance in the high field limit. A similar relation in the MR is also given for dilute magnetic alloys, where the s-d interaction is crucial,[80] and for ferromagnetic materials.[98]

To simulate the MR in detail, it is necessary to develop a more suitable model. However, the above simple model is helpful for a qualitative understanding of the spin-dependent tunneling. We present the $M(H)/M_0$ curves from the $\Delta R(H)/R(0)$ data for $H \parallel a$ and b, from which the quadratic background is subtracted, in the inset of Fig. 3.7(a). The $M(H)/M_0$ curve for $H \parallel a$ has a rapid increase at 2.0 T, whereas it gradually increases to 5 T for $H \parallel b$. These results are roughly consistent with the $M(H)$ curves at 2 K in Fig. 3.3(a).

3.3 Results for κ-(BDH-TTP)$_2$FeCl$_4$

3.3.1 Magnetic properties

The temperature dependences of the magnetic susceptibility χ and the inverse of χ were measured along each crystallographic axis at 0.5 T, and are shown in Fig. 3.15(a). The χ^{-1} plots show a linear dependence on temperature that follow the Curie-Weiss law with a small Weiss temperature $\Theta \approx -0.2$ K. The χT values [Fig. 3.15(b)] are almost constant above 50 K and the Curie constant of $C = 4.4$ emu·K·mol^{-1} is evidence for the high spin state ($S = 5/2$) of the Fe(III) ion. Here, we should note that the Pauli paramagnetism of the π spins is negligible. At lower temperatures, χT shows a characteristic temperature dependence [inset of Fig. 3.15(b)], the origin of which will be discussed later.

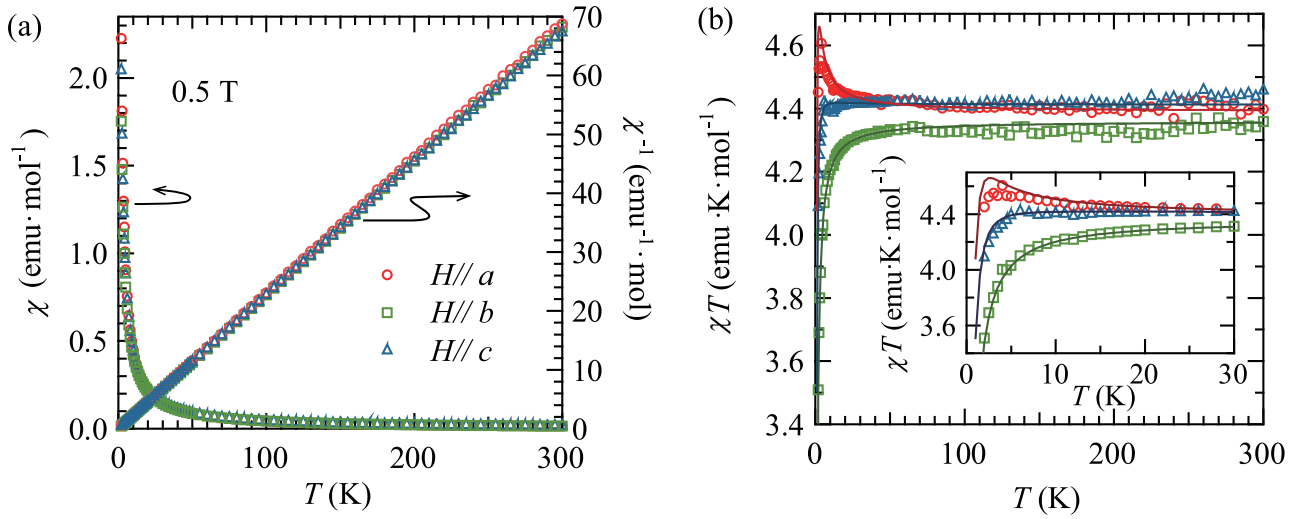

Figure 3.15: (a) Temperature dependence of the magnetic susceptibility for κ-(BDH-TTP)$_2$FeCl$_4$ along each crystal axis at $H = 0.5$ T. (b) χT vs T plots. Inset: Low-temperature data below 30 K. The solid curves represent the simulation results obtained using $D = -0.1$ K and $E = 0.042$ K.

The plots of magnetization (M) vs. H at 2 K for different field directions are shown in Fig. 3.16. All the M-H curves approximately follow the Brillouin function and show no indications of a magnetic transition.

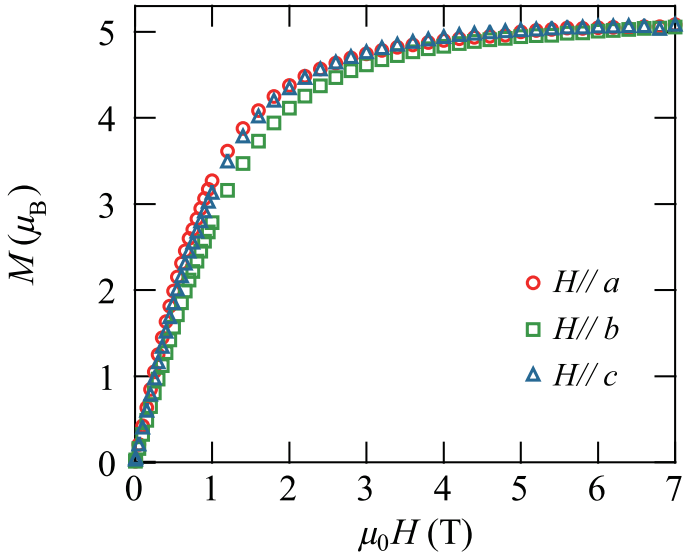

Figure 3.16: Magnetization vs. magnetic field measured at 2 K for κ-(BDH-TTP)$_2$FeCl$_4$.

In the ESR measurements, a single Lorentzian signal is observed in the entire temperature range. Because of the small π spin ($S = 1/2$), the ESR signal arises predominantly from the $3d$ spins ($S = 5/2$). The temperature dependences of the peak-to-peak linewidth ($\Delta H_{\rm pp}$), the g-value, and the inverse of the spin susceptibility ($\chi_{\rm spin}^{-1}$) are shown in Figs. 3.17(a)-(c), respectively. We see that the linewidths show peculiar temperature dependences. For $H \parallel a$, the linewidth gradually increases with decreasing temperature down to 3.5 K, but a cusp is seen at 130 K. For $H \parallel c$, a broad hump is observed at 130 K, whereas such an anomaly is ambiguous for $H \parallel b$. The g-values are almost constant above 50 K, but show steep changes at low temperatures below 50 K, the origin of which will also be discussed later. The $\chi_{\rm spin}^{-1}$ plots are approximately linear with temperature, consistent with the χ^{-1} plots shown in Fig. 3.15(a). For $H \parallel c$, the $\chi_{\rm spin}^{-1}$ plot has a broad cusp at 130 K, corresponding to the hump in the linewidth plots. However, the origin of the anomaly is unclear at present.

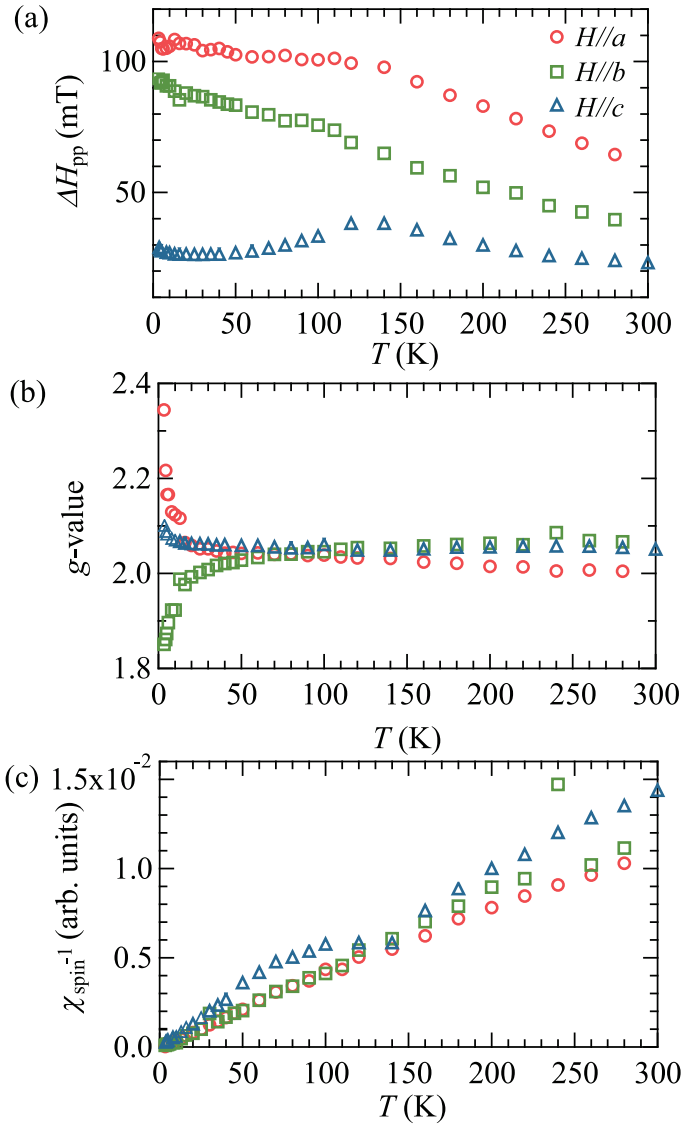

Figure 3.17: Temperature dependences of the (a) ESR linewidth $\Delta H_{\rm pp}$, (b) g-value, and (c) inverse of the spin susceptibility.

The angular dependences of the linewidth and g-value at 200 and 3 K are shown in Fig. 3.18.

A double-minimum dependence of the linewidth is clearly seen for H in the ab-plane but is not so evident for H in the bc-plane. The g-values have a sinusoidal dependence at 3 K for H in both the ab- and bc-planes but are almost constant at 200 K. The angular dependences of the g-values at 3 K are well fitted with $g(\theta) = g_1 \cos^2\theta + g_2 \sin^2\theta$ [solid curves in Fig. 3.18(c) and (d)], showing that the principal axes correspond to the crystal axes.

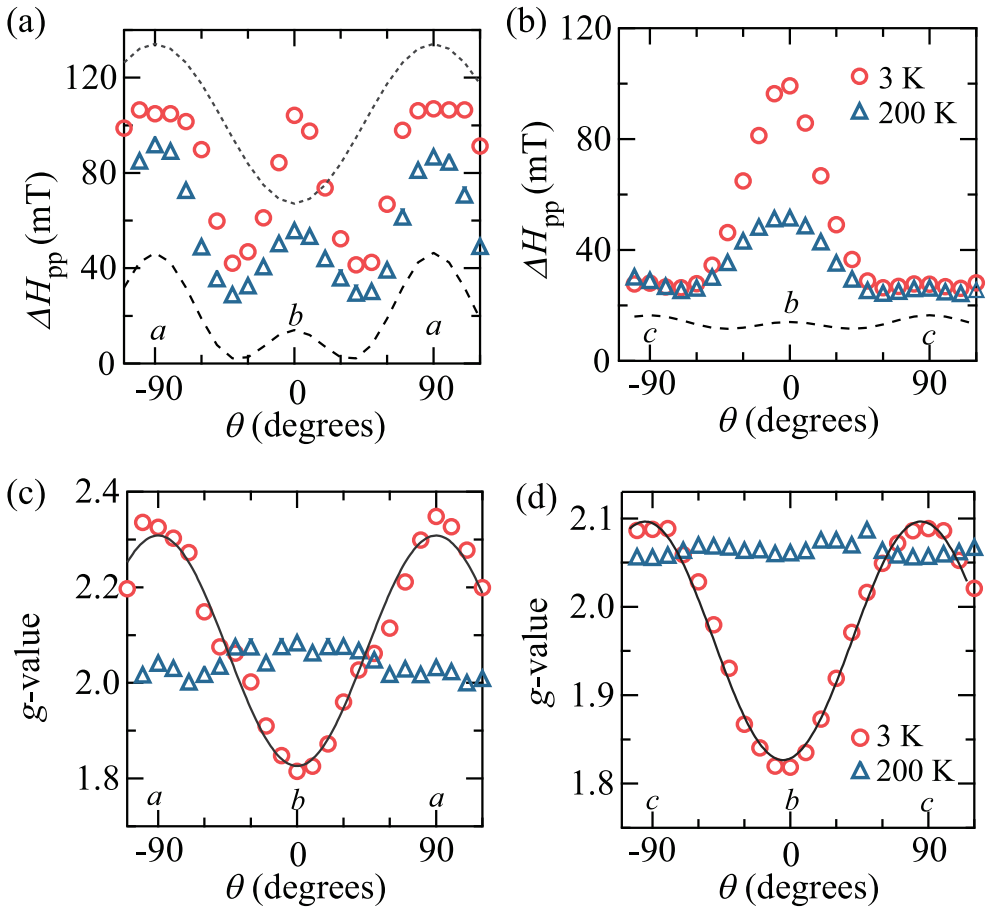

Figure 3.18: Angular dependences of the ESR linewidth ΔH_{pp} at 200 and 3 K for H in the (a) ab- and (b) bc-planes. Dotted and dashed curves denote the simulation results for the anisotropic crystal field and the dipole-dipole interaction effects, respectively. Angular dependences of the ESR g-value at 200 and 3 K for H in the (c) ab- and (d) bc-planes. Solid curves are the fitted curves using $g(\theta) = g_1 \cos^2\theta + g_2 \sin^2\theta$. The fitted values in (c) are $g_1 = 1.8$ and $g_2 = 2.3$, whereas those in (d) are $g_1 = 1.8$ and $g_2 = 2.1$.

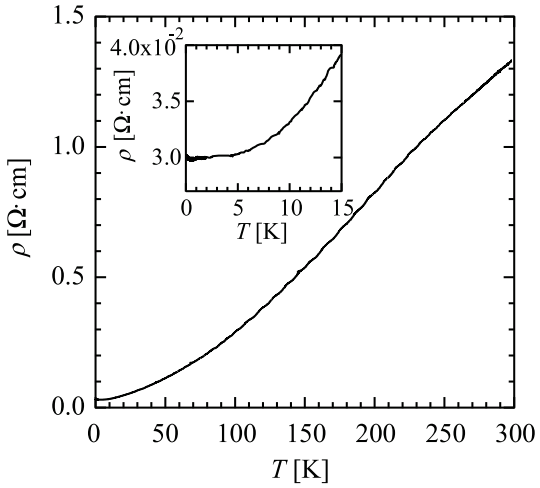

Figure 3.19: Temperature dependence of the resistivity. Inset: Low-temperature data below 15 K.

3.3.2 Resistivity and MR

The resistivity shows a monotonic decrease with decreasing temperature to 30 mK, as shown in Fig. 3.19, and no sign of superconductivity is seen. The monotonic temperature dependence is similar to that observed in the $FeBr_4$ salt.

Figure 3.20 shows the normalized MR data, ρ/ρ_0 curves at 30 mK, where ρ_0 is the resistance at zero field. The MR for $H \parallel a$ [$\theta = 90°$, Fig. 3.20(a)] exhibits an abrupt drop by about 20% at 0.2 T and then increases with increasing field. As the field is tilted from the a-axis to the b-axis, the MR drop becomes more moderate [inset of Fig. 3.20(a)] and, simultaneously, the positive MR at high fields is suppressed. For H in the bc-plane, the MR drops at low fields have no noticeable dependence on the field angle [Fig. 3.20(b)]. However, the increase in the positive MR at high fields becomes large as the field is tilted from the b-axis to the c-axis. Such an abrupt drop in the MR at low fields has also been observed in the $FeBr_4$ salt, which can be interpreted as the suppression of the magnetic potential by the spin-flop transition of the Fe $3d$ spins.[80] The evidence for a spin-flop transition for the $FeCl_4$ salt will be given below. The positive MR at high fields is explained by the orbital effect in 2D systems.[37] Figure 3.21 shows the normalized MR for $H \parallel a$ at various temperatures, in which the drop in the MR at 0.2 T is reduced as temperature increases above 0.4 K.

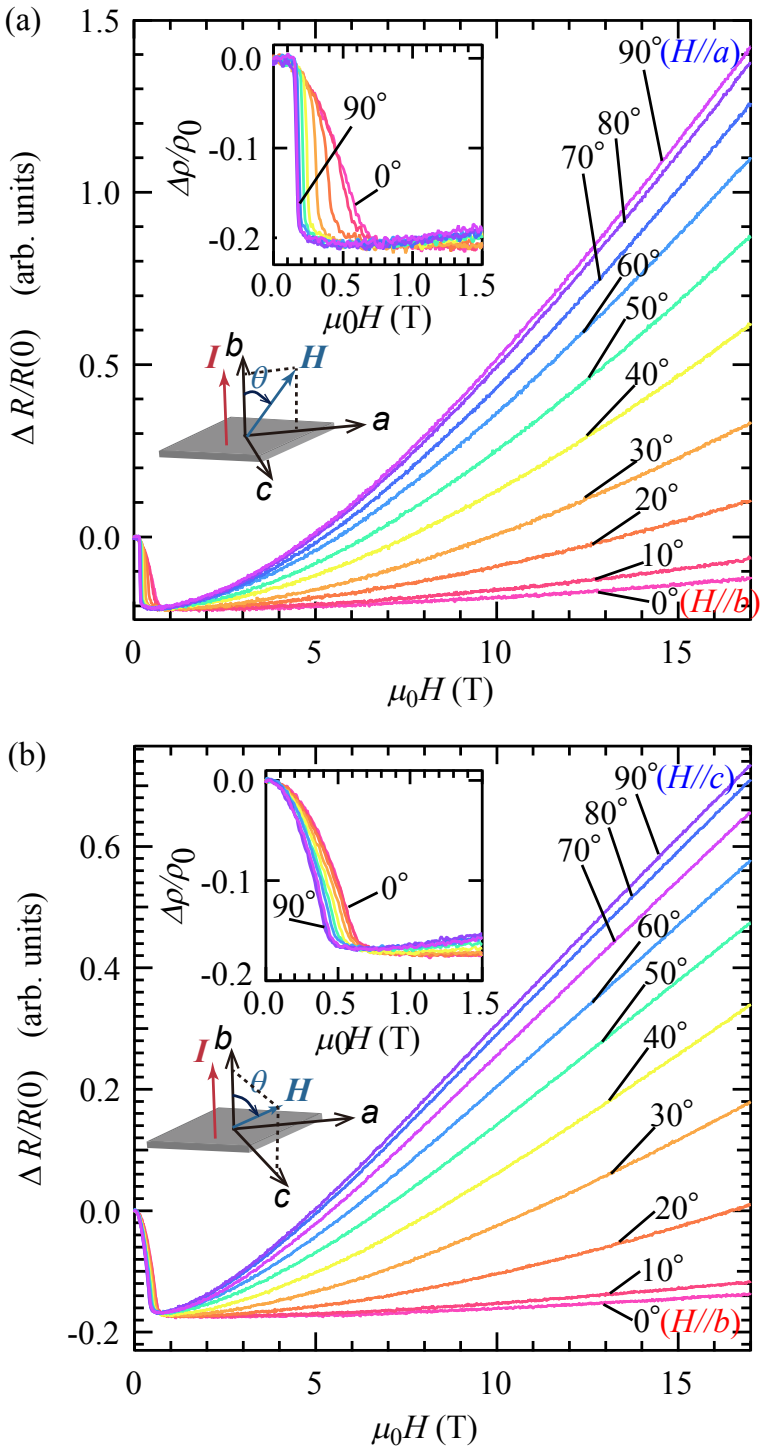

Figure 3.20: Normalized MR at 30 mK for H in the (a) *ab*- and (b) *bc*-planes. Insets: Close-ups of the low-field data below 1.5 T.

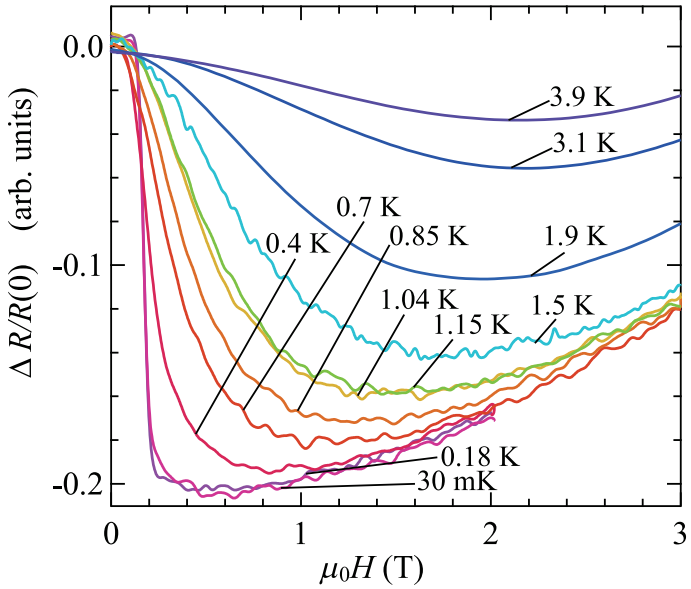

Figure 3.21: Normalized MR at various temperatures for $H \parallel a$.

3.3.3 Magnetic torque

In this subsection, θ is defined as the field angle from the a- or c-axis to the b-axis. The field dependences of the magnetic torque for a range of field angles in the ab-plane are shown in Figs. 3.22(c) and (d). The $\tau(H)$ curves (not shown) are almost linear above 4 T below 1 K, irrespective of the field direction. The result indicates that the magnetization is fully polarized above 4 T ($M \sim$ const.). The angular dependence is given by the simple sine curve at high fields, which has zeros at $\theta = 0^\circ$ and 90° for H in the ab- and bc-planes. Therefore, the principle axes of the magnetization correspond to the crystal axes, consistent with the results of the ESR measurements.

The torque curves at low fields show peculiar field dependences that are associated with the sign change. When the field is nearly parallel to the a-axis ($\theta \approx -1^\circ$), the sign change is observed at the lowest field of ~ 0.15 T, and then a kink occurs at ~ 0.25 T [red and black arrows in right panel of Fig. 3.22(c)]. The sudden sign change in the torque is caused by a rapid rearrangement of the spin structure. Similar sign changes have previously been observed in λ-$(BETS)_2FeCl_4$, κ-$(BETS)_2FeBr_4$, and the $FeBr_4$ salt [Fig. 3.9(c)], which are ascribed to spin-flop transitions.[64,66] Thus, we infer that the easy axis of the $3d$ spins is the a-axis and the spin-flop or metamagnetic transition takes place at around 0.15 T. At this magnetic transition, a steep decrease in the MR is seen [Fig. 3.20(a)], which provides clear evidence of a finite π-d interaction. The kink at 0.25 T in Fig. 3.22(c) is ascribed to a transition from the AF phase to the paramagnetic phase. The spin-flop transition field is much smaller than that (~ 1.5 T) for the $FeBr_4$ salt. As the field is tilted from the a-axis to the b-axis, the torque changes sign at higher fields. This tendency is closely related to the behavior of the steep MR decrease shown in Fig. 3.20(a), to be discussed later. When the field is nearly parallel to the b-axis, we see whether a dip or peak at ~ 0.7 T [Fig. 3.22(d)], which is also caused by the transition to a paramagnetic phase.

Figure 3.22(a) shows the $\tau(\theta)$ curves for the $FeCl_4$ salt at 30 mK, which are qualitatively very similar to those of the $FeBr_4$ salt. The $\tau(\theta)$ curves show a rapid change [Fig. 3.22(a)], which is strongly field-dependent. These changes are ascribed to the magnetic transition. At 1.5 K, the $\tau(\theta)$ curves are simple $\sin 2\theta$ curves, similar to those of the $FeBr_4$ salt above T_N.

For the H rotation in the cb-planes, the $\tau(\theta)$ and $\tau(H)$ curves at 30 mK are shown in Fig. 3.23. At 30 mK, $\tau(H)$ changes monotonically up to 0.5 T, and becomes linear with field above 0.5 T. The behavior indicates that the magnetization saturates above 0.5 T . The $\tau(\theta)$ curves at 30 mK and 1.5 K show a $\sin 2\theta$ dependence, which differs from the data for H in the ab-plane. The results are consistent with the picture of the AF order with the easy axis along the a-axis.

The torque curves for $\theta = 173^\circ$ at various temperatures are shown in Fig. 3.24. A sudden sign change induced by the spin-flop transition occurs at 0.15 T at a low temperature. As the temperature increases, the change at 0.15 T is smeared and is completely suppressed above 0.5 K. The results show that for the AF order T_N is approximately 0.4 K.

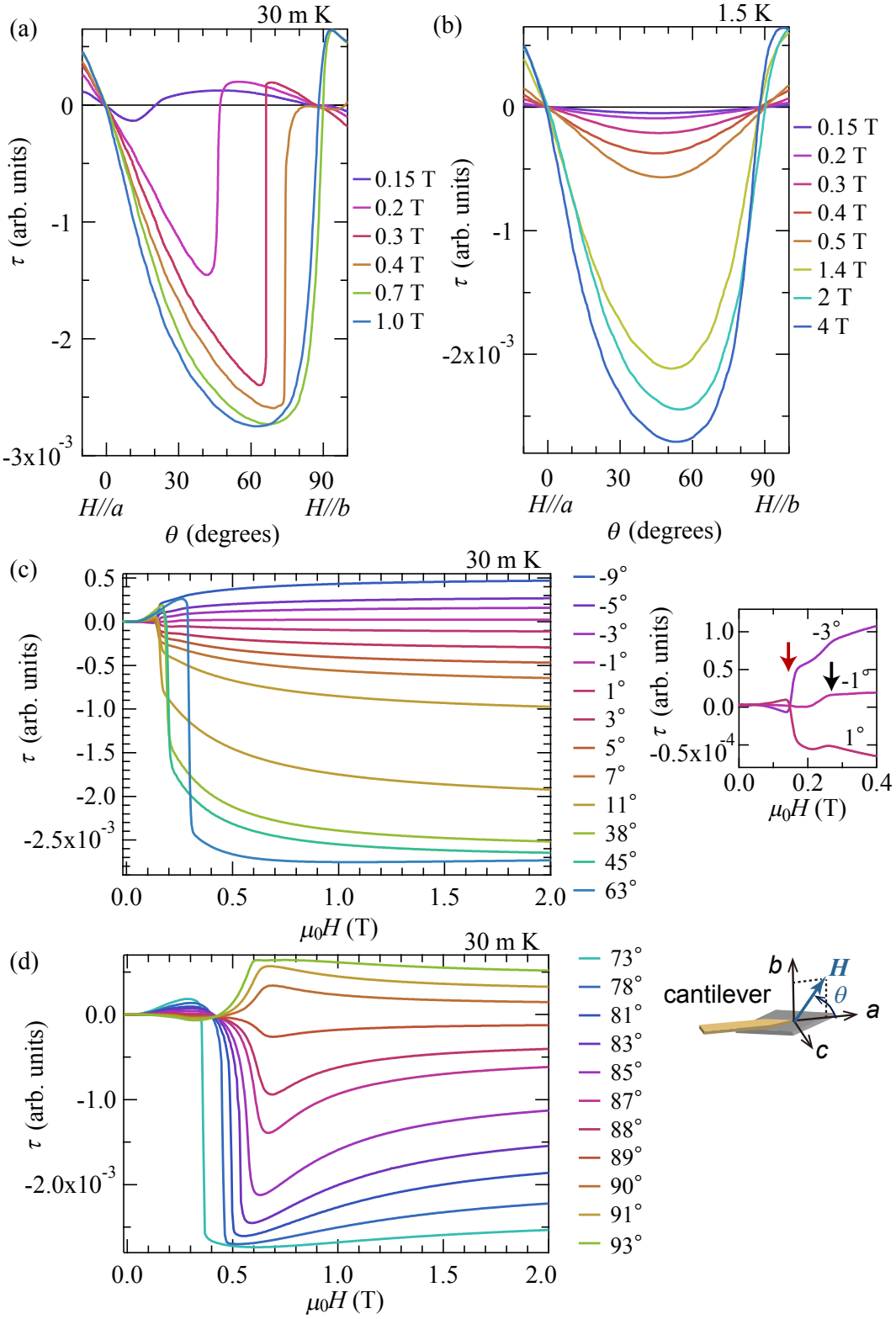

Figure 3.22: Field angle and magnetic field plots of magnetic torque for κ-(BDH-TTP)$_2$FeCl$_4$. Magnetic fields are rotated in the *ab*-plane at 30 mK and 1.2 K.

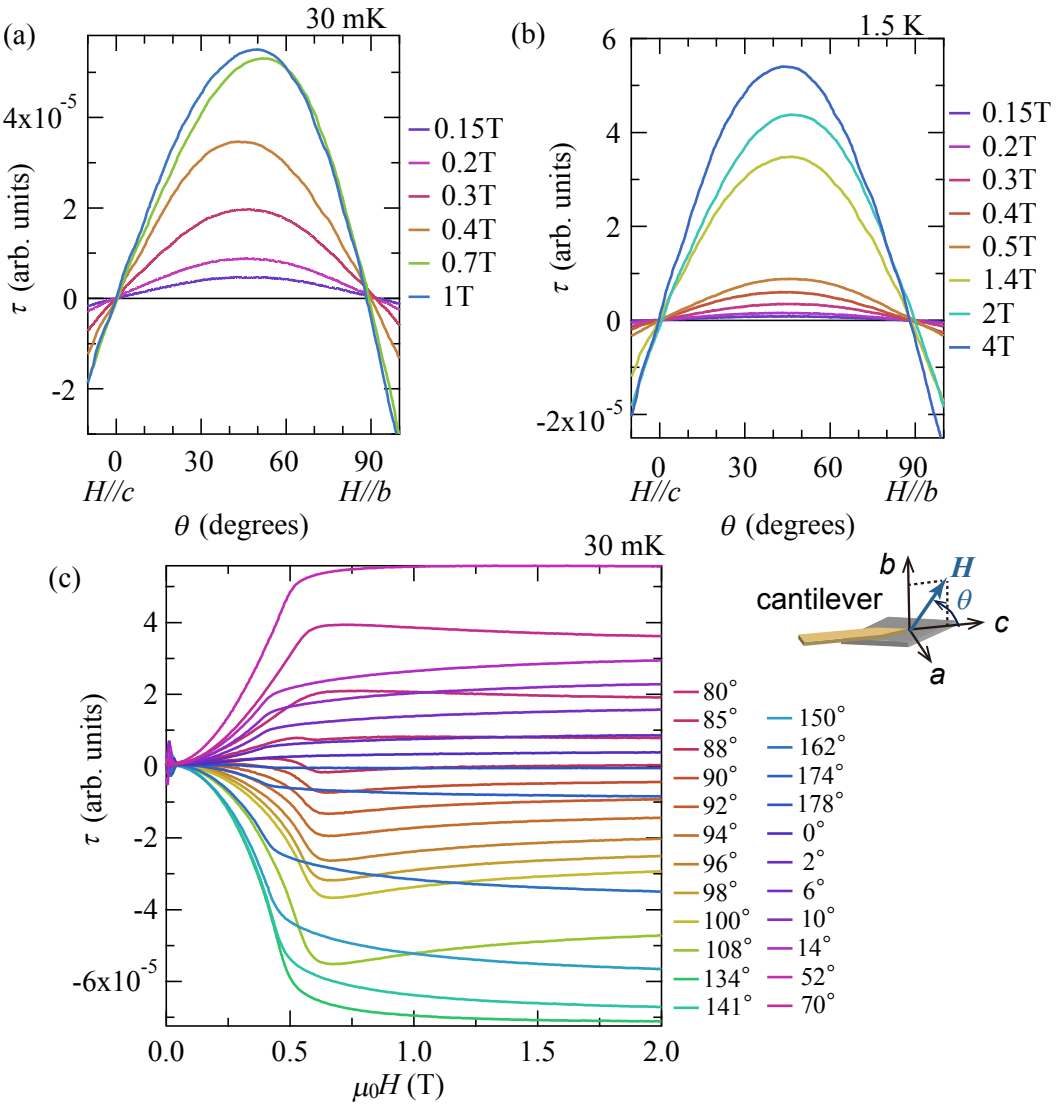

Figure 3.23: Field angle and magnetic field plots of magnetic torque for κ-(BDH-TTP)$_2$FeCl$_4$. Magnetic fields are rotated in the *cb*-plane at 30 mK and 1.2 K. Schematic shows the field direction and sample alignment.

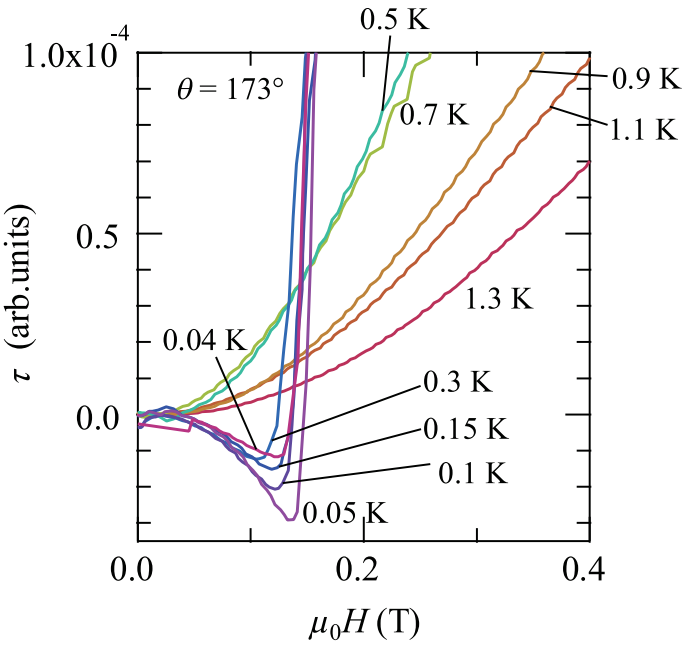

Figure 3.24: Field dependence of magnetic torque for κ-(BDH-TTP)$_2$FeCl$_4$ at various temperatures.

3.3.4 de Haas-van Alphen oscillation

The field dependence of the magnetic torque for κ-(BDH-TTP)$_2$FeCl$_4$ up to 35 T at 0.5 K is shown in Fig. 3.25(a). The field is rotated in the ab-plane and the field angle from the b-axis is denoted by θ for this measurement. Above 24 T, the de Haas-van Alphen (dHvA) oscillations are clearly observed [Fig. 3.25(b)]. Fig. 3.26(b) presents the Fourier transformation (FT) spectra of the oscillations, which have one peak around the frequency $F = 4760$ T, corresponding to approximately 100 % of the Brillouin zone (4596 T). F shows a $1/\cos\theta$ dependence, indicating a cylindrical Fermi surface.

The amplitude of the FT spectra A at $\theta = 0°$ diminishes with increasing temperature. By the Lifshitz-Kosevich formula, A/T is given as

$$A/T = a\frac{K\mu/H}{\sinh(K\mu T/H)}, \tag{3.9}$$

where a is a constant, $K = 14.7$, μ is the effective mass ratio. The A/T vs T plot (mass plot) is shown in Fig. 3.26(c). The effective mass ratio of the electron is calculated to be $\mu = m_c/m_e = 2.0$, where m_e is the mass of the free electron. Thus, some electron correlation exists in the $FeCl_4$ salt.

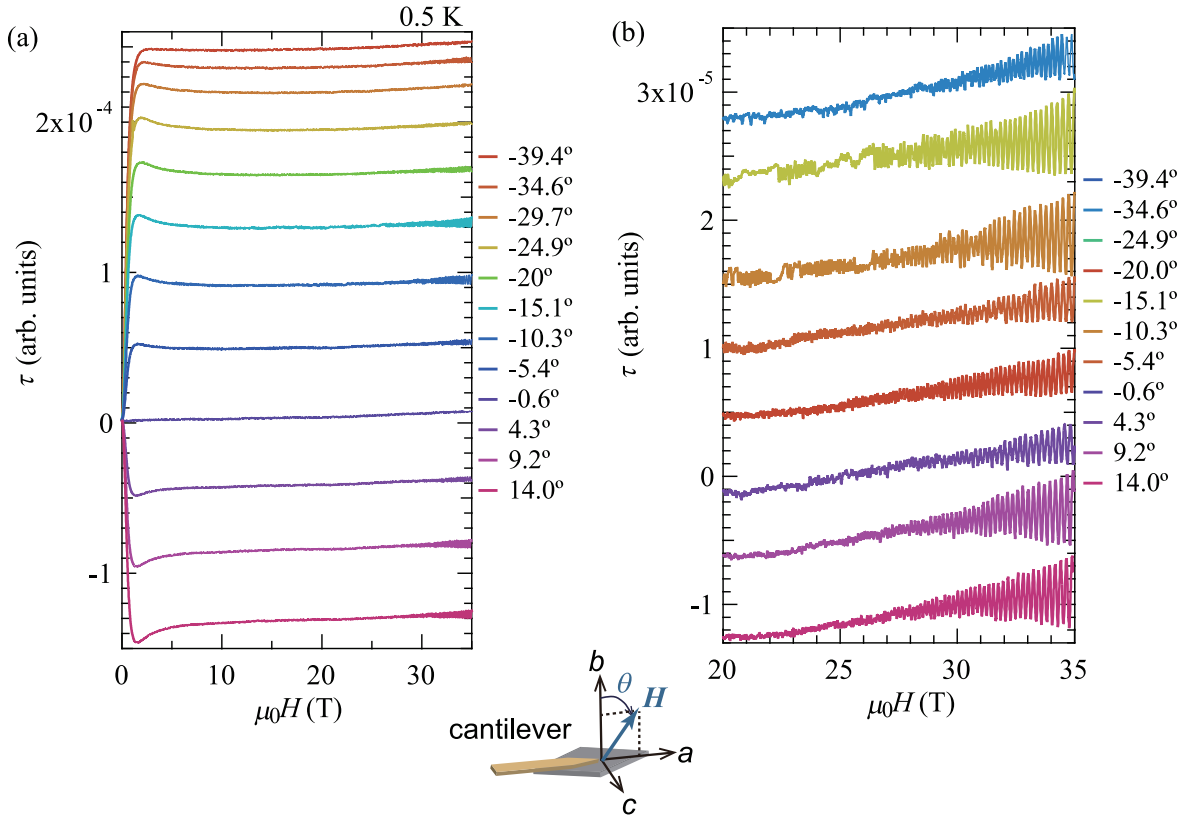

Figure 3.25: (a) Field dependence of magnetic torque for κ-(BDH-TTP)$_2$FeCl$_4$ at 0.5 T. (b) High field region of the dHvA oscillations. Schematic shows the field direction and sample alignment.

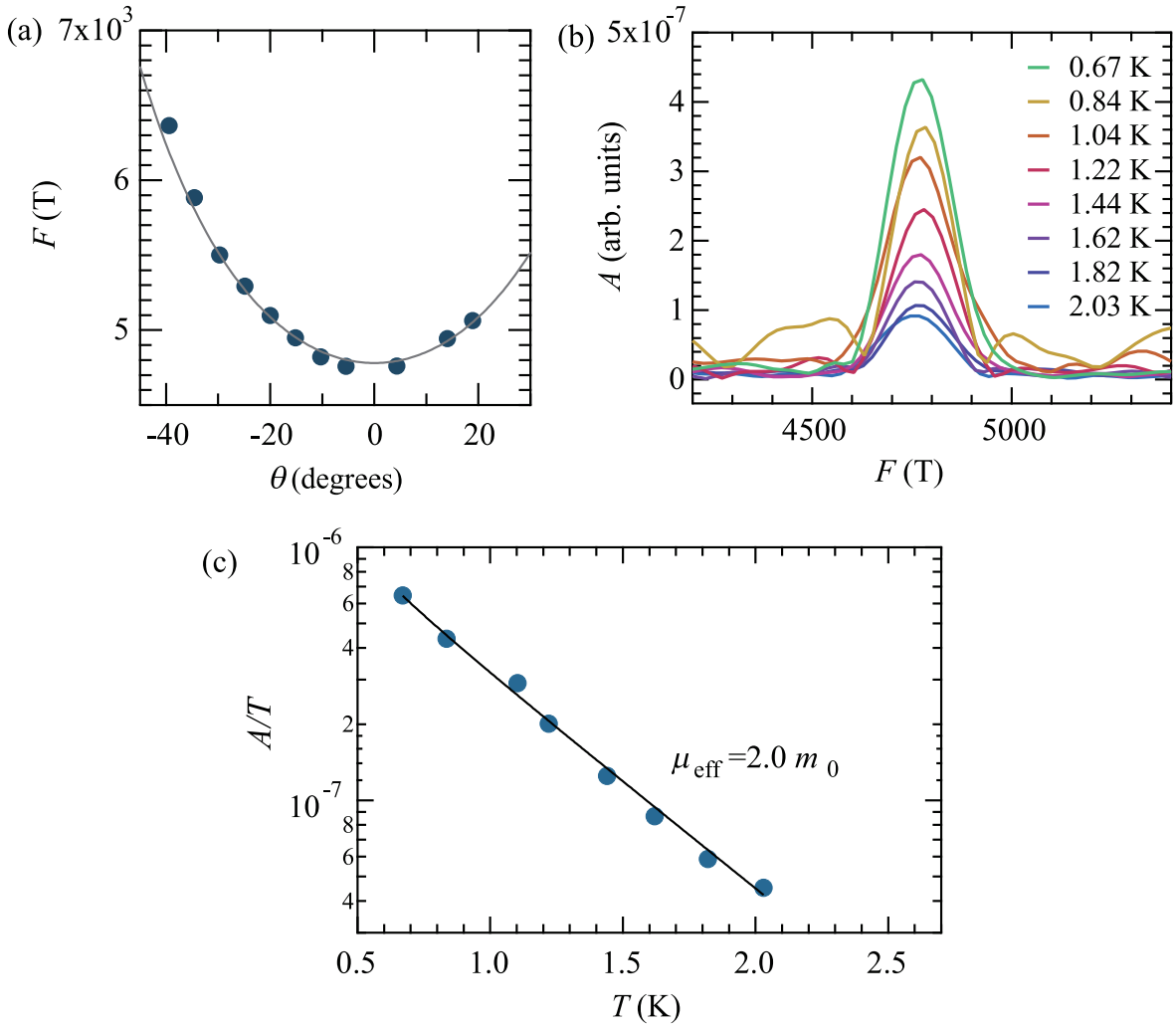

Figure 3.26: (a) FT amplitude vs. field angle plots for κ-(BDH-TTP)$_2$FeCl$_4$. (b) FT spectra of the oscillations at various temperatures. The FT amplitude shows the $1/\cos\theta$ dependence presented by a solid curve. (c) Mass plot. From the solid fitting curve, the effective mass ratio is estimated as $\mu = 2.0$.

3.4 Discussion for κ-(BDH-TTP)$_2$FeCl$_4$

3.4.1 ESR linewidth

Here, the contribution of the $3d$ spins to the ESR linewidth is considered as the ESR signal arises predominantly from the $3d$ spins. The observed ESR signal has a Lorentzian lineshape suggesting the exchange narrowing of the linewidth.

Similar to that for the $FeBr_4$ salt, the second moment M_2 is calculated for the $FeCl_4$ salt. The contribution of the crystal field to M_2 has a $\cos^2\theta$ dependence with a maximum value for $H \parallel a$ [Eq. (3.6)]. Assuming $|D| = 0.1$ K (see below) and $J = 0.2$ K, the calculated results are obtained as shown by the dotted curve in Fig. 3.18(a). In contrast, the Dzyaloshinskii-Moriya interaction,[85,86] gives $M_2^{\rm DM} \propto D_{\rm DM}^2$ and $D_{\rm DM} \approx [(g - g_0)/g_0]J$, where g_0 is the g-factor of the free electron. This term is negligible because of the negligible value of g-g_0.

The other dominant contribution arises from the dipole-dipole interaction between the $3d$ spins. The contribution to the second moment is given by Eq. (3.5). Taking $g = 2$ and $J = 0.2$ K, we obtain calculated results shown by the dashed curves in Figs. 3.18(a) and (b). Note that the dashed curves have a double-minimum dependence, qualitatively consistent with the experimental results. To obtain quantitative agreement, more realistic models are required that include the E term of the crystal field as well as the cross terms between the crystal field and dipole interaction effects in M_2. Although there still remain ambiguities in the calculations, we can conclude that the ESR linewidth arises mainly from both effects with $J \approx 0.2$ K.

3.4.2 Magnetic susceptibility and g-value

The magnetic susceptibility of the $FeCl_4$ salt follows the Curie-Weiss law with a low Weiss temperature [Fig. 3.15(b)], and the AF order occurs at a very low temperature ($T_{\rm N} \sim 0.4$ K). These results show that the AF interaction between the $3d$ spins in the $FeCl_4$ salt is much smaller than that in the $FeBr_4$ salt ($T_{\rm N} = 3.9$ K). Therefore, the characteristic temperature dependences of χT [Fig. 3.15(b)] and the g-values below 50 K [Fig. 3.17(b)] can be interpreted by a single-ion picture. Here, we consider the single-ion anisotropy described by the two parameters D and E. The spin Hamiltonian is given by

$$\mathcal{H} = \sum_i g_i \mu_{\rm B} H_i S_i + D S_z^2 + E\left(S_x^2 - S_y^2\right) \qquad (i = x, y, z), \tag{3.10}$$

where the first term corresponds to the Zeeman energy in the external field H_i, $\mu_{\rm B}$ is the Bohr magneton, g_i is the g-value of the electron spin, and S_x, S_y, and S_z are the spin operators ($S = 5/2$).[99] The total magnetic moment is given by the statistical average for the six sublevels of the $3d$ spins,

$$\langle M(T) \rangle = \frac{\sum_j M_j \exp\left(\frac{-E_j}{k_{\rm B}T}\right)}{\sum_j \exp\left(\frac{-E_j}{k_{\rm B}T}\right)} \qquad (j = 1, 2, \cdots, 6), \tag{3.11}$$

where M_j and E_j represent the magnetic moment and the eigenvalue for the jth sublevel, and $\langle M(T) \rangle$ is the statistical average of the total magnetic moment per mole, which corresponds to the experimental

data $\chi = \langle M(T) \rangle / H$. The temperature dependence of χT is calculated with the fitting parameters g_i, D, and E. The results calculated with $g_x = 1.998$, $g_y = 2.008$, $g_z = 2.006$, $D = -0.1$ K, and $E = 0.042$ K well describe the temperature dependence, as shown by the solid curves in Fig. 3.15(b). Here, x, y, and z correspond to the b-, c-, and a-axes, respectively. The magnetic easy axis is the a-axis, which is consistent with the torque data. The agreement with the experimental results seems satisfactory. For the calculation, the AF interaction between the $3d$ spins, J, is ignored. As shown in the previous subsections, J is estimated to be ~ 0.2 K, which is on the same order of magnitude as D. In the paramagnetic phase, the effect of the isotropic J leads to a shift in M in the mean field approximation. This does not cause a significant difference in the calculated results because the Weiss temperature determined by J is only ~ -0.2 K.

If the characteristic temperature dependences of the ESR g-values [Fig. 3.17(b)] have the same origin as those of the linewidths, we should see a strong correlation between them because $\chi T \approx K g(T)^2$ and $K = N_{\rm A} \mu_{\rm B}^2 S(S+1)/3k_{\rm B}$ (here $N_{\rm A}$ is the Avogadro constant). Figure 3.27 presents the plots of χT vs. g^2 in the temperature range 5-80 K. Although the data are somewhat scattered, we see a linear correlation, indicated by the dashed line. This result strongly indicates that the characteristic temperature dependences of the g-value and χT originate from the same effect as the anisotropic crystal field. The solid line corresponds to the case of isolated paramagnetic spins with $K = 1.1$. The discrepancy may be caused by the effect of finite J because the g-factors are more sensitive to a molecular field proportional to J.

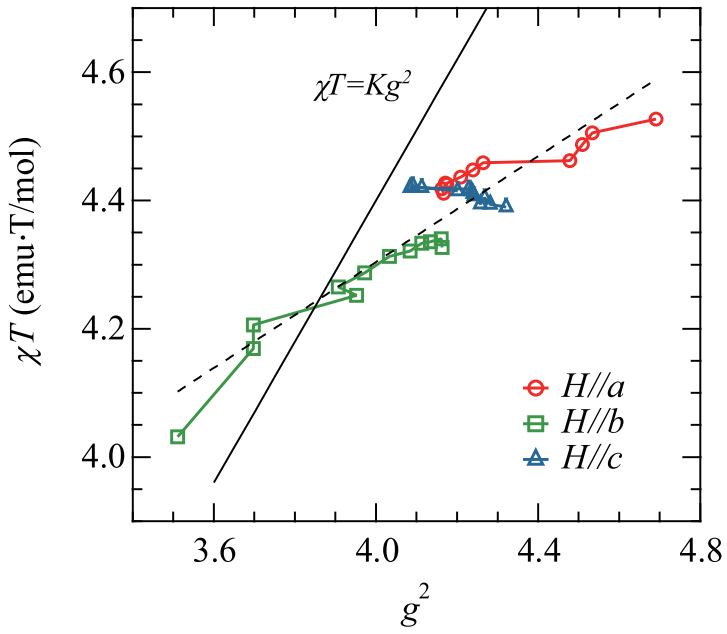

Figure 3.27: χT vs. g^2 plots in the temperature range between 5 K and 80 K. Solid line corresponds to the case of isolated paramagnetic spins. Dashed line denotes the least square fitting.

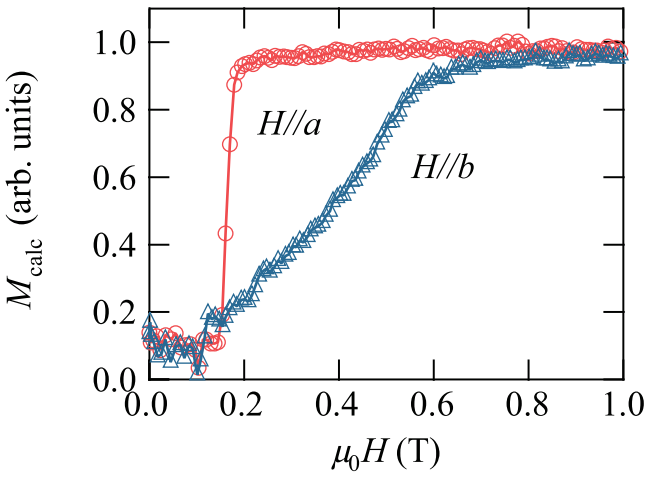

Figure 3.28: Feld dependence of the calculated magnetization from MR data at 30 mK.

3.4.3 Magnetoresistance

In the previous section, we proposed quantum tunneling between the layers as a simple model of the interlayer transport. Similar arguments can be applied to the $FeCl_4$ salt.

After subtracting the quadratic background arising from the orbital effect,[37] we obtain from the MR data at 30 mK the $M_{calc}(H)$ curves for $H \parallel a$ and b shown in Fig. 3.28. $M_{calc}(H)$ for $H \parallel a$ shows a rapid increase at 0.15 T, which corresponds to the spin-flop transition, and then saturates above 0.2 T. In contrast, with increasing field, $M_{calc}(H)$ for $H \parallel b$ monotonically increases with the field, and then saturates above 0.7 T. This gradual increase in the field perpendicular to the easy axis is a typical behavior of antiferromagnets.

3.4.4 Comparison of results for the $FeCl_4$ and $FeBr_4$ salts

Table 3.1: Comparison of parameter values obtained for κ-(BDH-TTP)$_2$$FeCl_4$ and κ-(BDH-TTP)$_2$$FeBr_4$.

salt	$\lvert D^{exp}\rvert$	T_N^{exp}	H_{SF} [a]	$\Delta\rho/\rho_0$ [b]	J_d^{calc} [c]	$J_{\pi d}^{calc}$ [d]	T_N^{calc}
$FeCl_4$	0.1 K	0.4 K	0.15 T	20%	0.22 K	2.1 K	1.34 K
$FeBr_4$	0.38 K	3.9 K	2.0 T	50%	0.62 K	5.7 K	4.0 K

[a] For $H \parallel a$ at 30 mK.

[b] Reduction ratio of the MR at the spin-flop field.

[c] Calculated d-d interaction.[56]

[d] Calculated effective π-d interaction.[56]

Here, it will be worthwhile to compare the physical parameters characterizing the electronic states of the $FeCl_4$ and $FeBr_4$ salts. Several parameters are summarized in Table 3.1. The experimentally determined T_N^{exp} (0.4 K) of the $FeCl_4$ salt is one order of magnitude lower than that (3.9 K) for the $FeBr_4$ salt. Concomitantly, the spin-flop field H_{SF} (0.15 T) in the $FeCl_4$ salt is lower than that (2.0 T) for the $FeBr_4$ salt. In π-d systems, the donor—anion distance provides important information on the

π-d interaction. For the $FeCl_4$ salt, the shortest distance between the sulfur atom of BDH-TTP and the chlorine atom of the $FeCl_4^-$ anion (S—Cl distance) is 3.661(2) Å, which is somewhat longer than the sum of the van der Waals radii [vdW (Bondi) = 3.55 Å]. In contrast, the shortest S—Br distance in the $FeBr_4$ salt is 3.715(3) Å, which is closer to vdW (Bondi) = 3.65 Åthan the difference (∼0.11 Å) between the shortest S—Cl distance and the vdW radii in the $FeCl_4$ salt. This structural distinction between the $FeCl_4$ and $FeBr_4$ salts should result in the lower T_N^{exp} and H_{SF} observed in the $FeCl_4$ salt.

The MO calculations using the mean field approximation that were previously reported,[56] show that the d-d exchange interaction of $J_d = 0.22$ K and the effective π-d interaction $J_{\pi d}$ for the $FeCl_4$ salt are about one-third of those for the $FeBr_4$ salt. Consequently, the $FeCl_4$ salt has a smaller T_N^{calc} (= 1.34 K) in the mean field approximation. However, this value is rather high as compared with T_N^{exp}. Assuming $k_B T_N^{exp} \approx (2/3)|J_d|S(S+1)$, we obtain $|J_d| \approx 0.07$ K. This value is rather small compared with $|J| \approx 0.2$ K, estimated from the ESR linewidth analysis.

The reduction ratios for the MR in the $FeCl_4$ and $FeBr_4$ salts in the spin-flop transition at 30 mK are ∼20 and ∼50%, respectively. The reduction ratio reflects the amplitude of the effective π-d interaction $J_{\pi d}$ (2.1 K for the $FeCl_4$ salt and 5.7 K for the $FeBr_4$ salt) as the spin-dependent tunneling conductance is directly related to the magnetic potential formed by the π-d interaction.

In the uniaxial crystal field, the spin-flop field H_{SF} is simply given by $H_{SF} = \sqrt{2|H_A H_E|} = (2/\mu_B)\sqrt{|J_d D|}$, where H_A is the anisotropic field and H_E is the exchange field. Taking $J_d = 0.07$ K and $|D| = 0.1$ K for the $FeCl_4$ salt and $J_d = 0.62$ K and $|D| = 0.38$ K for the $FeBr_4$ salt, we obtain $H_{SF} = 0.25$ and 1.44 T for the $FeCl_4$ and $FeBr_4$ salts, respectively. $H_{SF} = 0.25$ T is in approximate agreement with the experimental value of $H_{SF} = 0.15$ T.

In contrast to the monotonic temperature dependence of the linewidth in the $FeBr_4$ salt above 50 K, the linewidth in the $FeCl_4$ salt has a peculiar temperature dependence [Fig. 3.17(a)], the origin of which is not clear at present. Additionally, the linewidth in the $FeBr_4$ salt shows critical behavior (a rapid increase) for different field directions when approaching T_N below 50 K, whereas such a phenomenon is not found in the $FeCl_4$ salt down to 3.5 K. The absence of critical behavior is most likely because of the small exchange interaction in the $FeCl_4$ salt compared with that in the $FeBr_4$ salt.

The angular dependence of the ESR linewidth in the $FeBr_4$ salt is considerably different from that in the $FeCl_4$ salt. For the $FeBr_4$ salt, the major contribution to the ESR linewidth is not the dipole interaction but the crystal field effect. Therefore, a simple $1+\cos^2\theta$ dependence is observed for the $FeBr_4$ salt. Indeed, these results are consistent with the analyses of the susceptibility anisotropy; the $FeBr_4$ salt has a larger crystal field parameter $|D|$ ($\sim$ 0.38 K) than the $FeCl_4$ salt ($\sim$ 0.1 K). The large $|D|$ for the $FeBr_4$ salt is a consequence of the larger distortion in the $FeBr_4$ tetrahedral structure because of the larger ionic radius.

3.4.5 Magnetic torque simulations

To explain the magnetic torque data, a simple two-spin model is proposed, which corresponds to two magnetic sublattices [Fig. 3.29(c)]. The magnetic properties of the $FeBr_4$ and $FeCl_4$ salts are dominated by the $3d$ spins with large magnetic moments. The $3d$ spins on the nearest-neighbor Fe ions along the a-axis are antiferromagnetically coupled with each other. The AF coupling occurs via two different pathways: one direct and the other indirect via the π-d interaction.[56] As discussed previously, the ligand field of the $3d$ spin has an approximate uniaxial symmetry, so that the total energy E of the two $3d$ spins with the exchange coupling J in a field H will be mainly given by the sum of the Zeeman effect, the exchange interaction, and the anisotropic ligand field,

$$E = E_{Zeeman} + E_{exchange} + E_{anisotropy}, \tag{3.12}$$

$$E_{Zeeman} = -g\mu_{\rm B}S_1H\cos(\varphi_1 - \theta) + g\mu_{\rm B}S_2H\cos(\varphi_2 - \theta), \tag{3.13}$$

$$E_{exchange} = -JS_1S_2\cos(\varphi_2 - \varphi_2), \tag{3.14}$$

$$E_{anisotropy} = -D(S_1^2\cos^2\varphi_1 + S_2^2\cos^2\varphi_2), \tag{3.15}$$

where S_1 and S_2 are the $3d$ spins ($S_1 = S_2 = 5/2$), φ_1 and φ_2 are the respective angles for S_1 and S_2 from the easy axis (a-axis) [Fig. 3.29(c)], θ is the field angle from the easy axis, and D (> 0) is the uniaxial anisotropy parameter of the ligand field. The spin angles φ_1 and φ_2 are determined so that the total energy has a minimum at a fixed θ and H. The magnetic moment M per spin and the total torque τ are obtained from the following relations,

$$M(H,\theta) = \frac{1}{2}[g\mu_{\rm B}S_1\cos(\varphi_1 - \theta) - g\mu_{\rm B}S_2\cos(\varphi_2 - \theta)], \tag{3.16}$$

$$\tau(H,\theta) = -\partial E/\partial\theta. \tag{3.17}$$

In this simulation, the temperature fluctuation is not included; the results should therefore be compared with the data taken at very low temperatures ($T \ll D$ and $T \ll J$).

The simulations for the $FeBr_4$ salt with the parameter values $D = 0.26$ and $J = 1.02$ K are shown in Figs. 3.29(a), (b), and (d). For $H \parallel a$ ($\theta = 0°$), the $M(H)$ curve shows a sharp increase and a spin-flop transition at 1.7 T [Fig. 3.3(a)], and is saturated above 2.8 T, where the full Bohr magneton ($5\mu_{\rm B}$ per spin) is induced. For $H \parallel b$ ($\theta = 90°$), the $M(H)$ curve linearly increases with increasing H, and saturates above 4.7 T. The $\tau(H)$ curve has a peak at the spin-flop transition. The field dependences of both φ_1 and φ_2 at $\theta = 10°$ in Fig. 3.29(b) clearly show jumps at the spin-flop transition. Above the saturation field of $M(H)$, we note that the $\tau(H)$ curves become constant. Below the spin-flop field of 1.7 T, the $\tau(\theta)$ curves in Fig. 3.29(d) are given by the $\sin 2\theta$ dependence . In the intermediate

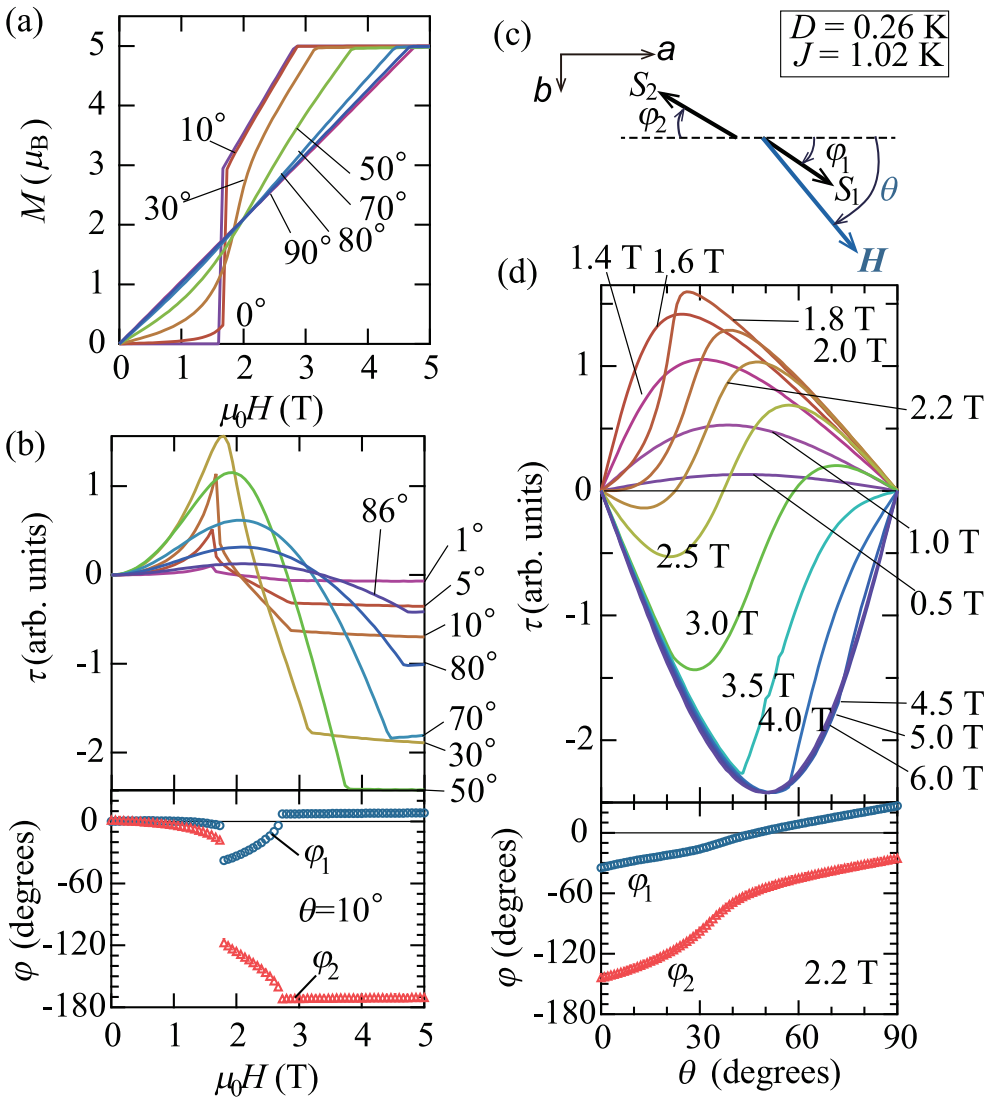

Figure 3.29: Simulations of (a) magnetization and (b) magnetic torque as a function of field at various field angles and the field dependences of the two spin angles at a field angle $\theta = 10°$. (c) Schematic of two d spins and spin angles. (d) Field angle dependence of the simulated magnetic torque and the two spin angles at 2.2 T. The parameter values $D = 0.26$ and $J = 1.02$ K were fitted to reproduce the experimental data for κ-(BDH-TTP)$_2$FeBr$_4$.

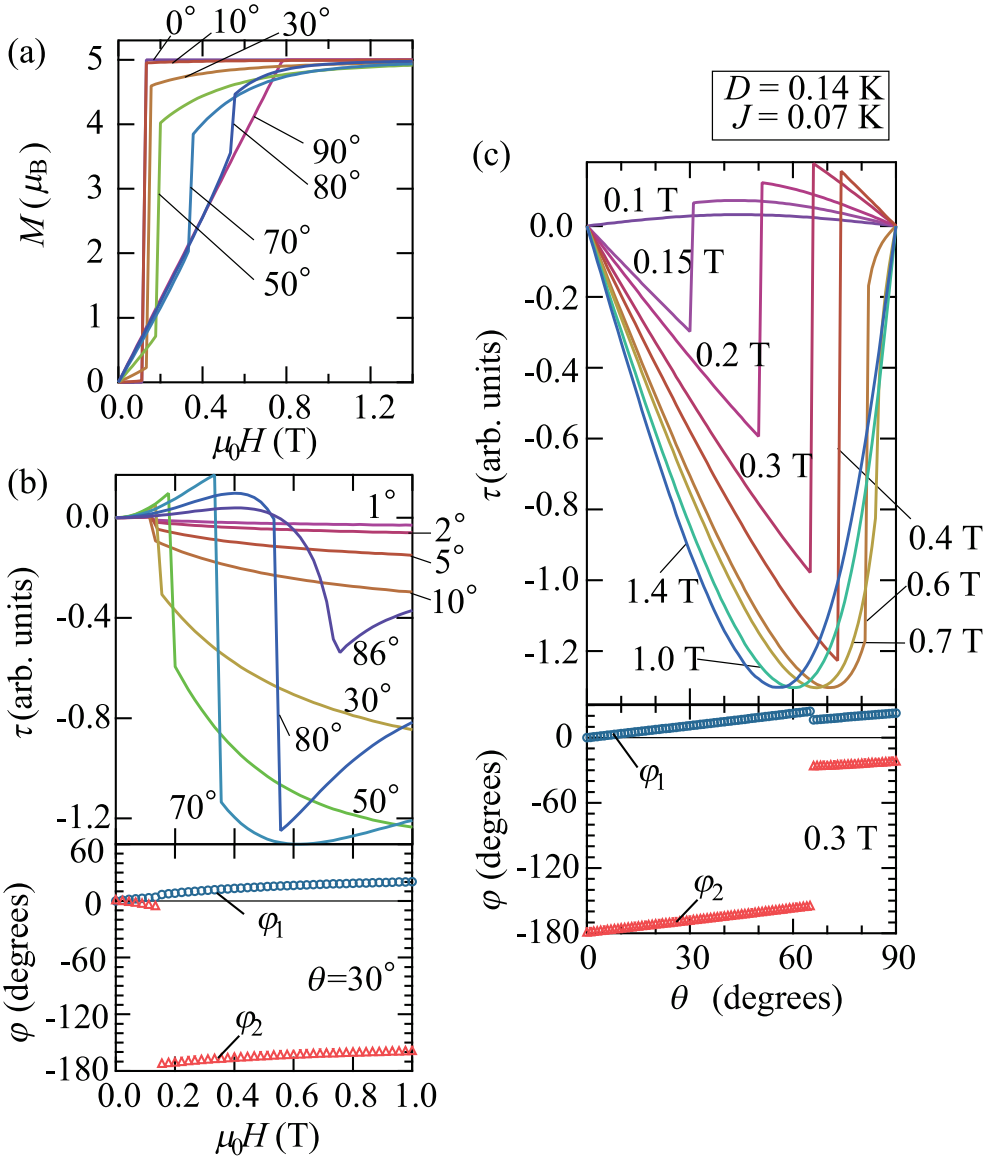

Figure 3.30: (a) Simulations of (a) magnetization and (b) magnetic torque as a function of field at various field angles and the field dependences of the two spin angles at a field angle $\theta = 30°$. (c) Field dependence of the simulated magnetic torque and the two spin angles at 0.3 T. The parameter values D= 0.14 and $J = 0.07$ K are were fitted to reproduce the experimental data for κ-(BDH-TTP)$_2$FeCl$_4$.

region between the spin-flop and the saturation fields, the $\tau(\theta)$ curve shows a sign change in the range $0^\circ < \theta < 90^\circ$. This is caused by a gradual but large change in the spin angles as shown in Fig. 3.29(d). Above the saturation field, the $\tau(\theta)$ curve approaches the $\sin 2\theta$ dependence and becomes field-independent. All these features are consistent with the experimental data.

The simulations on the $FeCl_4$ salt with the parameters $D = 0.14$ K and $J = 0.07$ K are illustrated in Fig. 3.30. Because of the small J ($J < D$), a metamagnetic transition (not a spin-flop transition) takes place in fields nearly parallel to the a-axis. Indeed, the $M(H)$ curve at $\theta = 0^\circ$ clearly shows a jump to the full moment at ~ 0.13 T [Fig. 3.30(a)]. At the metamagnetic transition, the $\tau(H)$ curve exhibits a peak, followed by a steep change [Fig. 3.30(b)]. This change is caused by a large spin angle jump for S_2 as shown in Fig. 3.30(b). As the field is tilted away from the a-axis, the metamagnetic transition is suppressed, and only a smooth change is seen with $\theta > 85^\circ$. In the $\tau(\theta)$ curves [Fig. 3.30(c)], sudden changes are also evident, which are attributed to the spin angle jumps (metamagnetic transition). These simulations reproduce the experimental data for the $FeCl_4$ salt.

We note some discrepancies between the experimental data and the simulations. For instance, the $M(H)$ curves in the experimental data show smooth changes at the transition fields in comparison with those in the simulations. This would be ascribed to the temperature fluctuation effect. Some other details are not completely reproduced by the simulations probably due to the presence of the bi-axial anisotropy of the ligand field, Dzyaloshinsky-Moriya interaction, and/or finite π-d interaction, as discussed in previous chapter. However, the essential features of the magnetic properties in organic π-d systems are reproduced by our proposed two-sublattice model. Along with the simulations, the torque measurements will be re-recognized as a powerful tool to determine the microscopic parameters of the AF ordered states.

Chapter 4

Results and Discussion for α-(BEDT-TTF)$_2$NH$_4$Hg(SCN)$_4$

4.1 Results

4.1.1 Temperature dependence of resistivity

The temperature dependences of the resistivities of nine samples (♯1-♯9) are shown in Fig. 4.1(a). The superconducting transition is observed at ∼1 K for all the samples ($T_c \approx 1$ K), which is consistent with the previous reports. However, the temperature dependence is strongly sample-dependent. For samples ♯1-♯5, the resistivities have broad humps at 110-150 K and then decrease with decreasing temperature, whereas the resistivities monotonically decrease with decreasing temperature in the whole temperature region for samples ♯7-♯9. Such resistivity humps have been observed in some 2D layered compounds as discussed later. The resistivity humps are more evident for samples with lower residual resistivity ratios defined as RRR = ρ_{290K}/ρ_{2K} as shown in Fig. 4.1(b). The inset of Fig. 4.1(b) shows the hump resistivity normalized at 290 K (ρ_{hump}/ρ_{290K}) vs. RRR plot. The ρ_{hump}/ρ_{290K} value has a tendency to decrease with increasing RRR. We see no significant correlation between RRR and T_c, and between ρ_{hump}/ρ_{290K} and T_c.

4.1.2 Shubnikov-de Haas oscillation

The field dependences of the resistance are shown in Fig. 4.2. The SdH oscillations are clearly observed above 4 T for sample ♯1. The Fourier transform (FT) spectrum of the oscillation [Fig. 4.3(a)] shows a single frequency of about 560 T, corresponding to the α orbit [shown in Fig. 4.14(a)], and its harmonics (2α and 3α). Figure 4.3(b) shows the angular dependence of the oscillation frequency $F[T]$. The frequency is proportional to $1/\cos\theta$, where θ denotes the field angle from the b-axis (interlayer direction). The $1/\cos\theta$ dependence and no node of the oscillation clearly show that the observed Fermi surface is highly 2D.

The energy band of a simple cylindrical 2D Fermi surface with a corrugation given by t_z will be approximated by $E = \hbar^2 k_F^2/2m_c - 2t_z\cos(k_z c)$. We define the Fermi energy, $E_F = \hbar^2 k_F^2/2m_c = \hbar^2 S_F/2\pi m_c$, where $S_F = \pi k_F^2$ is the cross-sectional area. Because of the finite t_z value, the corrugated 2D Fermi surface has the maximum and minimum cross-sectional areas, $S_{max} = 2\pi m_c(E_F + 2t_z)/\hbar^2$ and $S_{min} = 2\pi m_c(E_F - 2t_z)/\hbar^2$, respectively, giving two different oscillation frequencies. Therefore, if the t_z value is sufficiently large, we will observe nodes formed by the two frequencies arising from

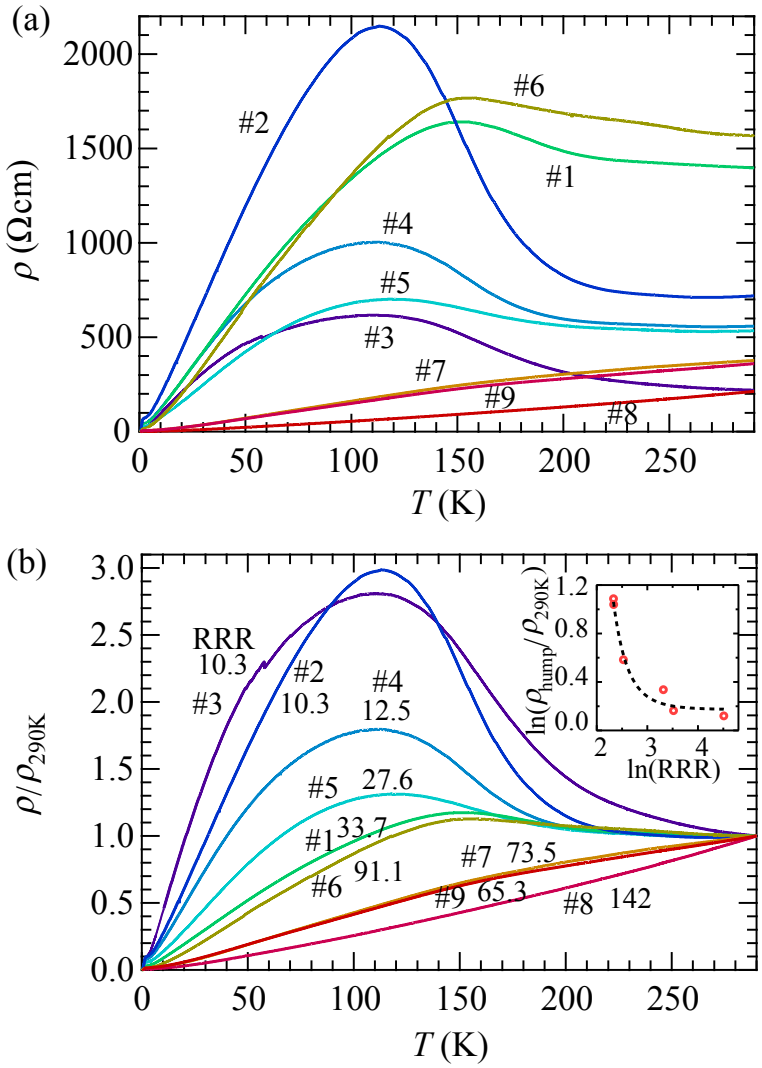

Figure 4.1: (a) Temperature dependences of the resistivity for various samples. (b) Normalized resistivity at 290 K for α-(BEDT-TTF)$_2$NH$_4$Hg(SCN)$_4$. Inset: Log plots of normalized height of the hump vs. RRR.

$S_{\max}$ and $S_{\min}$. We have carefully observed the SdH oscillations, but found no sign of such nodes in the range between 4 T and 17.5 T. The result shows that the difference of the two frequencies given by $\Delta F = (S_{\max} - S_{\min})/2\pi e\hbar$ follows the relation $\Delta F(1/4 - 1/17.5) \leq 1/2$. It gives the upper limit of t_z, $t_z \leq 0.03$ meV.[100]

The Landau levels are broadened by the scattering of the electrons, which is mainly caused by impurities or defects at low temperatures. The scattering gives the width of $\sim \hbar/\tau$, where τ is the scattering time. This broadening reduces the oscillation amplitude and the reduction factor is characterized by the Dingle temperature $T_{\rm D} = \hbar/(2\pi k_{\rm B}\tau)$, where $k_{\rm B}$ is the Boltzmann constant. We can estimate $T_{\rm D}$ from the so-called Dingle plot (Fig. 4.4), fitting the field dependence of the oscillation amplitude A by the equation,

$$\ln\left[AH\sinh\left(K\mu T/H\right)\right] = K\mu T_{\rm D}/H + a, \tag{4.1}$$

where $K = 14.7$ [T/K], μ is the ratio of the effective mass to the free electron mass $\mu = m_c/m_e =$

2.5, and a is a constant.[59,61] We estimated T_D for six samples, which ranges from 0.93 to 1.73 K as listed in Table 4.1. For samples ♯7-♯9, we cannot calculate T_D because the oscillations are too small, probably $T_D > 2$ K.

Table 4.1: Sample dependence of the Dingle temperature.

sample	♯1	♯2	♯3	♯4	♯5	♯6
T_D (K)	0.93	1.16	1.19	1.22	1.40	1.73
τ ($\times 10^{-12}$ s)	1.31	1.04	1.02	1.00	0.87	0.70

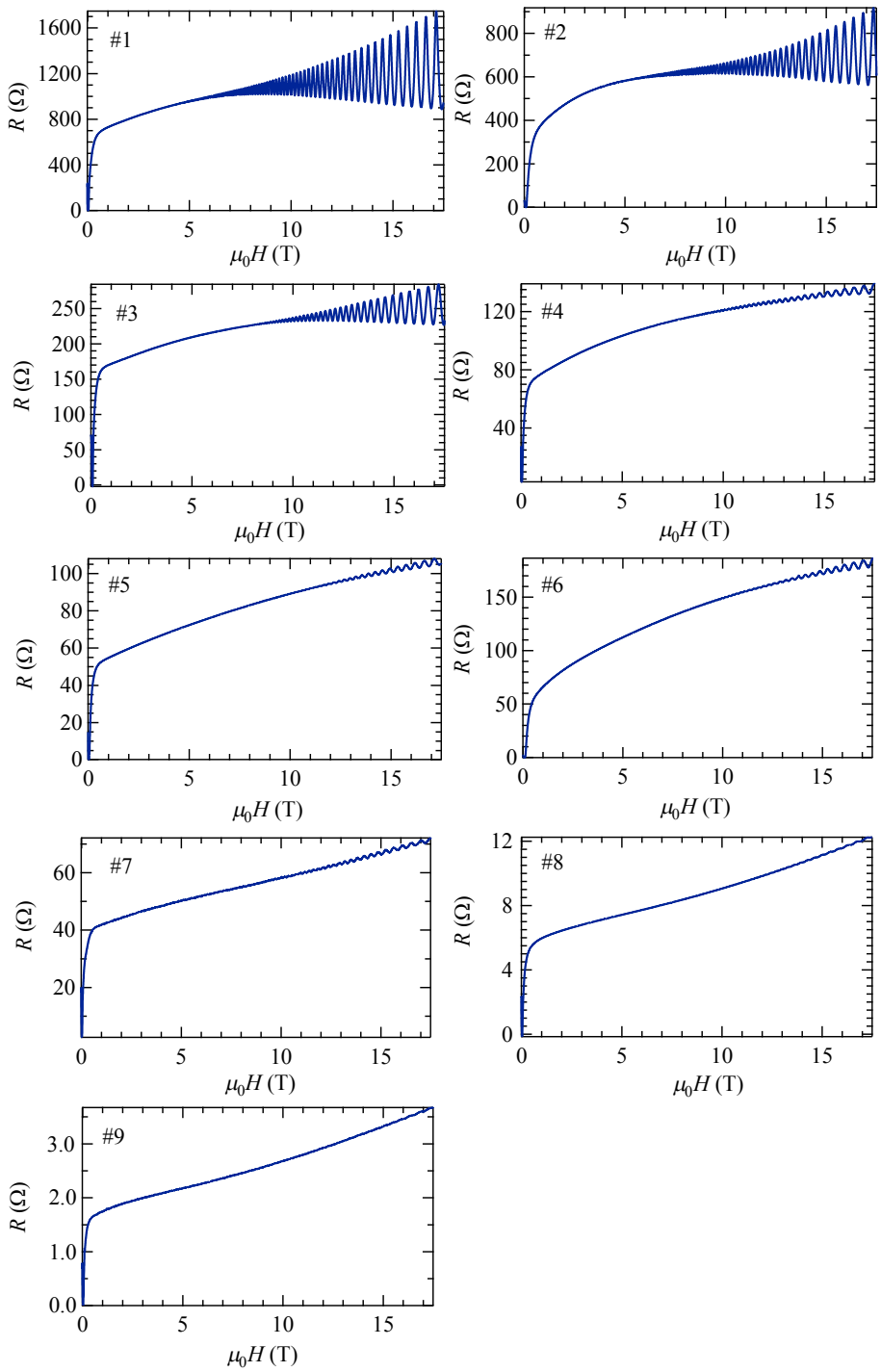

Figure 4.2: Resistances as a function of magnetic field at 0.3 K for α-(BEDT-TTF)$_2$NH$_4$Hg(SCN)$_4$. The SdH oscillations are clearly observed at high fields for samples ♯1-♯6.

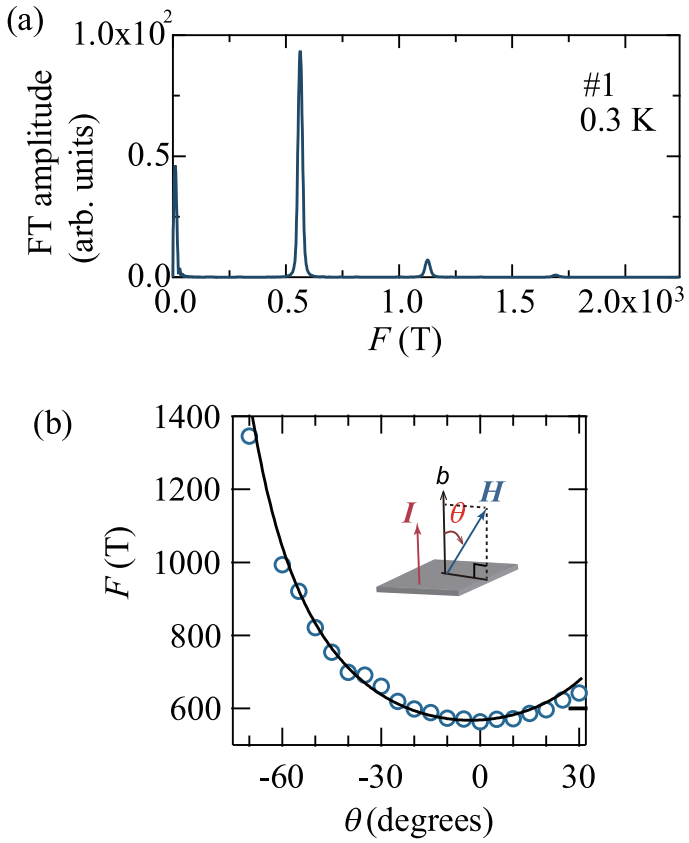

Figure 4.3: (a) FT amplitude vs. the quantum oscillation frequency F(T) at 0.3 K for sample ♯1. (b) Angular dependence of F(T). The solid curve shows the result calculated by $F(\mathrm{T}) = F_0/\cos\theta$ (F_0 =560 T). Inset: Schematic of the crystal and field angle.

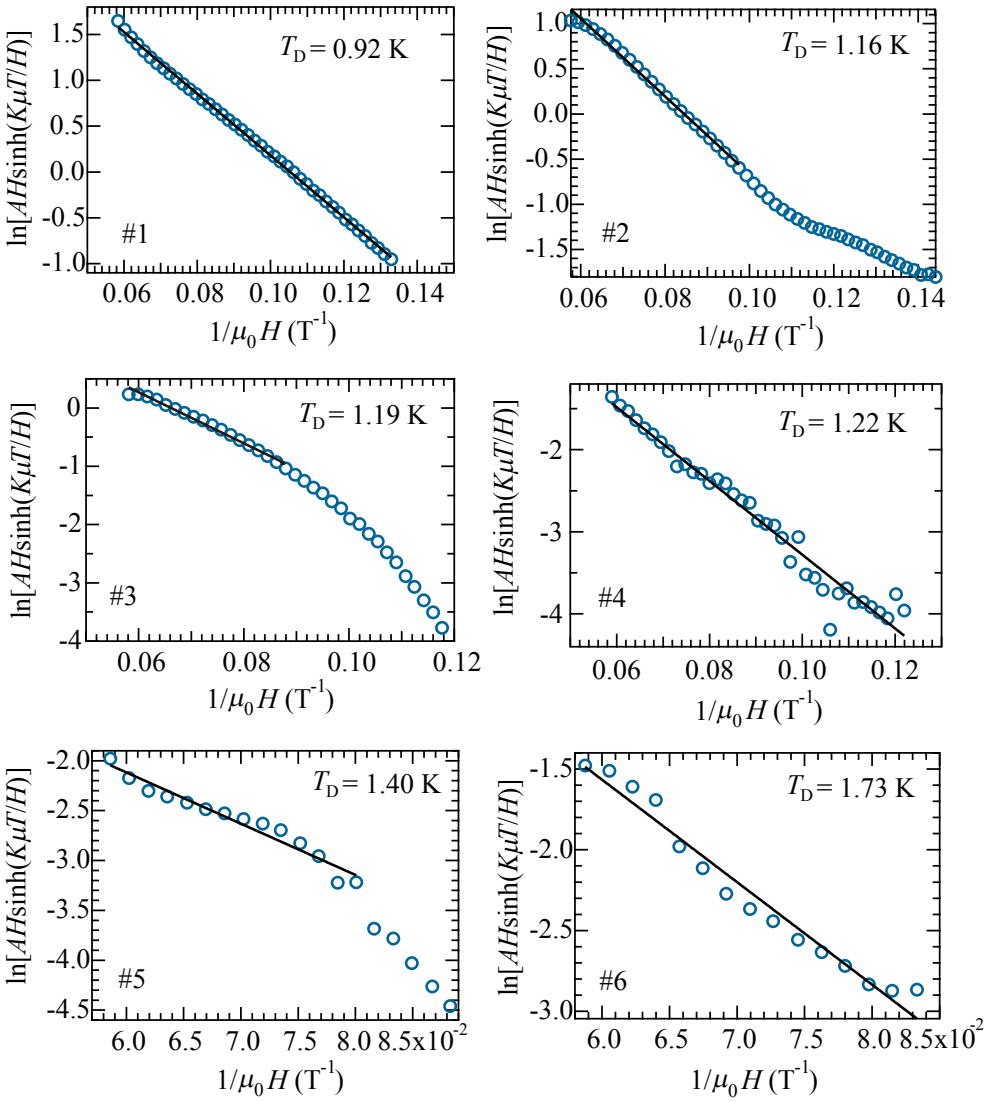

Figure 4.4: Dingle plots of the SdH oscillation for samples ♯1-♯6.

4.1.3 Angular dependent magnetoresistance

The angular dependences of the MR for some samples at 0.3 K are shown in Figs. 4.5 and 4.6. At low fields under 3 T, the resistances decrease to zero around $\theta = 90°$, due to the superconducting transition. The MR above 3 T strongly depends on the T_D (sample quality). For sample ♯1 with $T_D = 0.93$ K, the MR at high field shows large AMROs, where the small and rapid SdH oscillation is superimposed, as shown in Fig. 4.5(a). The background MR has a maximum around 90° and a minimum around 0°. The AMRO is slightly asymmetric around 90° because of the monoclinic structure.

For samples ♯5 ($T_D = 1.40$ K) and ♯6 ($T_D = 1.73$ K), V-shaped dips around $\theta = 90°$ appear at high fields and the AMRO amplitudes are suppressed [Figs. 4.5(c) and (d)]. We note that the angle region of the V-shaped dip is wider for the larger T_D sample. In the other angle region, the MR is similar to that for sample ♯1. For sample ♯9 (T_D is unknown), the angular dependence of the MR has no AMRO and the MR is completely reversed in all the angle region at high fields [Fig. 4.6(b)].

To reproduce the experimental results in Fig. 4.5(a), we calculated the AMROs by Eq. (2.41) for several $\omega_c\tau$ values in Fig. 4.7. Using the Fermi wave number $k_F = 1.35$ nm^{-1} of the α orbit and the layer spacing $c = 2.06$ nm, we take $k_F c = 2.78$. For $\tau = 3$ ps, giving $\omega_c\tau = 3.6$ at 17 T, we note that the relative amplitudes of the successive AMRO peaks for sample ♯1 at various fields in Fig. 4.5(a) are well reproduced as shown in Fig. 4.7(a). The scattering time τ used in the calculation is longer than the value obtained by the Dingle plot ($\tau = 1.31$ ps). This is because the AMRO amplitude is not sensitive to small-angle scattering whereas the SdH oscillation is reduced by any scattering losing the phase coherence. We also show the calculated AMROs at different τ values in Fig. 4.7(b), which should be compared with the data of the other samples with shorter τ in Figs. 4.5(b)-(d) and 4.6. As τ reduces, the MR background and the AMRO peaks gradually decrease and the MR approaches a simple sine curve with a maximum at $\theta = 90°$. These calculations are apparently inconsistent with the experimental results.

The V-shaped dip around $\theta = 90°$ can never be explained by the Boltzmann transport theory and indicates the incoherent interlayer transport. For sample ♯9, the SdH oscillations and the AMRO peaks are slightly observed. The MR background reversal, the incoherent interlayer transport, occurs in almost the whole angle region [Fig. 4.6(b)]. As discussed later, the background reversal at high fields is scaled by the perpendicular field component to the ac-plane ($H\cos\theta$). Such behavior has already been found for $(TMTSF)_2PF_6$[29] and α-$(BEDT\text{-}TTF)_2KHg(SCN)_4$.[41] Our data show that the crossover of the interlayer transport from the weakly coherent to incoherent regime is induced by the scattering.

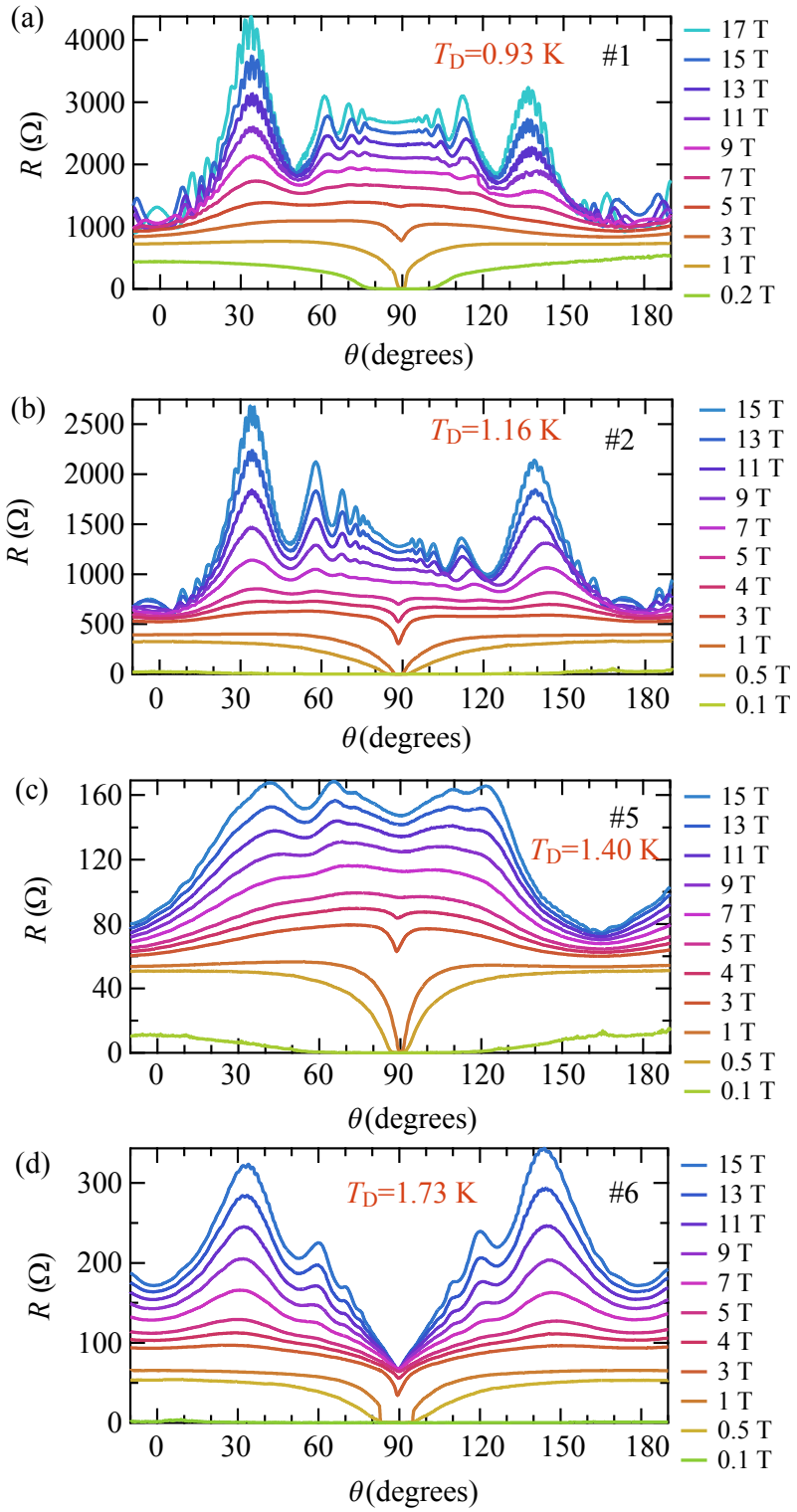

Figure 4.5: Angular dependences of the resistances at 0.3 K for α-(BEDT-TTF)$_2$NH$_4$Hg(SCN)$_4$.

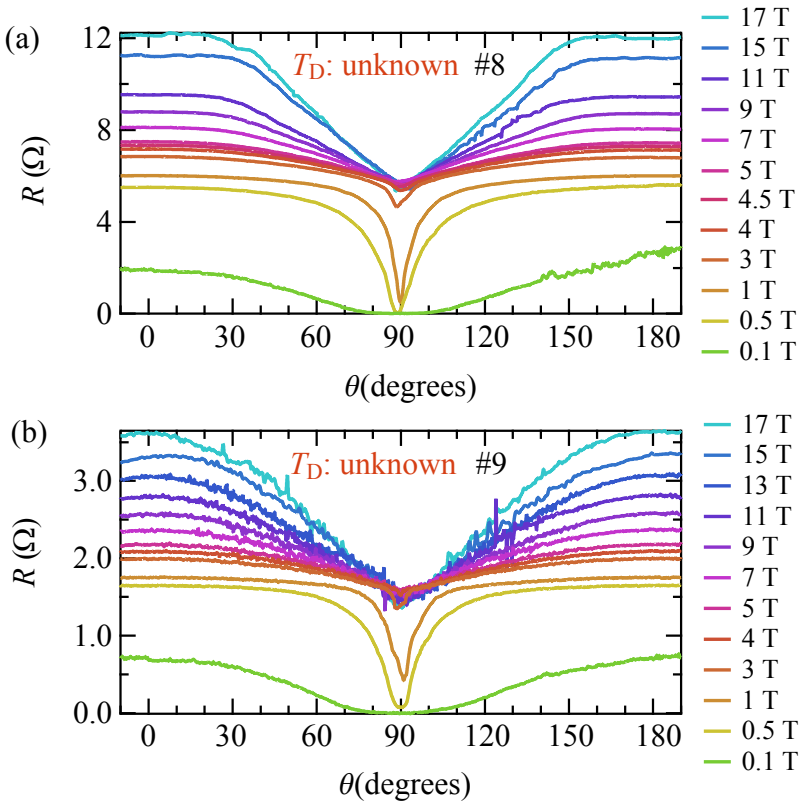

Figure 4.6: Angular dependences of the resistances at 0.3 K for α-(BEDT-TTF)$_2$NH$_4$Hg(SCN)$_4$.

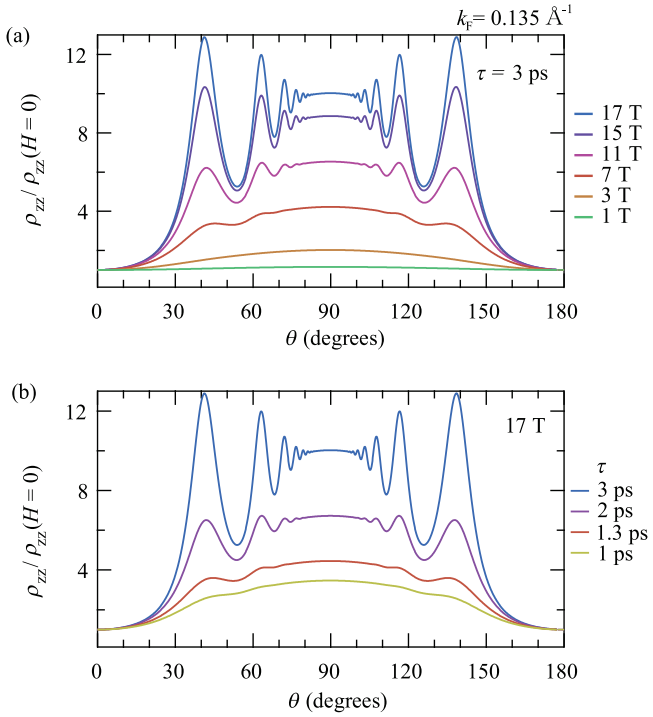

Figure 4.7: Simulated MR as a function of the field angle with $k_F = 1.35$ nm^{-1}. Simulations for (a) $\tau = 3$ ps at various fields and (b) $\mu_0 H = 17$ T at various scattering time τ.

The horizontal angular dependences of the MR at various azimuthal angles from the a-axis (ϕ) are presented in Figs. 4.8 and 4.9. For samples ♯1-♯3, the AMRO strongly depends on ϕ, reflecting the anisotropy of the Fermi surface structure. The V-shaped MR reversal around $\theta = \pm 90°$ is evident around $\phi = 45°$ and 225° but not clearly observed at the other angles. For sample ♯7, it is surprising that the MR is almost independent of ϕ and the V-shaped feature appears around $\theta = \pm 90°$ at all the ϕ values [Fig. 4.9(c)]. These features stand out in the polar plots of the resistances at $\theta = \pm 90°$ as shown in Fig. 4.10. For sample ♯2, the polar plot has a dumbbell shape with sharp dips. The sharp dips are evident in the $\phi = 45°$ direction, where the V-shaped MR reversal is observed. For sample ♯5, a similar dumbbell shape is seen. However, for sample ♯7, the polar plot has an almost circular shape; the resistance is independent of the azimuthal angle ϕ. The absence of the azimuthal angle dependence of the MR is already reported for a dirty crystal of α-(BEDT-TTF)$_2$KHg(SCN)$_4$.[41]

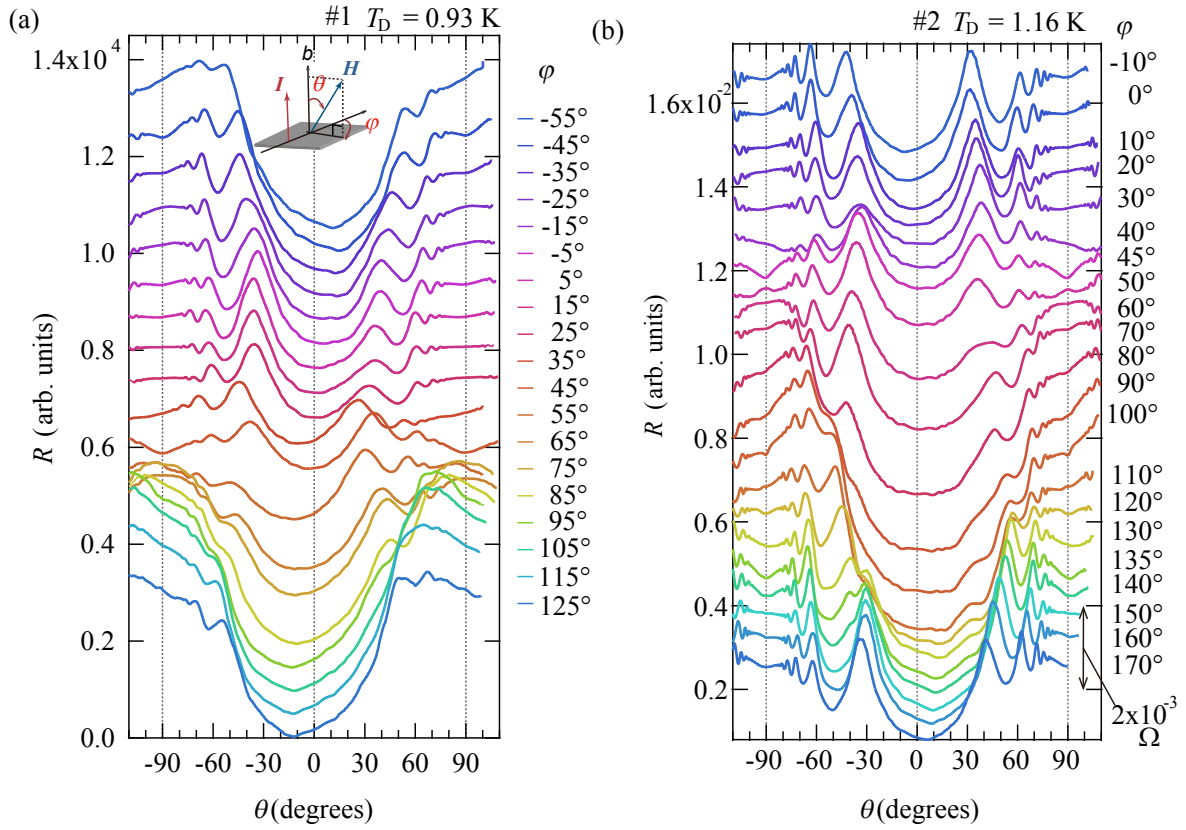

Figure 4.8: Angular dependences of the resistance at 14.5 T and 1.6 K for α-(BEDT-TTF)$_2$NH$_4$Hg(SCN)$_4$. The curves are shifted for clarity.

Figure 4.11(a) shows the resistance near $\theta = -90°$ for sample ♯2. A small peak in the MR at $\theta = \pm 90°$ is ascribed to the coherence peak.[35] The peak is evident in the second derivative curve $d^2R/d\theta^2$, [Fig. 4.11(b)], where we can define the peak width $\Delta\theta_{\rm peak} = 0.96°$. The coherence peak arises from the small closed orbits formed on the side of the corrugated Fermi surface and the geometrical analysis gives the peak width $\Delta\theta_{\rm peak} \approx 2k_F t_z c/E_F$.[35] Using $E_F = \hbar^2 k_F^2/2m_c \approx 26$ meV, we obtain the interlayer transfer integral $t_z \approx 0.078$ meV. This value will be reasonably consistent

with the inequality obtained from the analysis of the SdH oscillation, $t_z \leq 0.03$ meV because rather large ambiguity is included in these estimations. For κ-(BEDT-TTF)$_2$I$_3$, similar discrepancy between the two analyses is found; the absence of the node in the quantum oscillations shows $t_z \leq 0.016$ meV but the coherence peak width gives $t_z \approx 0.061$ meV.[28]

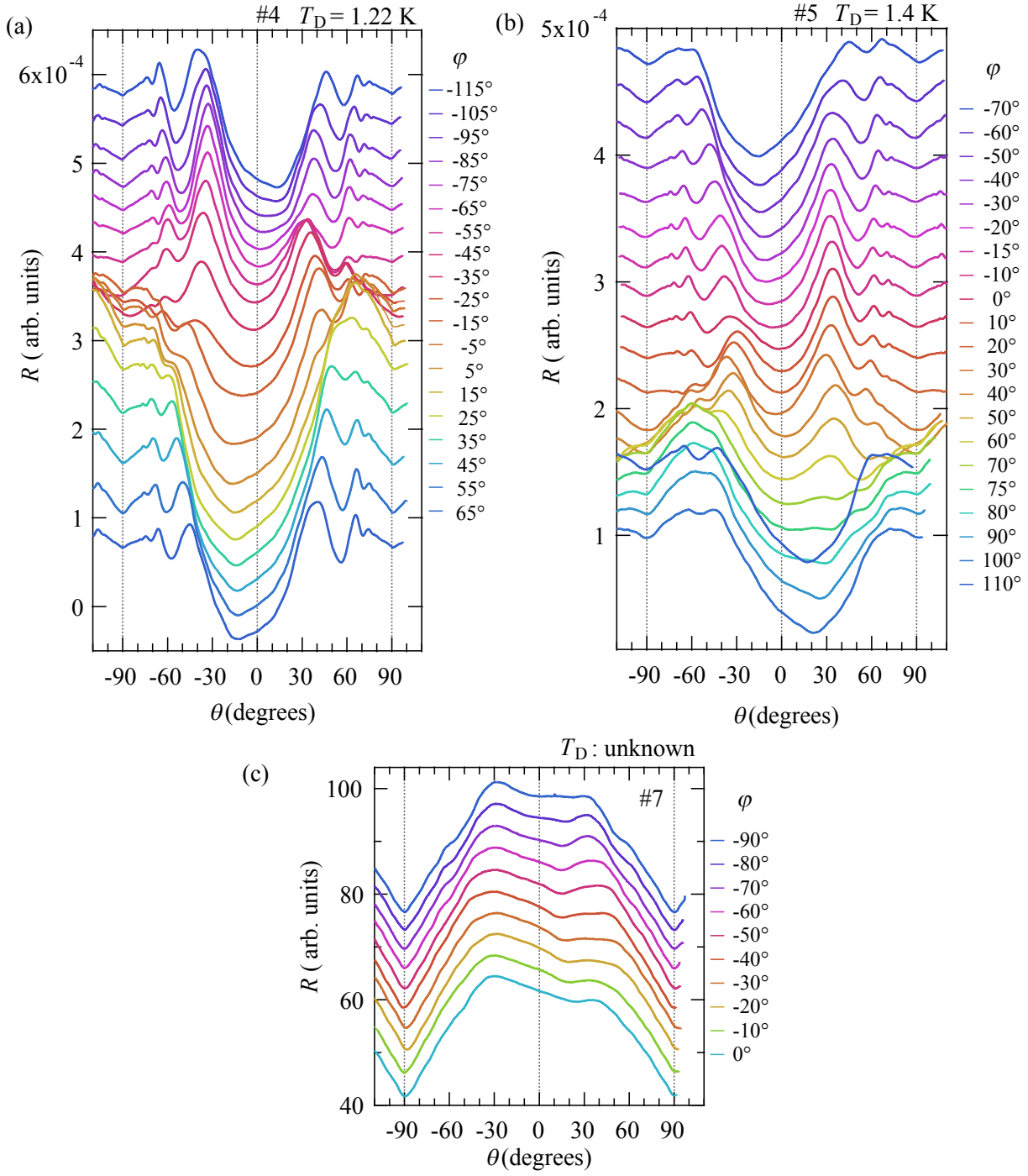

Figure 4.9: Angular dependences of the resistance at 14.5 T and 1.6 K for α-(BEDT-TTF)$_2$NH$_4$Hg(SCN)$_4$. The curves are shifted for clarity.

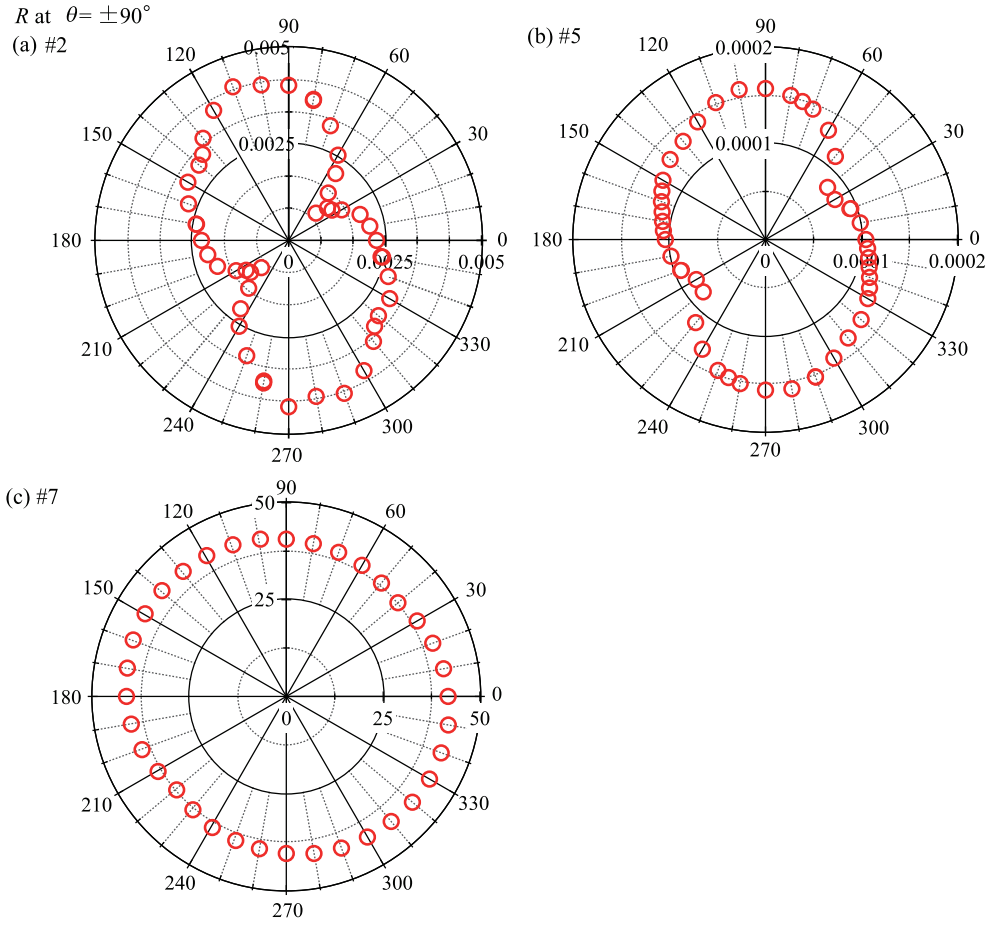

Figure 4.10: Polar plots of the interlayer resistances for $\theta = \pm 90°$ at 1.6 K and 14.5 T in samples (a) ♯2, (b) ♯5, and (c) ♯7.

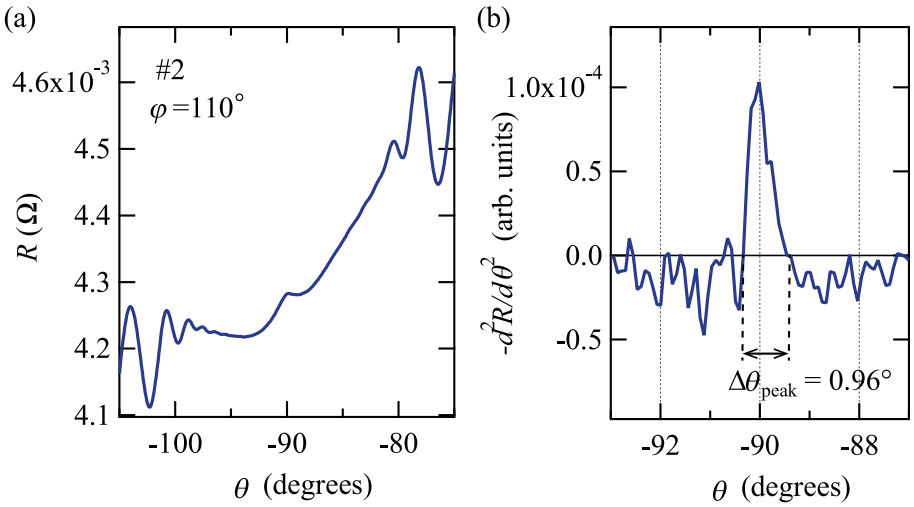

Figure 4.11: (a) Close-up of the resistance at 14.5 T, 1.6 K, and $\phi = 110°$ for sample ♯2. A coherence peak is seen at $\theta = -90°$ (b) The second derivative curve of the resistance, giving the peak width $\Delta\theta_{\text{peak}} = 0.96°$.

4.2 Discussion

4.2.1 Temperature dependence of resistivity

The temperature dependences of the interlayer resistivity show a broad hump around 120 K. Similar humps in the resistivity have been observed for various 2D superconducting materials such as Sr_2RuO_4,[101,102] $YBa_2Cu_3O_{6.87}$,[103] κ-(BEDT-TTF)$_2$Cu(CN)$_2$]Br,[104] κ-(BEDT-TTF)$_2$Cu(NCS)$_2$,[105] κ-(BEDT-TTF)$_2$FeBr$_4$,[106] and λ-(BEDT-TTF)$_2$FeCl$_4$.[107] A large number of the theoretical models have been proposed to explain the anomalous behavior in the interlayer resistivity.[102,108,109] Most of the theories suggest that the coherent band picture is not appropriate for the interlayer transport.

The temperature dependence of the interlayer resistivity has been systematically investigated for κ-(BEDT-TTF)$_2$Cu(NCS)$_2$ crystals, whose defects are controlled by the irradiation of X-rays or protons.[105] A broad resistivity hump is clearly observed around 100 K for a pure crystal. However, the resistivity decreases above $\sim$50 K and then the hump is suppressed for the irradiated (damaged) crystals. All the crystals have metallic temperature dependence at low temperatures. To explain these results, Analytis *et al.* assumed that the total interlayer conductivity is described by a formula,

$$\sigma_\perp(T,H) = \sigma_\perp^{\mathrm{B}}(T,H) + \sigma_\perp^{\mathrm{imp}}(T,H), \tag{4.2}$$

where $\sigma_\perp^{\mathrm{B}}$ is the interlayer band conductivity given by the Boltzmann transport, $\sigma_\perp^{\mathrm{B}} = (\rho_0 + \rho_{\mathrm{imp}} + \rho_{\mathrm{intrinsic}}(T))^{-1}$, ρ_0 is residual resistivity, ρ_{imp} is the contribution of the defect scattering to the resistivity, which is almost temperature-independent. $\rho_{\mathrm{intrinsic}}(T)$ is the intrinsic temperature-dependent scattering contribution, which gives metallic conductivity at low temperatures ($\rho_{\mathrm{intrinsic}}(T) \propto T^2$). $\sigma_\perp^{\mathrm{imp}}$ is the conductivity by the interlayer impurity channel, which is proportional to the density of impurities n_{imp}. The second term in Eq.(4.2) slightly decreases with temperature, so the temperature dependence of the interlayer resistivity $\rho_\perp = 1/\sigma_\perp$ may have a broad hump. After the irradiation, both ρ_{imp} and $\sigma_\perp^{\mathrm{imp}}$ increase, and the hump is consequently suppressed.

In α-(BEDT-TTF)$_2$NH$_4$Hg(SCN)$_4$, the high T_{D} samples (♯7-♯9) has the smaller resistances than the low T_{D} samples at the high temperatures and show the smaller humps. The behavior is consistent with the above model. In the low temperature limit, the total resistivity is given by $\rho_\perp = \rho_0 + \rho_{\mathrm{imp}}$. In the high temperature limit, the second term in Eq. (4.2) will be dominant, $\rho_\perp \approx 1/\sigma_\perp^{\mathrm{imp}}$. Therefore, we obtain RRR $\approx \left[(\rho_0 + \rho_{\mathrm{imp}})\sigma_\perp^{\mathrm{imp}}\right]^{-1}$, showing that the lower-quality sample has the lower RRR. This is consistent with the results of κ-(BEDT-TTF)$_2$Cu(NCS)$_2$. However, as shown in Fig. 4.12, we see that the RRR has a tendency to increase with T_{D} although the data points are rather scattered. This result seems inconsistent with the above model. For κ-(BEDT-TTF)$_2$Cu(NCS)$_2$, T_c is also reduced by the irradiation. However, we have not seen significant correlation between T_c and T_{D} for α-(BEDT-TTF)$_2$NH$_4$Hg(SCN)$_4$. The reasons of the discrepancies between the two salts are not clarified yet.

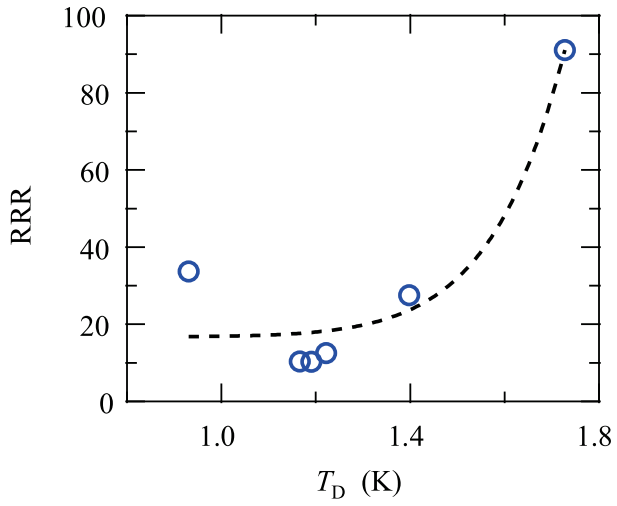

Figure 4.12: RRR vs. Dingle temperature plot. Dashed curve is a guide for the eye.

4.2.2 Incoherent interlayer transport

The V-shaped MR reversals at $\theta \approx 90°$ have been found for the relatively high T_D samples [see Figs. 4.5(d), 4.6, and 4.9(c)]. Figure 4.13(a) and (b) shows the interlayer resistance $\Delta R = R(\theta) - R(\theta = 90°)$ as a function of the perpendicular field component $H\cos\theta$ $(= H_\perp)$ above 7 T for samples ♯9 and ♯8, respectively. We note that the ΔR values are completely scaled by $H_\perp$ in all the angle regions for sample ♯9. A similar scaling is found in a limited angle region for sample ♯8. As presented in Fig. 4.13(c), ΔR exhibits a power law $\Delta R \propto (\mu_0 H_\perp)^p$. For these samples, we should note that the scaling is observed in the wide θ region at any ϕ angles; the incoherent behavior is independent of the field direction in the layer, irrespective of the anisotropic structure of the Fermi surfaces. The results show that the scattering effect plays a dominant role in the incoherent behavior for the relatively high T_D samples.

The similar scaling behavior has already been observed in the angular dependent MR of the 1D systems $(TMTSF)_2X$ (X = ClO_4, PF_6) with p =1.25[29,31] and a 2D system α-$(BEDT\text{-}TTF)_2KHg(SCN)_4$ (p is unknown).[41] The scaling for the 1D systems has been explained in terms of the confinement of the electron motion within the layer at the high parallel fields. For $(TMTSF)_2X$, as the parallel field along the b-axis increases, the amplitude of the sinusoidal motion shrinks in the interlayer direction, and then the electrons are confined in each layer; the electronic states are decoupled between the adjacent layers. Once the electronic states are decoupled by the parallel field, the interlayer MR does not depend on the parallel field: the MR should depend only on the perpendicular field. The decoupling field $H_{\rm decouple}$ is given by

$$\mu_0 H_{\rm decouple} \approx \frac{4t_z}{ev_F c}. \tag{4.3}$$

This equation gives $\mu_0 H_{\rm decouple} \approx 40$ T for $(TMTSF)_2PF_6$, but the experimental results exhibit $\mu_0 H_{\rm decouple} \approx 0.5$ T. As suggested by Strong *et al.*,[31] the interlayer decoupling can happen even for $H \ll H_{\rm decouple}$ due to electron correlation effect in the layer.

Since the decoupling is driven by the Lorentz force, the effect strongly depends on the direction of v_F of the electrons; the decoupling effect is maximum (minimum) when the field is perpendicular (parallel) to v_F. This is probably the reason why the decoupling effect has clearly been observed for the 1D systems, where the v_F vectors on the whole Fermi surface is almost aligned with the same direction. This is not the case for 2D systems, where the v_F vectors are distributed in all the directions in the layer. Therefore, the decoupling will depend on the field direction in the layer, reflecting the anisotropy of the 2D Fermi surface, as observed in the anisotropic 2D system (BEDT-TTF)$_2$Br(DIA).[40]

For sample ♯2, we can construct the anisotropic cross-section of the 2D Fermi surface from the periodicity of the AMRO [Fig. 4.8(b)] as shown in Fig. 4.14(b). The results are consistent with the previous studies.[60] The cross-section is slightly elliptical with the long axis in the $\theta = 40^\circ$ direction, which well agrees with the band calculation [Fig. 4.14(a)].[58]

The V-shaped MR background reversal around $\theta = \pm 90^\circ$ is observed at the directions indicated by red arrows in Fig. 4.14(b). These azimuthal angles correspond to the directions parallel to the flat parts of the 1D and 2D Fermi surfaces as shown by the dashed lines in Fig. 4.14(a). The v_F vectors on these flat parts are almost perpendicular to the field. Therefore, many electrons undergo the confinement effect by the parallel field in these directions. This is another evidence showing that the V-shaped MR background reversal around $\theta = \pm 90^\circ$ is caused by the confinement effect. We obtain similar behavior for three different samples with $T_\mathrm{D} \leq 1.19$ K. These results show that the confinement effect plays a dominant role in the incoherent behavior for the relatively low T_D samples. The coherence peak is observed only at $\phi \approx 110^\circ$ for sample ♯2. At present, it is not clear why the coherence peak appears only at $\phi \approx 110^\circ$.

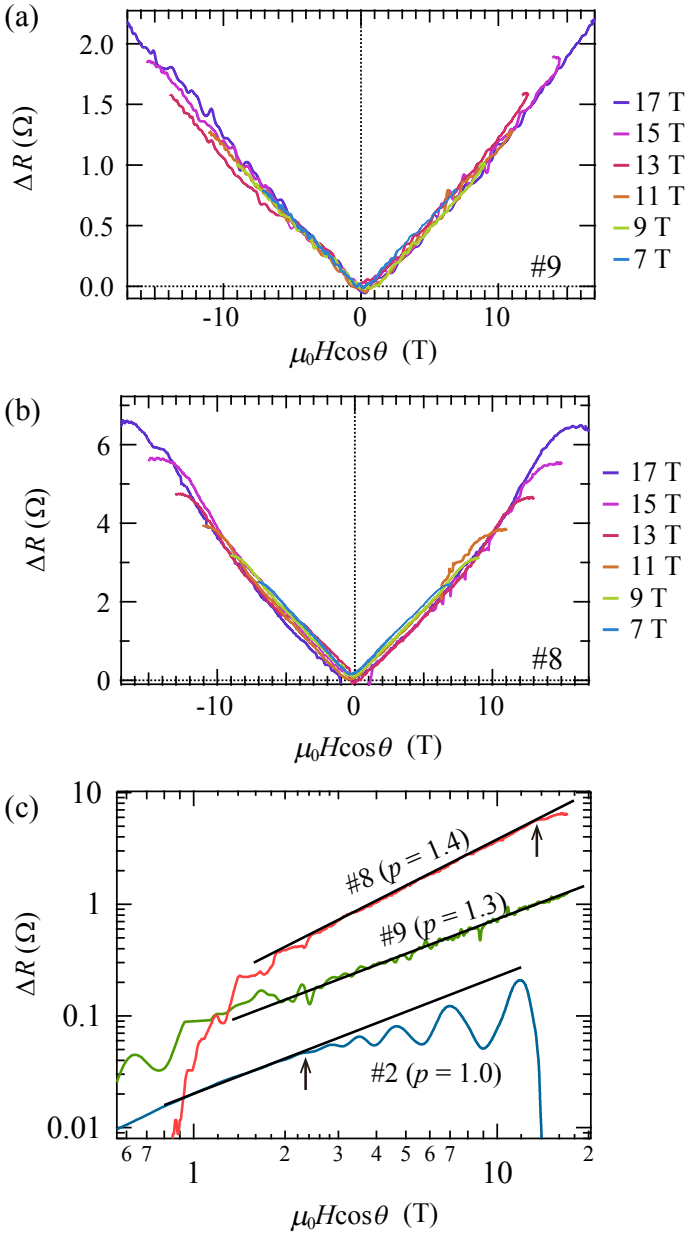

Figure 4.13: Interlayer resistance $\Delta R = R(\theta) - R(\theta = 90°)$ as a function of the perpendicular field component $\mu_0 H \cos\theta$ for samples (a)♯9 and (b)♯8. (c) Log-log plots of ΔR vs. $\mu_0 H \cos\theta$ for samples ♯2, ♯8, and ♯9. The curves are shifted for clarity. The solid lines denote the power law behavior $\Delta R \propto (\mu_0 H_\perp)^p$. At high perpendicular fields, ΔR deviates from the power law for samples ♯2 and ♯8, where the crossover field $\mu_0 H_\parallel^{\rm CO}$ is defined as indicated by the arrows.

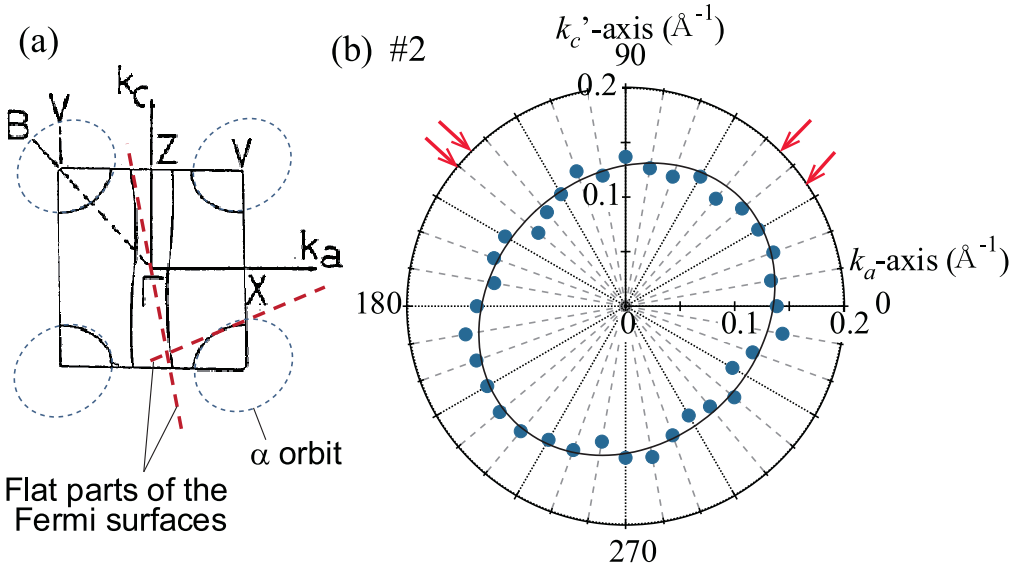

Figure 4.14: (a) Calculated Fermi surface of α-(BEDT-TTF)$_2$NH$_4$Hg(SCN)$_4$.[58] Dashed lines denote the flat parts of the 1D and 2D Fermi surfaces. (b) Cross section of the 2D Fermi surface obtained by the AMRO for sample ♯2. The MR background reversal is clearly observed at the angles denoted by red arrows.

4.2.3 Crossover

The experimental results are summarized in Fig. 4.15. We have obtained the two important results on the incoherent behavior (the V-shaped MR background reversal). 1) When $T_{\rm D}$ is relatively high (τ is relatively short), the interlayer transport is incoherent irrespective of the field direction. For sample ♯9, the MR background reversal is observed at fields down to 3 T [Fig. 4.6(b)], where the scaling $\Delta R \propto (\mu_0 H_\perp)^p$ behavior is evident even at $\theta = 0°$ ($\mu_0 H_\parallel = 0$ T). This fact clearly shows that the confinement effect by the parallel field is not required for the incoherent transport. Therefore, we can conclude that the scattering effect plays a dominant role in the incoherent behavior for the relatively high $T_{\rm D}$ samples. 2) When $T_{\rm D}$ is relatively low (τ is relatively long), the V-shaped MR background reversal becomes evident at $\phi \approx 45°$ and 135°, where the v_F vectors of the most electrons are perpendicular to the field (Fig. 4.8). The results apparently show that the confinement effect by the parallel field is required for the incoherent transport.

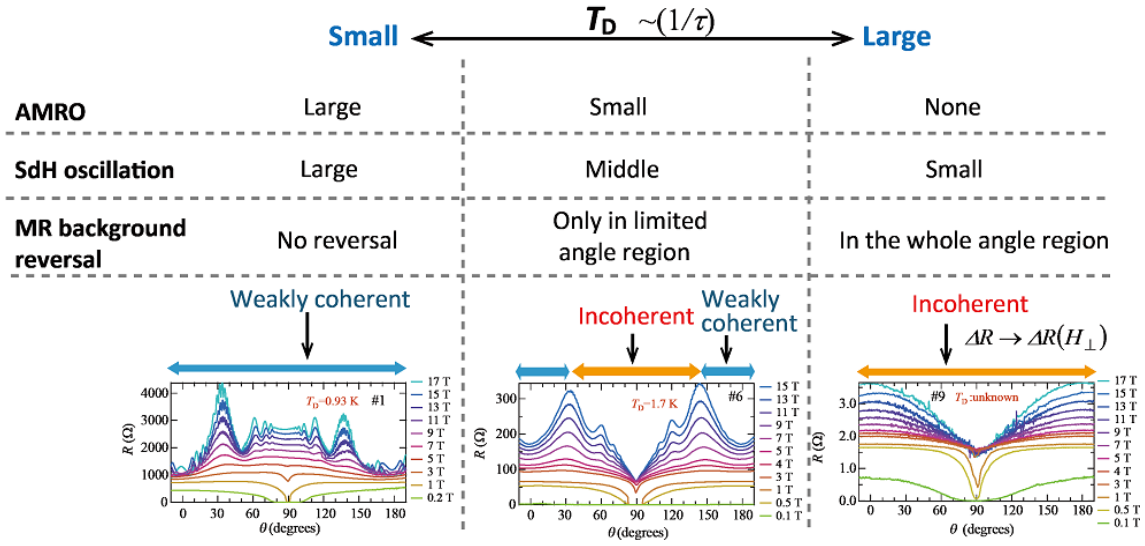

Figure 4.15: Summary of the experimental results.

Here, we can see the crossover from the weakly coherent to incoherent interlayer transport, characterized by the crossover parallel field $H_\parallel^{\rm CO}$. For the relatively high $T_{\rm D}$ samples, $H_\parallel^{\rm CO}$ should be quite low since the incoherent behavior is observed even for$\theta = 0°$ ($\mu_0 H_\parallel^{\rm CO} \approx 0$ T). For the relatively low $T_{\rm D}$ samples, the incoherent behavior depends on the field strength and azimuthal angle ϕ as well. For simplicity, we define $H_\parallel^{\rm CO}$ at $\phi \approx 45°$, where the incoherent behavior is the most evident. For instance, ΔR for sample ♯2 follows the power law $\Delta R \propto (\mu_0 H_\perp)^p$ up to $\theta = 80.4°$, but deviates from the law above it at 14.5 T [Fig. 4.13(c)]. Therefore, the crossover filed is estimated as $\mu_0 H_\parallel^{\rm CO} = 14.5 \cos(80.4°)$ = 14.3 T. Similarly, we can define $H_\parallel^{\rm CO}$ for samples ♯1-♯6 ($T_{\rm D} \leq 1.73$ K), which is plotted as a function of $T_{\rm D}$ as shown in Fig. 4.16. In the low $H_\parallel^{\rm CO}$ region, the interlayer transport is in the coherent regime.

In Fig. 4.16, we note $H_\parallel^{\rm CO} \approx 14$ T, independent of $T_{\rm D}$ in the low $T_{\rm D}$ region. When $T_{\rm D}$ is sufficiently low, it is reasonable that the confinement condition is determined only by the parameters of the electronic structure t_z and v_F in Eq. (4.3). Using $t_z \approx 0.078$ meV and $v_F = 6.3 \times 10^6$ cm/s

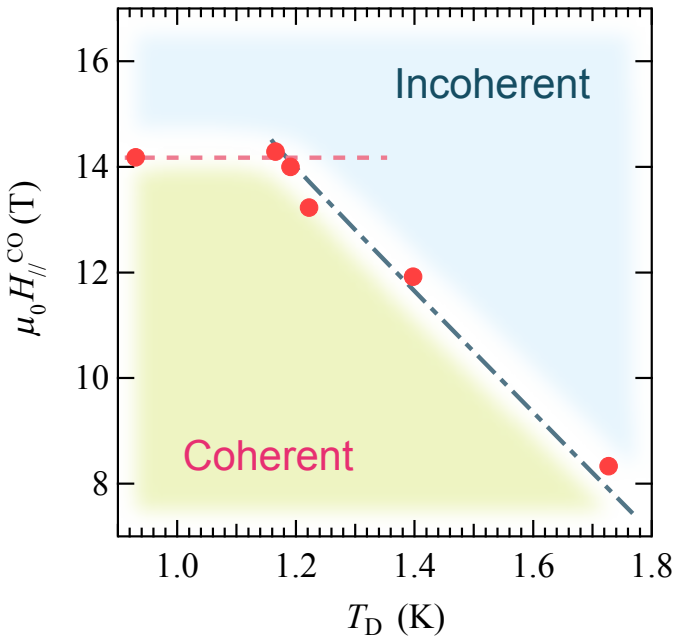

Figure 4.16: Crossover in-plane field vs. Dingle temperature plot. Dashed (red) and dot-dashed (blue) lines are guides for the eye.

from $v_F = k_F\hbar/m_c$, we obtain $\mu_0 H_{\rm decouple} \approx 2.4$ T. This value reasonably agrees with $\mu_0 H_{\parallel}^{\rm CO} \approx 14$ T since $\mu_0 H_{\rm decouple}$ gives the lower limit of the crossover. We could expect that $H_{\parallel}^{\rm CO}$ is constant even in the limit of $T_{\rm D} \to 0$ K. On the other hand, as $T_{\rm D}$ increases above ~1.2 K, $H_{\parallel}^{\rm CO}$ decreases almost linearly. If $T_{\rm D}$ further increases, we expect that $H_{\parallel}^{\rm CO}$ decreases down to zero. Actually, for sample ♯9, we see the MR background reversal is observed in the whole angle region, suggesting $\mu_0 H_{\parallel}^{\rm CO} \approx 0$ T.

The above results will be interpreted according to the two-conducting-channel model given by Eq. (4.2). The model was first applied to the incoherent behavior in high fields for α-(BEDT-TTF)$_2$KHg(SCN)$_4$ by Kartsovnik *et al.*[110] In this model, it is assumed that the band (coherent) conductivity term $\sigma_{\perp}^{\rm B}$ gives the conventional AMRO but the impurity-channel term $\sigma_{\perp}^{\rm imp}$ shows the MR background reversal, following the power law. For α-(BEDT-TTF)$_2$NH$_4$Hg(SCN)$_4$, the conductivity should be dominated by the band conductivity term $\sigma_{\perp}^{\rm B}$ in the low $T_{\rm D}$ limit since the conventional MR behavior is observed as shown in Fig. 4.5(a). In this case, the incoherent behavior will be induced by the confinement effect, whose crossover field $\mu_0 H_{\parallel}^{\rm CO}$ is determined by t_z and v_F in Eq. (4.3). As long as the $\sigma_{\perp}^{\rm B}$ term is dominant, $H_{\parallel}^{\rm CO}$ will be independent of $T_{\rm D}$, which is consistent with the result for $T_{\rm D} < 1.2$ K (Fig. 4.16). In the high $T_{\rm D}$ limit, the conductivity will be dominated by the impurity-channel term $\sigma_{\perp}^{\rm imp}$. Therefore, we will observe the power law behavior, the MR reversal background as shown in Fig. 4.6(b). In this limit, we will obtain $\mu_0 H_{\parallel}^{\rm CO} \approx 0$ T.

Based on the above model, we simulated the angular dependence of the interlayer resistance $\rho_\perp$ as shown in Fig. 4.17. The $\sigma_\perp^{\rm B}$ is calculated with the same parameters shown in Fig. 4.7(a), and $\sigma_{zz}^0 = 1$ and $\sigma_\perp^{\rm imp} = [\rho_1 + \rho_2(\mu_0 H_\perp)^p]^{-1}$, where $\rho_1 = 0.2$, $\rho_2 = 0.4$, and $p = 1.25$. For comparison, the $1/\sigma_\perp^{\rm B}$ and $1/\sigma_\perp^{\rm imp}$ terms at 15 T are indicated by the dotted and dashed curves, respectively. We note that the overall behavior of the total resistance $1/(\sigma_\perp^{\rm B} + \sigma_\perp^{\rm imp})$ is quite similar to the data in Fig. 4.5(d). In this simulation, the $\sigma_\perp^{\rm imp}$ term is dominant around $\theta = 90°$. Therefore, the V-shaped MR behavior is evident for $38° \leq \theta \leq 142°$. The crossover field $\mu_0 H_\parallel^{\rm CO}$ will be defined at $\theta \approx 38°$ and 142°. As the field is further tilted, the $\sigma_\perp^{\rm B}$ contribution becomes dominant so we observe the conventional AMRO around $\theta = 0°$ and 180°. If the $T_{\rm D}$ of the sample is lower ($\sigma_\perp^{\rm B}$ contribution is larger), we will see the V-shaped MR behavior in a narrower angle region; the crossover field will increase. In this way, the increase of $\mu_0 H_\parallel^{\rm CO}$ with decreasing $T_{\rm D}$ in Fig. 4.16 is qualitatively interpreted by the two-conducting-channel model.

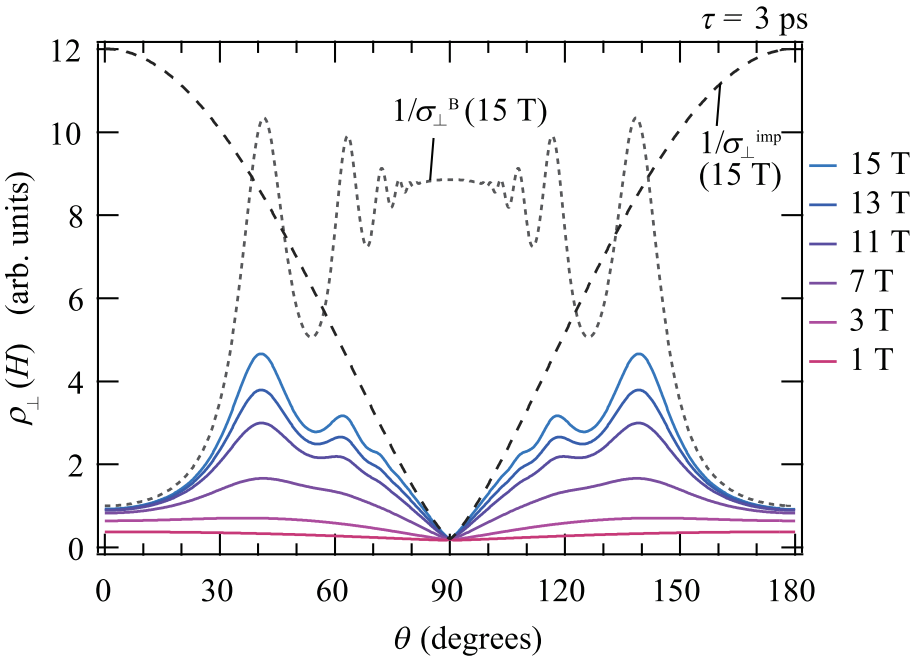

Figure 4.17: Angular dependence of simulated total interlayer resistance $\rho_\perp = 1/(\sigma_\perp^{\rm B} + \sigma_\perp^{\rm imp})$. The $1/\sigma_\perp^{\rm B}$ and $1/\sigma_\perp^{\rm imp}$ terms at 15 T are indicated by the dotted and dashed curves, respectively. In this simulation, we take $k_F = 1.35$ nm^{-1} and $\tau = 3$ ps for $\sigma_\perp^{\rm B}$, and $\rho_1 = 0.2$, $\rho_2 = 0.4$, and $p = 1.25$ for $\sigma_\perp^{\rm imp}$. See the text in detail.

Chapter 5

Conclusions

(1) Conductivity and magnetism in π-d organic conductors κ-(BDH-TTP)$_2$FeX$_4$ (X = Br, Cl)

The physical properties of the 2D π-d systems κ-(BDH-TTP)$_2$FeX$_4$ (X = Br, Cl) have been measured to investigate the electronic state. Both salts exhibit metallic conductivity down to 30 mK.

For the $FeBr_4$ salt, the localized Fe $3d$ spins with $S = 5/2$ have the AF transition at 3.9 K with the magnetic easy axis along the a-axis while the π electrons show metallic conductivity down to 30 mK. The canted AF spin structure is proposed, causing the WF transitions for $H \parallel b$ and $H \parallel c$. The dominant mechanisms of the spin canting are the spin frustration and anisotropic crystal field effects. The ESR signal is observed in the wide temperature range down to 20 K. Above 120 K, the ESR lineshape is Lorentzian, showing the strong exchange narrowing. Below 50 K, ESR linewidth shows the critical phenomenon toward the AF order, which is associated with the deviation of the magnetic susceptibility from the Curie-Weiss behavior. The angular dependence of the ESR linewidth at low temperatures suggests that the critical broadening of the linewidth is significantly enhanced by the spin fluctuation in addition to the effect of the low dimensionality. From the anisotropy of the susceptibility above T_N, the CF parameters ($D = -0.38$ K, $E = 0.038$ K) are estimated. The evidence of the strong π-d interaction is obtained by the magnetoresistance measurements, where the magnetic potential created by the $3d$ spins plays an essential role.

For the $FeCl_4$ salt, the magnetic susceptibility, arising mainly from the localized $3d$ spins of the Fe ions, obeys the Curie Weiss law down to 2 K with a small Weiss temperature of $\sim$-0.2 K. The magnetic torque measurements demonstrate that the $3d$ spins ($S = 5/2$) show the AF order at $\sim$0.4 K, with the easy axis parallel to the a-axis, and that the metamagnetic transition takes place at $\sim$0.15 T for $H \parallel a$. A simple two-spin sublattices model is found to well reproduce the essential features of the torque data in the AF states. The metamagnetic transition is associated with a sharp drop of the interlayer resistance at low temperatures. Such behavior is explained in terms of the simple model of the quantum tunneling between the layers, and provides strong evidence of the finite π-d interaction for the $FeCl_4$ salt. χT and the g-value have characteristic temperature dependences below 50 K. The χT behavior is well explained by the single-ion anisotropy model, and the numerical fitting gives the anisotropy parameters $D = -0.1$ K and $E = +0.042$ K. The linear correlation between χT and g^2 suggests that the temperature dependences of both χT and the g-value have the same origin. The ESR signal has the Lorentzian lineshape, showing the exchange narrowing. The ESR linewidth

is simulated by the simple model including both the crystal field and dipole interaction effects with the exchange interaction $J \approx 0.2$ K. This J value is high compared with $J_d \approx 0.07$ K obtained from the relation $k_{\rm B}T_{\rm N}^{\rm exp} \approx (2/3)|J_d|S(S+1)$ for $T_{\rm N} = 0.4$ K.

(2) Incoherent interlayer charge transport in α-(BEDT-TTF)$_2$NH$_4$Hg(SCN)$_4$

The interlayer transport of an organic superconductor α-(BEDT-TTF)$_2$NH$_4$Hg(SCN)$_4$ has been investigated for many samples with various qualities. For the samples with $T_{\rm D} < 1.2$ K, the incoherent interlayer transport, the MR background reversal, is found to be induced by the confinement effect due to the parallel field. The crossover field $\mu_0 H_{\parallel}^{\rm CO}$ from the weakly coherent to incoherent interlayer transport is estimated as about 14 T. The $\mu_0 H_{\parallel}^{\rm CO}$ value, which is independent of $T_{\rm D}$, is determined by the band parameters, t_z and v_F. For the higher $T_{\rm D}$ samples, $\mu_0 H_{\parallel}^{\rm CO}$ decreases with increasing $T_{\rm D}$. These results are interpreted on the assumption of two conducting channels, the band coherent and impurity-assisted incoherent channels in the interlayer transport. The band coherent channel $\sigma_{\perp}^{\rm B}$ gives the conventional MR behavior, but the electrons undergo the confinement effect by the parallel field. The impurity-assisted incoherent channel gives the V-shaped MR, characterized by the power law behavior $\Delta R \propto (\mu_0 H_{\perp})^p$. When $T_{\rm D} > 1.2$ K (the impurity concentration is sufficiently large), the $\sigma_{\perp}^{\rm imp}$ term becomes relatively large especially in the field parallel to the layer, which leads to the V-shaped MR. In the high $T_{\rm D}$ limit, the $\sigma_{\perp}^{\rm imp}$ term is dominant; the power law MR is observed in the whole angle and field region.

References

[1] H. Akamatu, H. Inokuchi, and Y. Matsunaga, Nature **173**, 168 (1954).

[2] H. Shirakawa, E. J. Louis, A. G. MacDiarmid, C. K. Chiang, and A. J. Heeger, J. Chem. Soc. Chem. Commun. 578 (1977).

[3] J. Ferraris, D. O. Cowan, V. Walatka, and J. H. Perlstein, J. Am. Chem. Soc. **95**, 948 (1973).

[4] H. Kobayashi, Mol. Sci. **1**, A0009 (2007) (Japanese).

[5] D. Jérome, A. Mazaud, M. Ribault, and K. Bechgaad, J. Physique Lett. **41**, L95 (1980).

[6] G. Saito, T. Enoki, K. Toriumi, and H. Inokuchi, Solid. State. Commun. **42**, 557 (1982).

[7] H. Urayama, H. Yamochi, G. Saito, K. Nozawa, T. Sugano, M. Kinoshita, S. Sato, K. Oshima, A. Kawamoto, and J. Tanaka, Chem. Lett. 55 (1988).

[8] H. Tanaka, Y. Okano, H. Kobayashi, W. Suzuki, and A. Kobayashi, Science **291**, 285 (2001).

[9] K. Miyagawa, K. Kanoda, and A. Kawamoto, Chem. Rev. **104**, 5635 (2004).

[10] N. Thorup, G. Rindorf, H. Soling, and K. Bechgaard, Acta Cryst. **B37**, 1236 (1981).

[11] M. Tamura, K. Yakushi, H. Kuroda, A. Kobayashi, R. Kato, and H. Kobayashi, Chem. Lett. **15**, 89 (1986).

[12] H. Kobayashi, R. Kato, A. Kobayashi, G. Saito, M. Tokumoto, H. Anzai, and T. Ishiguro, Chem. Rev. **104**, 5005 (2004).

[13] K. Oshima, T. Mori, H. Inokuchi, H. Urayama, H. Yamochi, and G. Saito, Phys. Rev. B **38**, 938 (1988).

[14] L. Ducasse and A. Fritsch, Solid State Commun. **91**, 201 (1994).

[15] P. Foury-Leylekian, J. -P. Pouget, Y. -J. Lee, R. M. Nieminen, P. Ordejon, and E. Canadell, Phys. Rev. B **82**, 134116 (2010).

[16] E. Coronado and P. Day, Chem. Rev. **104**, 5419 (2004).

[17] T. Enoki and A. Miyazaki, Chem. Rev. **104**, 5449 (2004).

[18] L. Ouahab and T. Enoki, Eur. J. Inorg. Chem. 933 (2004).

[19] H. Kobayashi and H. Bo Cui, Chem. Rev. **104**, 5265 (2004).

[20] T. Inabe and H. Tajima, Chem. Rev. **104**, 5503 (2004).

[21] T. Sugimoto, H. Fujiwara, S. Noguchi, and K. Murata, Sci. Technol. Adv. Mater. **10**, 024302 (2009).

[22] S. Uji, H. Shinagawa, T. Terashima, T. Yakabe, Y. Terai, M. Tokumoto, A. Kobayashi, H. Tanaka, and H. Kobayashi, Nature **410**, 908 (2001).

[23] M. Kimata, Y. Takahide, A. Harada, H. Satsukawa, K. Hazama, T. Terashima, S. Uji, T. Naito, and T. Inabe, Phys. Rev. B **80**, 085110 (2009).

[24] N. Hanasaki, M. Matsuda, H. Tajima, E. Ohmichi, T. Osada, T. Naito and T. Inabe, J. Phys. Soc. Jpn. **75**, 033703 (2006).

[25] H. Akiba, S. Nakano, Y. Nishio, K. Kajita, B. Zhou, A. Kobayashi, and H. Kobayashi, J. Phys. Soc. Jpn. **78**, 033601 (2009).

[26] M. M. Matsushita, H. Kawakami, and T. Sugawara, Phys. Rev. B. **77**, 195208 (2008).

[27] R. H. McKenzie and P. Moses, Phys. Rev. Lett. **81**, 4492 (1998).

[28] J. Wosnitza, J. Hagel, J. S. Qualls, J. S. Brooks, E. Balthes, D. Schweizer, J. A. Schluter, U. Geiser, J. Mohtasham, R. W. Winter, and G. L. Gard, Phys. Rev. B **65**, R180506 (2002).

[29] D. G. Clarke, S. P. Strong, P. M. Chaikin, and E. I. Chashechkina, Science **279**, 2071 (1998).

[30] E. I. Chashechkina and P. M. Chaikin, Phys. Rev. Lett. **80**, 2181 (1998).

[31] S. P. Strong, D. G. Clarke, and P. W. Anderson, Phys.Rev. Lett. **73**, 1007 (1994).

[32] W. Kang, T. Osada, Y. J. Jo, and Haeyong Kang, Phys. Rev. Lett. **99**, 017002 (2007).

[33] W. Kang, Phys. Rev. B **76**, 193103 (2007).

[34] J. Singleton, P. A. Goddard, A. Ardavan, N. Harrison, S. J. Blundell, J. A. Schulueter, and A. M. Kini, Phys. Rev. Lett., **88**, 037001 (2002).

[35] N. Hanasaki, S. Kagoshima, T. Hasegawa, T. Osada, and N. Miura, Phys. Rev. B 57, 1336 (1998).

[36] K. Yamaji, J. Phys. Soc. Jpn. **58**,1520 (1989).

[37] R. Yagi, Y. Iye, T. Osada, and S. Kagoshima, J. Phys. Soc. Jpn. **59**, 3069 (1990).

[38] M. Kuraguchi, E. Ohmichi, T. Osada, and Y. Shiraki, Synth. Met. **133-134**, 133 (2003).

[39] T. Kawamoto, T. Mori, D. Graf, J. S. Brooks, T. Shirahata, and T. Imakubo, J. Phys. Soc. Jpn., 83, 15002 (2014).

[40] S. Uji, T. Terashima, S. Yasuzuka, J. Yamaura, H. M. Yamamoto, and R. Kato, Phys. Rev. B **68**, 064420 (2003).

[41] M. V. Kartsovnik, D. Andres, S. V. Simonov, W. Biberacher, I. Sheikin, N. D. Kushch, and H. Muller, Phys. Rev. Lett. **96**, 166601 (2006).

[42] T. Otsuka, H Cui, H. Fujiwara, H. Kobayashi, E. Fujiwara, and A. Kobayashi, J. Mater. Chem. **14**, 1682 (2004).

[43] H. Fujiwara, E. Fujiwara, Y. Nakazawa, B. Z. Narymbetov, K. Kato, H. Kobayashi, A. Kobayashi, M. Tokumoto, and P. Cassoux, J. Am. Chem. Soc. **123**, 306 (2001).

[44] S. Uji, T. Terashima, C. Terakura, T. Yakabe, Y. Terai, S. Yasuzuka, Y. Imanaka, M. Tokumoto, A. Kobayashi, F. Sakai, H. Tanaka, H. Kobayashi, L. Balicas, and J. S. Brooks, J. Phys. Soc. Jpn. **72**, 369 (2003).

[45] H. Fujiwara, K. Wada, T. Hiraoka, T. Hayashi, T. Sugimoto, H. Nakazumi, K. Yokogawa, M. Teramura, S. Yasuzuka, K. Murata, T. Mori, J. Am. Chem. Soc. **127**, 14166 (2005).

[46] X. Xiao, T. Hayashi, H. Fujiwara, T. Sugimoto, S. Noguchi, Y. Weng, H. Yoshino, K. Murata, and H. Aruga Katori, J. Am. Chem. Soc. **109**, 12618 (2007).

[47] T. Hayashi, X. Xiao, H. Fujiwara, T. Sugimoto, H. Nakazumi, S. Noguchi, T. Fujimoto, S. Yasuzuka, H. Yoshino, K. Murata, T. Mori, and H. Aruga-Katori, J. Am. Chem. Soc. **128**, 11746 (2006).

[48] H. Fujiwara, T. Hayashi, T. Sugimoto, H. Nakazumi, S. Noguchi, L. Li, K. Yokogawa, S. Yasuzuka, K. Murata, and T. Mori, Inorg. Chem. **45**, 5712 (2006).

[49] Y. Weng, H. Yoshino, H. Fujiwara, T. Sugimoto, and K. Murata, Solid State Sci. **45**, 5712 (2006).

[50] T. Konoike, S. Uji, T. Terashima, M. Nishimura, S. Yasuzuka, K. Enomoto, H. Fujiwara, B. Zhang, and H. Kobayashi, Phys. Rev. B **70**, 094514 (2004).

[51] J. Yamada, H. Akutsu, H. Nishikawa, and K. Kikuchi, Chem. Rev. **104**, 5057 (2004).

[52] E. S. Choi, D. Graf, J. S. Brooks, J. Yamada, H. Akutsu, K. Kikuchi, and M. Tokumoto, Phys. Rev. B **70**, 024517 (2004).

[53] K. Kikuchi, H. Nishikawa, I. Ikemoto, H. Toita, H. Akutsu, J. Nakatsuji, and J. Yamada, J. Solid State Chem. **168**, 503 (2002).

[54] K. Kanoda, Physica C **282**, 299 (1997).

[55] T. Komatsu, N. Matsukawa, T. Inoue, and G. Saito, J. Phys. Soc. Jpn. **65**, 1340 (1996).

[56] T. Mori and M. Katsuhara, J. Phys. Soc. Jpn. **71**, 826 (2002).

[57] T. Mori, M. Katsuhara, H. Akutsu, K. Kikuchi, J. Yamada, H. Fujiwara, T. Matsumoto, and T. Sugimoto, Polyhedron **24**, (2005) 2315.

[58] H. Mori, S. Tanaka, M. Oshima, G. Saito, T. Mori, Y. Maruyama, and H. Inokuchi, Bull. Chem. Soc. Jpn. **63**, 2183 (1990).

[59] S. Uji, T. Terashima, H. Aoki, J. S. Brooks, M. Tokumoto, N. Kinoshita, T. Kinoshita, Y. Tanaka, and H. Anzai, Phys. Rev. B **54**, 9332 (1996).

[60] N. Hanasaki, S. Kagoshima, N. Miura, and G. Saito, Phys. Rev. B **63**, 245116 (2001).

[61] D. Shoenberg “Magnetic oscillations in metals” Cambridge University Press (1984).

[62] K. Kajita, Y. Nishio, T. Takahashi, W. Sasaki, R. Kato, H. Kobayashi, A. Kobayashi, and Y. Iye, Solid State Commun. **70**, 1189 (1989).

[63] R. Kubo and K. Tomita, J. Phys. Soc. Jpn. **9**, 888 (1954).

[64] T. Sasaki, H. Uozaki, S. Endo, and N. Toyota, Synth. Met. **120**, 759 (2001).

[65] E. Ohmichi and T. Osada, Rev. Sci. Instrum. **73**, 3022 (2002).

[66] T. Konoike, S. Uji, M. Nishimura, K. Enomoto, H. Fujiwara, B. Zhang, and H. Kobayashi, Physica B **359-361**, 457 (2005).

[67] H. Tajima, G. Yoshida, M. Matsuda, J. Yamaura, N. Hanasaki, T. Naito, and T. Inabe, Phys. Rev. B **80**, 024424 (2009).

[68] M. Tokumoto, H. Tanaka, T. Otsuka, H. Kobayashi, and A. Kobayashi, Polyhedron **24**, 2793 (2005).

[69] M. Maesato, Y. Furushima, G. Saito, H. Kitagawa, T. Imakubo, A. Kiswandhi, D. Graf, and J. S. Brooks, J. Phys. Soc. Jpn. **82**, 043704 (2013).

[70] M. Kimata, H. Satsukawa, Y. Takahide, T. Terashima, S. Uji, M. Matsuda, H. Tajima, T. Naito, and T. Inabe, J. Low Temp. Phys. **159**, 272 (2010).

[71] O. M. Vyaselev, M. V. Kartsovnik, W. Biberacher, L. V. Zorina, N. D. Kushch, and E. B. Yagubskii, Phys. Rev. B **83**, 094425 (2011).

[72] J. I. Oh, M. J. Naughton, T. Courcet, I. Malfant, P. Cassoux, M. Tokumoto, H. Akutsu, H. Kobayashi, and A. Kobayashi, Synth. Met. **103**, 1861 (1999).

[73] H. Uozaki, T. Sasaki, S. Endo, and N. Toyota, J. Phys. Soc. Jpn. **69**, 2759 (2000).

[74] J. Yamada, H. Akutsu, H. Nishikawa, and K. Kikuchi, Chem. Rev. **104**, 5057 (2004).

[75] T. Thio, T. R. Thurston, N. W. Preyer, P. J. Picone, M. A. Kastner, H. P. Jenssen, D. R. Gabbe, C. Y. Chen, R. J. Birgeneau, and A. Aharony, Phys. Rev. B **38**, 905 (1988).

[76] J. M. Tarascon, P. F. Miceli, P. Barboux, D. M. Hwang, G. W. Hull, M. Giroud, L. H. Greene, Yvon LePage, W. R. McKinnon, E. Tselepis G. Pleizier, M. Eibschutz, D. A. Neumann , and J. J. Rhyne, Phys. Rev. B **39**, 11587 (1989).

[77] K. Murata, M. M. Ishibashi, Y. Honda, N. A. Fortune, M. Tokumoto, N. Kinoshita, and H. Anzai, Solid State Commun. **76**, 377 (1990).

[78] I. D. Parker, R. H. Friend, M. Kurmoo, P. Day, C. Lenoir, and P. Batail, Synth. J. Phys., Condens. Matter **1**, 4479 (1989).

[79] H. Hasegawa, Phys. Lett. **41A**, 39 (1972).

[80] H, Yamada and S. Takada, J. Phys. Soc. Jpn. **34**, 51 (1973).

[81] I. Yamamoto and K. Nagata, J. Phys. Soc. Jpn. **43**, 1581 (1977).

[82] J. Nishijo, A. Miyazaki, and T. Enoki, Bull. Chem. Soc. Jpn. **77**, 715 (2004).

[83] A. Miyazaki, H. Yamazaki, M. Aimatsu, T. Enoki, R. Watanabe, E. Ogura, Y. Kuwatani, and M. Iyoda, Inorg. Chem. **46**, 3353 (2007).

[84] S. Kudo, A. Miyazaki, T. Enoki, S. Golhen, L. Ouahab, T. Toita, and J. Yamada, Inorg. Chem. **45**, 3718 (2006).

[85] I. Dzyaloshinskii, J. Phys. Chem. Solids **4**, 241 (1958).

[86] T. Moriya, Phys. Rev. **120**, 91 (1960).

[87] T. Mori, H. Mori, and S. Tanaka, Bull. Chem. Soc. Jpn. **72**, 179 (1999).

[88] K. Takahara, S. Hao, H. Tanaka, T. Kadono, M. Hara, K. Takai, and T. Enoki, Phys. Rev. B **82**, 121417 (2010).

[89] R. M. Richards and M. B. Salamon, Phys. Rev. B **9**, 32 (1974).

[90] M. J. Hennessy and C. D. McElwee, Phys. Rev. B **7**, 930 (1973).

[91] A. Bencini and D. Gattechi, " EPR of Exchange Coupled Systems " (Springer-Verlag, Berlin, 1990).

[92] H. Tanaka, K. Ito, and K. Nagata, J. Phys. Soc. Jpn. **54**, 4345 (1985).

[93] J. Deisenhofer, M. V. Eremen, D. V. Zakharov, V. A. Ivanshin, R. M. Eremina, H, A. Krug von Nidda, A. A. Mukhin, A. M. Balbashov, and A. Loidl, Phys. Rev. B **65**, 10440 (2002).

[94] T. Fujimoto, S. Yasuzuka, K. Yokogawa, H. Yoshino, T. Hayashi, H. Fujiwara, T. Sugimoto, and K. Murata, J. Phys. Soc. Jpn. **77**, 014704 (2008).

[95] S. Uji, H. Shinagawa, Y. Terai, T. Yakabe, C. Terakura, T. Terashima, L. Balicas, J. S. Brooks, E. Ojima, H. Fujiwara, H. Kobayashi, A. Kobayashi, and M. Tokumoto, Physica B **298**, 557 (2001).

[96] J. Inoue and S. Maekawa, Phys. Rev. B **53**, R11927 (1996).

[97] Y. Taguchi and Y. Tokura, Phys. Rev. B **60**, 10280 (1999).

[98] P. Majumdar and P. B. Littlewood, Nature **395**, 479 (1998).

[99] M. Gerloch, J. Lewis, and R. C. Slade, J. Chem. Soc. A 1422 (1969).

[100] M. V. Kartsovnik, Chem. Rev. **104**, 5737 (2004).

[101] N. E. Hussey, A. P. Mackenzie, J. R. Cooper, Y. Maeno, S. Nishizaki, and T. Fujita, Phys. Rev. B **57**, 5505 (1998).

[102] D. B. Gutman and D. L. Maslov, Phys. Rev. Lett. **99**, 196602 (2007).

[103] T. Ito, H. Takagi, S. Ishibashi, T. Ido, and S. Uchida, Nature **350**, 596 (1991).

[104] Ch. Strack, C. Akinci, V. Pashchenko, B. Wolf, E. Uhring, W. Assmus, M. Lang, J. Schreuer, L. Wiehl, J. A. Schlueter, J. Wosnitza, D. Schweitzer, J. Muller, and J. Wykhoff, Phys. Rev. B **72**, 054511 (2005).

[105] J. G. Analytis, A. Ardavan, S. J. Blundell, R. L. Owen, E. F. Garman, C. Jeynes, and B. J. Powell, Phys. Rev. Lett. **96**, 177002 (2006).

[106] H. Kobayashi, H. Tomita, T. Naito, A. Kobayashi, F. Sakai, T. Watanabe, and P. Cassoux, J. Am. Chem. Soc. **118**, 368 (1996).

[107] A. Kobayashi, T. Udagawa, H. Tomita, T. Naito, and H. Kobayashi, Chem. Lett. **22**, 2179 (1993).

[108] A. G. Rojo and K. Levin, Phys. Rev. B **48**, 16861 (1993).

[109] A. F. Ho and A. J. Schofield, Phys. Rev. B **71**, 045101 (2005).

[110] M. V. Kartsovnik, P. D. Grigoriev, W. Biberacher, and N. D. Kushch, Phys. Rev. B **79**, 165120 (2009).

Acknowledgments

Special thanks are due to my thesis supervisor Professor Shinya Uji (Unit Director, Superconducting Properties Unit, NIMS) for his invaluable support and guidance through the moments of graduate school.

I am also grateful to my dissertation committee: Professor Kazuaki Sakoda (Unit Director, Photonic Materials Unit, NIMS), Professor Xiao Hu (Unit Director, Nano-System Theoretical Physics Unit, NIMS), and Associate Professor Akinobu Kanda (Institute of Physics, University of Tsukuba) for many valuable comments and suggestions to improve this thesis.

I would like to express my gratitude to Professor Enoki Toshiaki (Tokyo Institute of Technology) and Assistant Professor Kazuyuki Takai (his present post is Associate Professor in Hosei University) for their suggestive discussions that make my research of great achievement.

I would like to express my gratitude to Associate Professor Jun-ichi Yamada (University of Hyogo) for providing me high quality samples, valuable discussions, and encouragement throughout my doctoral course. The author also would like to thank to Assistant Professor Hiroki Akutsu (University of Hyogo), Dr. Shun Ichikawa (post doctoral researcher), and Mr. Atsushi Wada for providing me high quality samples and teaching me to synthesize the donor molecules in their laboratory.

I am grateful to Professor Kazushi Kanoda (The University of Tokyo), Assistant Professor Kazuya Miyagawa (The University of Tokyo), and Associate Professor Hiromi Taniguchi (Saitama University) for providing me important samples and their valuable cooperation in my experiments.

I gratefully acknowledges the experimental cooperation and helpful advise given by Professor Jim S. Brooks (NHMFL, Tallahassee, USA) and Dr. David Graf (NHMFL, Tallahassee, USA).

The author is very grateful to all the colleagues in NIMS: I would like to express my appreciation to Dr. Taichi Terashima (Chief Researcher, Quantum Properties Group, NIMS) for his elaborated guidance for my experiments. I would like to thank to Dr. Shunsuke Tsuda (Senior Researcher, Quantum Properties Group, NIMS), Dr. Naoki Kikugawa (Senior Researcher, Quantum Properties Group, NIMS) for teaching and advising me about my research.

I would like to express my gratitude to Dr. Satoshi Tsuchiya (Assistant Professor in Hokkaido University), Dr. Kurita Nobuyuki (Assistant Professor in Tokyo Institute of Technology), and Dr. Kouta Kodama (SanDisk) for their valuable guidance and many discussions. I am grateful to Yoritsugu Iida-kun and Dr. Takayuki Isono for helping my experiments. I am also grateful to Megumi Tomita-san, Mariko Saito-san for supporting our experiments in NIMS.

I also thank to my friends especially Maho Yamaguchi, Yuki Takahashi, Satoshi Demura, Keita Deguchi, and other friends in my doctoral and master courses.

I am also very grateful to NIMS for making my Ph.D. study possible by the financial support.

Finally, I thank to my family for their support and constant encouragement.

Publications and Talks

Publication list

Refereed papers published in journals (first author)

K. Sugii, K. Takai, S. Uji, T. Terashima, H. Akutsu, A. Wada, S. Ichikawa, J. Yamada, T. Mori, and T. Enoki,
" Crystal Structure and Physical Properties of π-d System κ-(BDH-TTP)$_2$FeBr$_4$ " ,
J. Phys. Soc. Jpn., **82**, 054706 (2013).

K. Sugii, K. Takai, S. Uji, T. Terashima, H. Akutsu, A. Wada, S. Ichikawa, J. Yamada, and T. Enoki,
" Magnetic and Transport Properties of π-d System κ-(BDH-TTP)$_2$FeCl$_4$ " ,
J. Phys. Soc. Jpn., **82**, 124709 (2013).

K. Sugii, K. Takai, S. Tsuchiya, S. Uji, T. Terashima, H. Akutsu, A. Wada, S. Ichikawa, J. Yamada, and T. Enoki,
" Magnetic Torque Studies of π-d System κ-(BDH-TTP)$_2$FeX$_4$ (X = Br, Cl) " ,
J. Phys. Soc. Jpn., **83**, 023704 (2014).

Refereed papers published in journals (co-author)

S. Uji, K. Kodama, K. Sugii, Y. Takahide, T. Terashima, N. Kurita, S. Tsuchiya, M. Kohno, M. Kimata, K. Yamamoto, and K. Yakushi,
" Kosterlitz-Thouless-Type Transition in a Charge Ordered State of the Layered Organic Conductor α-(BEDT-TTF)$_2$I$_3$ " ,
Phys. Rev. Lett., **110**, 196602 (2013).

S. Tsuchiya, J. Yamada, T. Terashima, N. Kurita, K. Kodama, K. Sugii, and S. Uji,
" Fluctuating Superconductivity in the Strongly Correlated Organic Superconductor κ-(BEDT-TTF)$_2$Cu[N(CN)$_2$]Br " ,
J. Phys. Soc. Jpn., **82**, 064711 (2013).

S. Uji, K. Kodama, K. Sugii, T. Terashima, Y. Takahide, N. Kurita, Satoshi S. Tsuchiya, M. Kimata, T. Konoike, A. Kobayashi, B. Zhou, and H. Kobayashi,
" Orbital Effect on FFLO Phase and Energy Dissipation due to Vortex Dynamics in Magnetic-Field-Induced Superconductor λ-(BETS)$_2$FeCl$_4$ " ,
J. Phys. Soc. Jpn., **82**, 034715 (2013).

S. Tsuda, N. Kikugawa, K. Sugii, S. Uji, S. Ueda, M. Nishio, and Y. Maeno,
" Mott transition extremely sensitive to impurities in $Ca_3Ru_2O_7$ revealed by hard x-ray photoemission studies " ,
Phys. Rev. B, **87**, 241107(R) (2013).

S. Uji, K. Kodama, K. Sugii, T. Terashima , Y. Takahide, N. Kurita, S. Tsuchiya, M. Kimata, A. Kobayashi, B. Zhou, and H. Kobayashi,

“ Magnetic torque studies on FFLO phase in magnetic-field-induced organic Superconductor λ-$(BETS)_2FeCl_4$ ” ,
Phys. Rev. B, **85**, 174530 (2012).

S. Yasuzuka, S. Uji, T. Terashima, S. Tsuchiya, K. Sugii, B. Zhou, A. Kobayashi, and H. Kobayashi,
“ In-Plane Anisotropy of Flux-Flow Resistivity in Layered Organic Superconductor λ-$(BETS)_2FeCl_4$ ” ,
J. Phys. Soc. Jpn., **83**, 013705 (2014).

Talks in conference

International conference

(oral talk) K. Sugii, K. Takai, S. Uji, T. Terashima, A. Wada, S. Ichikawa, J. Yamada, and T. Enoki,
“ Effect of π-d Interaction on Conductivity in κ-$(BDH\text{-}TTP)_2FeX_4$ (X=Br, Cl) ”
9the International Symposium on Crystalline Organic Metals, Superconductors and Ferromagnets (ISCOM2011), Poznan, Poland, September, 2011.

(poster talk) K. Sugii, K. Takai, S. Ichikawa, J. Yamada, and T. Enoki,
“ Magnetoresistance of π-d material κ-$(BDH\text{-}TTP)_2FeBr_4$ ” ,
5th Japan-France Symposium on Molecular Materials: Electronics, Photonics and Spintronics, Rennes, France, October, 2010.

(poster talk) K. Sugii, K. Takai, S. Tsuchiya, S. Uji, T. Terashima, A. Wada, S. Ichikawa, J. Yamada, T. Enoki, D. Graf, and J. S. Brooks,
“ Magnetic Properties and Fermi Surface of κ-$(BDH\text{-}TTP)_2FeCl_4$ ” ,
International Conference on Science and Technology of Synthetic Metals (ICSM2012), Atlanta, America, July, 2012.

(poster talk) K. Sugii, S. Tsuchiya, k. Miyagawa, K. Kanoda, H. Taniguchi, T. Terashima, and S. Uji,
“ Incoherent Interlayer Transport in α-$(BEDT\text{-}TTF)_2NH_4Hg(SCN)_4$ ” ,
7th Japan-France Symposium on Molecular Materials: Electronics, Photonics and Spintronics, Durham, England, September, 2012.

(poster talk) K. Sugii, S. Tsuchiya, k. Miyagawa, K. Kanoda, H. Taniguchi, T. Terashima, and S. Uji,
“ Incoherent Interlayer Transport in α-$(BEDT\text{-}TTF)_2NH_4Hg(SCN)_4$ ” ,
International Symposium on Materials Science Opened by Molecular Degree of Freedom (MDF2012), Miyazaki, Japan, December, 2012.

National conference (Japanese)

(口頭) 杉井かおり, 高井和之, 市川俊, 山田順一, 榎敏明
「金属性 π-d 系物質 κ-$(BDH\text{-}TTP)_2FeBrl_4$ の磁気抵抗」
日本物理学会 2009 年秋季大会, 28pYC-9, 熊本, 2009 年 9 月

(口頭) 杉井かおり, 高井和之, 市川俊, 山田順一, 寺嶋太一, 宇治進也, 榎敏明
「κ-(BDH-TTP)$_2$FeX$_4$ (X=Br, Cl) の磁気輸送特性」
日本物理学会 2010 年秋季大会, 23aRB-5, 大阪, 2010 年 9 月.

(口頭) 杉井かおり, 高井和之, 宇治進也, 寺嶋太一, 和田淳志, 市川俊, 山田順一, 榎敏明
「κ-(BDH-TTP)$_2$FeX$_4$ (X=Br, Cl) の磁性」
日本物理学会 2011 年秋季大会, 22aTR-7, 富山, 2011 年 9 月.

(口頭) 杉井かおり, 土屋聡, 宇治進也, 寺嶋太一, 圷広樹, 和田淳志, 市川俊, 山田順一, 高井和之, 榎敏明, D. Graf, J. S. Brooks
「π-d 系有機導体 κ-(BDH-TTP)$_2$FeX$_4$ (X=Br, Cl) のフェルミ面」
日本物理学会第 67 回年次大会, 24aBK-11, 兵庫, 2012 年 3 月.

(口頭) 杉井かおり, 宮川和也, 鹿野田一司, 谷口弘三, 土屋聡, 寺嶋太一, 宇治進也
「α-(BEDT-TTF)$_2$NH$_4$Hg(SCN)$_4$ における面間インコヒーレント伝導」
日本物理学会 2012 年秋季大会, 18pEB-1, 横浜, 2012 年 9 月.

(ポスター) 杉井かおり, 高井和之, 宇治進也, 寺嶋太一, 和田淳志, 市川俊, 山田順一, 榎敏明
「π-d 系有機導体 κ-(BDH-TTP)$_2$FeX$_4$ (X=Br, Cl) の磁気輸送特性」
新学術領域研究第 5 回領域会議, 東京, 2011 年 6 月.

(ポスター) 杉井かおり, 土屋聡, 宇治進也, 寺嶋太一, 圷広樹, 和田淳志, 市川俊, 山田順一, 高井和之, 榎敏明, D. Graf, J. S. Brooks
「π-d 系有機導体 κ-(BDH-TTP)$_2$FeX$_4$ (X=Br, Cl) のフェルミ面」
新学術領域研究第 6 回領域会議, 宮城, 2012 年 1 月.